Electrohydrodynamic (EHD) Printing of Microparticle Streams for Additive Manufacturing

by

Yue Guan

B.S., Tsinghua University (2014)

Submitted to the Department of Mechanical Engineering in partial fulfillment of the requirements for the degree of

Master of Science in Mechanical Engineering

at the

Massachusetts Institute of Technology

September 2016

Signature of Author: Signature redacted

Department of Mechanical Engineering

August 19, 2016

Certified by: Signature redacted

A. John Hart

Associate Professor of Mechanical Engineering

Thesis Supervisor

Accepted by: Signature redacted

Rohan Abeyaratne

Department of Mechanical Engineering

Chairman, Committee for Graduate Students

this page intentionally left blank

Electrohydrodynamic (EHD) Printing of Microparticle Streams for Additive Manufacturing

by

Yue Guan

Submitted to the Department of Mechanical Engineering
on August 19, 2016, in partial fulfillment of the requirements for the degree of
Master of Science in Mechanical Engineering

Abstract

Electrohydrodynamic (EHD) printing can be used to fabricate high resolution (~100 nm) features at high rates (~10 kHz), and is compatible with a wide range of materials. However, conventional EHD printing techniques focus only on homogeneously dispersed functional inks, including nanoparticulate materials, molecular and polymers. This thesis explores EHD printing of liquids containing microparticles. For printing, liquids containing microparticles with a diameter of ~1-10 μm are prepared, which sediment upon loading into the capillary tip. A single-tip EHD apparatus enabling pulsed delivery of kilovolt signals, high speed imaging, and measurement of charge transfer to the substrate has been constructed. Using this apparatus, it is shown that pulsed voltage signals can cause printing of liquid droplets, streams, and aggregates containing microparticles, at rates of ~10 kHz. Upon evaporation of the liquid, the particles organize into clusters that, depending on the deposition conditions, may form continuous lines or regularly spaced aggregates. By first-order modeling of the forces exerted on the particles, it is concluded that the amount of colloidal material ejected from the capillary is influenced by the packing of the particles within the meniscus, their size, the strength of electrostatic and Van der Waals interactions, and other factors. Future work should focus on the design of the colloidal solution and EHD parameters to enable controlled and consistent ejection of particles, and improvement of the accuracy of deposition. This process therefore is attractive for additive manufacturing of composite materials by direct deposition of microparticles.

Thesis Supervisor: A. John Hart

Title: Associate Professor of Mechanical Engineering

this page intentionally left blank

Acknowledgements

First and foremost, I would like to express my deepest gratitude to my advisor Prof. A. John Hart, for his guidance and support throughout my master study. The past two years has been very tough to me, he has been extremely patient to help me overcome the difficulties in research here at MIT. His vision, knowledge and constant encouragement have inspired and helped me in all the time of research and writing this thesis.

I would like to thank Justin Beroz for introducing the concept of EHD printing of microparticles to me, which is the foundation of this thesis.

I would like to thank Hangbo Zhao, who has been a big brother to me ever since I joined the group. His encouragement and support has helped me get through a lot of hard times.

I would also like to thank my fellow lab mates, especially Dr. Sanha Kim, Dhanushkodi Mariappan, Alvin Tan, Stuart Baker and Ryan Oliver for many exciting discussions and constructive suggestions; Adam Stevens, Nick Dee, Ron Rosenberg and Nigamaa Nayakanti for sharing their experiences and suggestions on writing theses; Dr. Orb, Crystal Owens, Bethany Lettiere, Kehang Cui and Yu Zou for sharing a lot of fun times; and of course our administrative assistants Saana McDaniel and Haden Quinlan for their tireless efforts to take care of so much lab stuff and make our group a better place to work in. It is such an awesome and memorable experience to work with all you guys at the Mechanosynthesis Group.

Moreover, I would like to thank MIT Deshpande Center and MIT Lincoln Laboratory for their financial support during the past two years.

Big thanks to numerous friends who have supported me through this journey and shared their happiness and sadness with me. It is great to have you all.

Finally, I would like to express my special thanks to my family, especially my parents, grandparents and my girlfriend Jenny Wu for their unconditional love, support and understanding. None of this could have been possible without you.

this page intentionally left blank

Contents

List of Figures

this page intentionally left blank

List of Tables

this page intentionally left blank

Chapter 1: Introduction and Thesis Goals

1.1. Motivation and Background

Additive manufacturing (AM), which has also been widely known as 3D printing, is rapidly gaining popularity as a novel manufacturing process. Unlike the conventional subtractive manufacturing (SM) process which yields the desired parts by selectively removing materials from the raw material in a series of cutting operations [1], AM is a process of selectively depositing and joining materials to make objects from 3D digital model data, usually in a layer by layer fashion [2,3]. (Fig. 1.1)

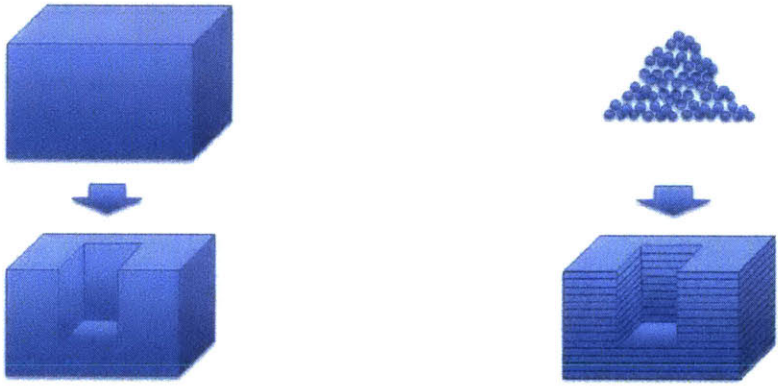

Subtractive Manufacturing **Additive Manufacturing**

Fig. 1.1 Subtractive Manufacturing (SM) versus Additive Manufacturing (AM). [4]

AM is capable of rapid prototyping and creating complex geometries [1,2]. Materials are directly deposited in AM processes hence in many situations material waste is reduced. Moreover, AM has great potential to process functionally graded materials and multi-material parts, and difficult-to-machine materials [3].

Typical AM processes include fused deposition modeling (FDM) [5], digital light processing (DLP) [6,7], laminated object manufacturing (LOM) [8,9], electron beam freeform fabrication (EBF^3) [10,11], selective laser sintering (SLS) [12,13], directed energy deposition (DED) [14], stereolithography (SLA) [15,16], and material jetting (inkjet) [17] (Fig. 1.2).

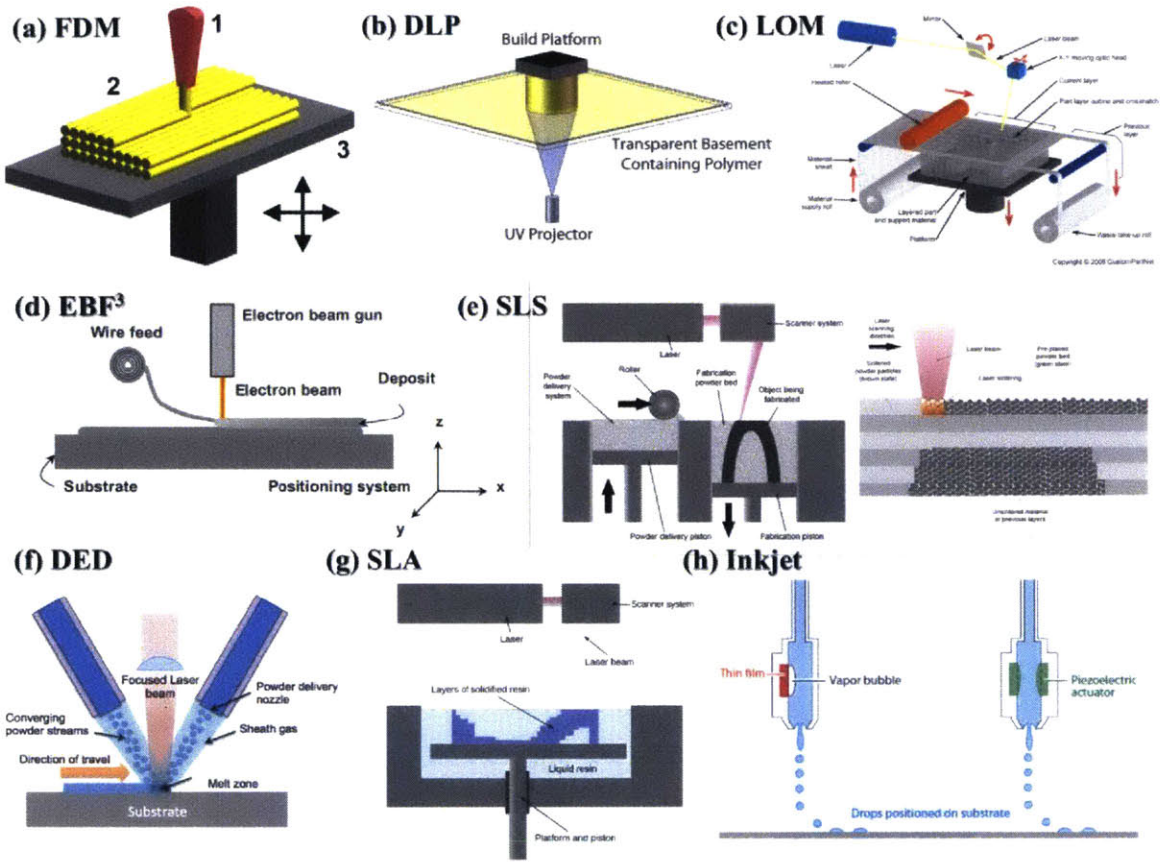

Fig. 1.2 Typical AM processes. [5-17]

Among the above, inkjet printing has been gaining traction as a versatile direct-write manufacturing approach for a wide variety of applications in materials fabrication beyond its traditional role in graphics output and marking [18]. It has been widely applied in various fields including printed electronics, optics, and bioengineering [19-22].

The key of the inkjet printing process is the generation and ejection of ink droplets from a nozzle aperture, which are then deposited onto the substrates in a noncontact fashion with high-resolution spatial control.

Thermal and piezoelectric based driving mechanisms are conventionally used for droplet generation and ejection in inkjet printing (Fig. 1.2(h) left: thermally driven; right: piezoelectrically driven) [17]. However, these mechanisms have encountered the critical challenge to achieve sub 10 μm patterned feature sizes, due to limitations on the minimum volume (typically in the picoliter range) of the droplets they can print.

Since the beginning of this century, researchers have been exploiting electrostatic forces to drive the generation and ejection of droplets through fine nozzles, which offers a solution to overcome the limited resolution of the conventional thermally and piezoelectrically driven inkjet printing [18]. This technique is call electrohydrodynamic (EHD) driven inkjet printing, wherein a bias voltage is imposed between the nozzle and the substrate to drive the generation and ejection

of liquid droplets which can contain ink particles. Other researchers have shown EHD printing is capable of creating patterns with feature sizes approaching ~100 nm at ~10 kHz rate, with a wide range of printable materials including metals, ceramics, polymers and other functional materials, as additives in a carrier liquid. More details about the fundamentals, applications and previous studies of EHD driven inkjet printing will be addressed in Chapter 2.

However, conventional EHD-driven inkjet printing techniques focus on homogenously dispersed functional inks, like nanoparticulate materials, molecular, polymers and etc. In this thesis, the EHD printing of liquids containing microparticles is explored. For this, we prepare colloidal suspensions containing microparticles with diameters ranging from 1 μm to 10 μm[1], allowing their gravitational sedimentation to stack into layers of particles at the tip of the nozzle near the meniscus. Upon application of a pulsed voltage, the particles are ejected along with the liquid. The microparticles are deposited onto the substrate in clusters (Fig. 1.3).

Therefore, EHD printing of particle streams preserves the strengths of conventional EHD-driven inkjet printing techniques (e.g., high spatial resolution, compatibility with various materials, high-throughput and broad applicability), while further extends this technology as a direct-write AM approach towards the regime of microparticulate materials.

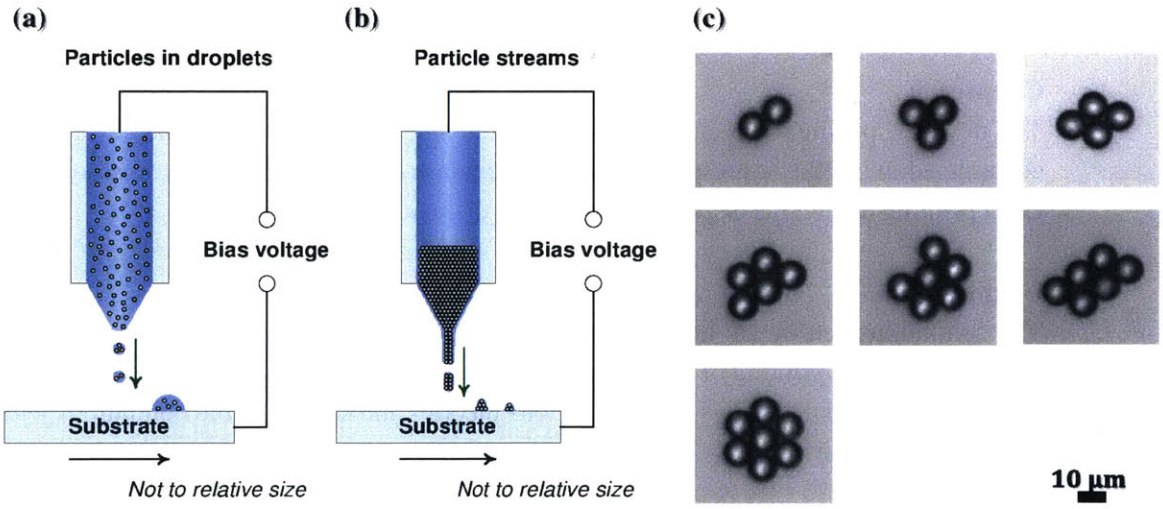

Fig. 1.3 Concept and demonstrations of EHD printing of particle streams: (a) Particles in droplets using conventional EHD-driven inkjet printing technique which focus on homogeneously dispersed functional inks; (b) EHD printing of particle streams of microparticulate materials; (c) Printed particle clusters consisting of 10 μm diameter polystyrene microparticles with different numbers of particles, ranging from 2 to 7, on glass microscope slides via EHD printing of particle streams.

[1] For microparticles with diameter smaller than 1 μm, specific mechanisms other than gravitational forces alone to deliver the particles to the tip of the capillary will be developed in the future.

1.2. Thesis Scope

In this thesis, we present an apparatus and experiments performed to demonstrate and control EHD printing of particle streams. A customized single-tip apparatus has been designed and constructed for experimental study. Colloidal suspensions containing microparticles with different sizes and materials have been printed on demand within the regime of particle streams. Moreover, the force balance of the microparticles upon printing has been analyzed, and three distinct modes of printing microparticulate materials have been observed and qualitatively explained in light of the forces involved. Furthermore, the capabilities of EHD printing of particle streams onto CNT forests and onto a metal powder bed are demonstrated.

The remainder of this thesis is organized as follows:

- **Chapter 2:**
  A brief overview of EHD-driven inkjet printing is presented, including the fundamentals of EHD jetting mechanism, the formation of the Taylor cone and the calculation of the Taylor cone angle, as well as a literature review of prior work done on EHD-driven inkjet printing techniques.

- **Chapter 3:**
  The design, specifications and operation of the single-tip EHD experimental apparatus constructed in our lab is presented. It is also demonstrated that the charge transferred upon EHD printing can be measured, and related to the mode of printing.

- **Chapter 4:**
  Via continuous jetting of liquid containing a low concentration of microparticles, we demonstrate EHD printing of dot arrays and continuous lines. The comparison of the results from the patterned dot arrays versus previous theories and studies of the continuous jetting mechanism is detailed.

- **Chapter 5:**
  In this chapter, we study the pulsed EHD printing from densely packed microparticles in the capillary tip, which results ideally in the streaming of liquid along with particles onto the substrate. Printing experiments of colloidal suspensions containing microparticles with different sizes and materials are demonstrated, as well as demonstrations of depositing microparticles onto porous substrates. A first-order modeling of the forces exerted on the particles upon ejection has been conducted to investigate the governing constitutive laws of the ejection of the microparticle streams qualitatively.

- **Chapter 6:**
  The thesis is summarized and recommendations for future work are discussed, including the design of the colloidal solution and EHD parameters to enable controlled and consistent ejection of particles, and improvement of the accuracy of deposition, towards AM capabilities of composite materials by direct deposition of microparticles.

this page intentionally left blank

Chapter 2: Fundamentals of EHD Jetting

In this chapter, we will start with a brief introduction to the concept of EHD jetting, EHD driven inkjet printing will follow, including the mechanism of EHD jetting through a capillary, the formation of the Taylor cone, and the phase diagrams of the EHD ejection modes. The chapter will close with a literature review of previous studies on EHD driven inkjet printing.

2.1. EHD Overview

EHD is a branch of fluid mechanics which studies the dynamics of electrically charged fluids [23]. EHD mechanism has been widely used in various applications, some striking ones include EHD driven inkjet printing [18], electrospinning [24-25], EHD cooling [26,27], EHD thrusters [28,29], electrospray [30,31], air ioniser, fluidized bed stabilization and so on [27]. (Fig. 2.1)

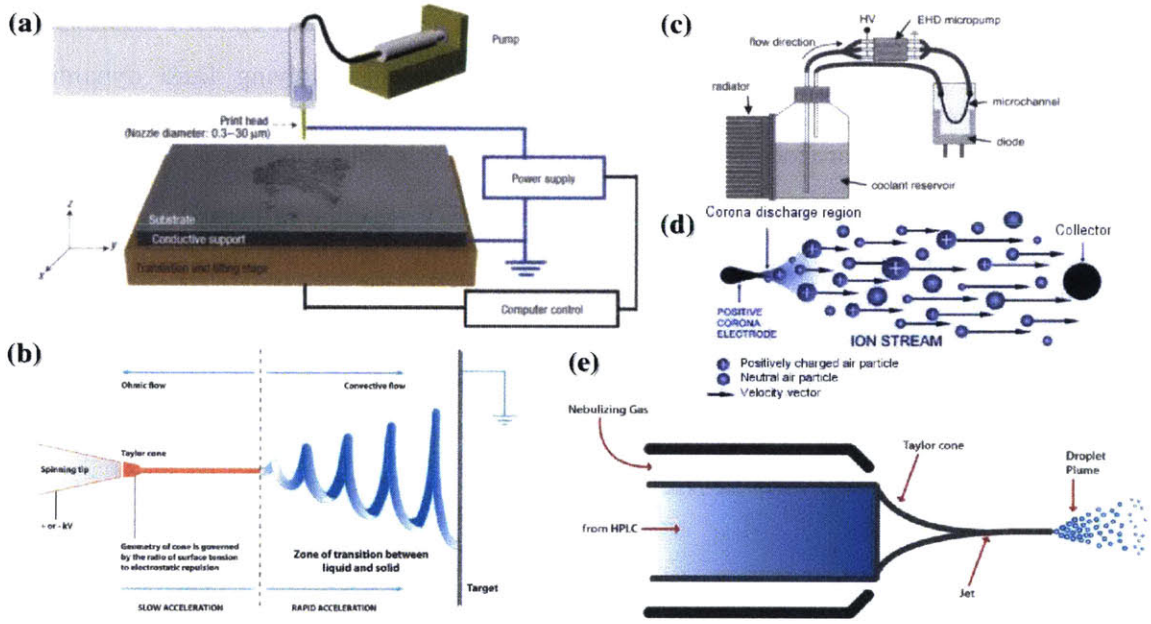

Fig. 2.1 Applications of EHD mechanism: (a) EHD driven inkjet printing; (b) Electrospinning; (c) EHD cooling; (d) EHD thrusters; (e) Electrospray. [18, 24-31]

The research on EHD can be traced back to the late 16th century, when the earliest record of an EHD experiment was conducted by William Gilbert [32]. He observed that a droplet of water would deform into a conical shape upon bringing a charged rod above it. In 1750, Jean-Antoine (Abbé) Nollet observed that water flowing from an electrified vessel which was placed near the electrical ground would aerosolize [33]. In 1882, Lord Rayleigh performed theoretical studies of the dynamics of an electrified droplet. He revealed how forces in the radial direction stemming from the surface charge of the droplet offset surface tension and estimated the maximum amount of

charge an electrified water droplet could carry, which has been referred to as the "Rayleigh limit" [34]. Rayleigh's prediction that an electrified droplet reaching the "Rayleigh limit" would eject fine jets from its surface was verified experimentally in 1989 [35]. John Zeleny published a paper in 1914 studying the behavior of liquid meniscus at the tip of an electrified capillary. In this paper, he was the first to experimentally investigate different EHD ejection modes, such as the pulsation and cone jet modes. [36] Three years later in 1917, Zeleny succeeded in capturing the time-lapse images of the dynamics of an electrified meniscus. [37] In 1962, R. S. Allan and S. G. Mason started to look into the dynamics of poorly conductive liquids under electrical fields, which they named as leaky dielectrics. [38] In 1964, Sir Geoffrey Ingram Taylor theoretically modeled the shape of an electrified droplet and calculated the angle of the cone. He also conducted experiments to verify his model and the agreement was within 1%. This cone is famous as "Taylor cone". [39] Five years later in 1969, Taylor and J. R. Melcher developed the leaky dielectric model to study the dynamics of conducting fluids with the effects of electrical fields. [23] In 1997, D. A. Saville reported a more detailed discussion and derivation on the underlying assumptions of the Taylor-Melcher leaky dielectric model and applied it towards a unified treatment of EHD. [32]

The underlying physics of EHD is a coupled problem involving fluid dynamics and electromagnetics and has been studied mainly via experimental and numerical methods as the analytical formulations are too complex to lead to closed form solutions.

The differential equations and the boundary conditions to describe EHD related phenomena are summarized in the following Table 2.1, which consists of two main parts: the electrodynamic part and the hydrodynamic part. The electrodynamic part is basically Maxwell's equations, while the hydrodynamic part describes the conservation of mass and momentum of the liquids. [23]

	Differential Laws	Boundary Conditions
Electrodynamics	$\nabla \times \mathbf{E} = 0$ $\nabla \cdot \mathbf{D} = \mathrm{q}$ $\nabla \cdot \mathbf{J} + \frac{\partial \mathrm{q}}{\partial \mathrm{t}} = 0$ $\mathbf{D} = \varepsilon_0 \mathbf{E} + \mathbf{P}$	$\mathbf{n} \times [\mathbf{E}] = 0$ $\mathbf{n} \cdot [\mathbf{D}] = \mathrm{Q}$ $\mathbf{n} \cdot [\mathbf{J}] + \nabla_{\Sigma} \cdot \boldsymbol{K} = \mathbf{n} \cdot \mathbf{v}[\mathrm{q}] - \frac{\partial \mathrm{Q}}{\partial \mathrm{t}}$
Hydrodynamics	$\rho \frac{D\boldsymbol{v}}{Dt} = \rho \boldsymbol{g} + \nabla \cdot (\boldsymbol{T^m} + \boldsymbol{T^e})$ $T_{ij}{}^{m} = \mu \left(\frac{\partial v_i}{\partial x_j} + \frac{\partial v_j}{\partial x_i} \right) - \delta_{ij} p$ $\nabla \cdot \mathbf{v} = 0$	$\mathbf{n}[\mathrm{p}] = n \cdot (\boldsymbol{T^m} + \boldsymbol{T^e})$ $\mathbf{n} \times [\mathbf{v}] = 0$ $\mathbf{n} \cdot [\mathbf{v}] = 0$
Notation	**E**: strength of the electric field q: density of free charge **D:** electric displacement **P**: polarization density **v**: velocity of the boundary Q: surface charge density **K**: surface current density ρ: mass density of the fluid μ: viscosity of the fluid	**g**: gravitational acceleration p: pressure **n**: unit normal of the boundary directed from region (b) to region (a) $\boldsymbol{T^m}$: viscous stress $\boldsymbol{T^e}$: electromagnetic stress $[\mathrm{A}] \equiv A^a - A^b$: the jump of A across the interface from region (b) to (a) ∇_{Σ}: surface Nabla

Table 2.1 Fundamental differential equations and boundary conditions describing EHD.

2.2. EHD Jetting

Electrostatic forces can manipulate the dynamics of conductive fluids. When conductive fluid is introduced into a capillary, EHD mechanism can drive the ejection of the liquid through the capillary tip, this is call EHD jetting. As is shown in Fig. 2.2, the EHD jetting system is basically composed of two parts: a fine capillary containing conductive liquid and a counter electrode which is separated from the tip of the capillary by a certain distance.

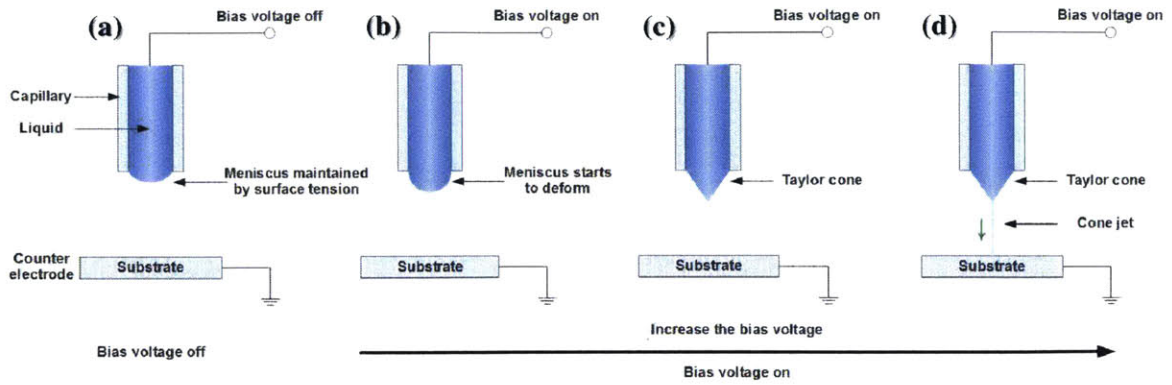

Fig. 2.2 Schematic of the EHD jetting process.

When a bias voltage is imposed between the capillary (thus the conductive liquid inside it) and the counter electrode, the meniscus at the tip of the capillary will start to deform. At a certain amplitude of the bias voltage, the meniscus will turn into a stable conical shape due to the force balance between the electrostatic force and surface tension force. Sir Geoffrey Ingram Taylor was the first researcher to systematically rationalize the mechanism of the formation of the conical meniscus, thus it was named after him as "Taylor cone". [39] When further increasing the bias voltage, electrostatic force will beat surface tension force, which leads the apex of the cone to break and eject a fine, stable and continuous jet from the tip of the meniscus.

EHD jetting has been widely used as a novel mechanism of inkjet printing, for direct, additive patterning of materials. EHD driven inkjet printing is advantageous over the conventional inkjet printing mechanisms, e.g., thermal and piezoelectric driven inkjet printing, since it is capable of printing features with size approximately 100nm at 10 kHz frequency.

The high resolution of EHD driven inkjet printing is due to the following reasons [18]:

1. The inner diameters of the capillaries can be much smaller than those used in thermal and piezoelectric driven inkjet printing processes, where the size of the capillaries need to be large enough to maintain high pressure to overcome surface tension.
2. EHD driven inkjet printing is capable of generating droplets/jets with sizes that are 1~2 orders of magnitude smaller than the dimension of the capillary due to the condition that the ejection happens at the apex of the Taylor cone.
3. The distribution of the electrical field lines facilitates the focusing of the trajectories of the ejected droplets to minimize lateral variations in the materials placement.

The high frequency (10 kHz) of EHD driven inkjet printing is either due to the natural resonant frequency of the fluid in the capillary or the frequency of the applied bias voltage.

2.2.1. Taylor Cone

As has been explained above, Taylor cone is a key characteristic feature of the EHD driven inkjet printing process. The formation of the Taylor cone makes the EHD jetting happen either right at the apex of the conical meniscus or around a very small portion of it, which enables that the ejected droplets/jets can be 1~2 orders of magnitude smaller than the inner diameter of the capillary.

In this section, we will derive expressions for the Taylor cone angle. This derivation is based on the original paper by Sir Geoffrey Ingram Taylor in 1964, which was the first theoretical study of the EHD jetting problem which outlined the conditions of the formation of the conical shape of an electrified droplet and the calculation of the cone angle. [39]

Let us consider an electrified water droplet with a conical shape in the spherical coordinates $< \hat{r}, \hat{\theta}, \hat{\varphi} >$, with its apex at the origin and axis coinciding with the Z axis. The semi-vertical angle of the cone is denoted as α. The schematic is illustrated in Fig. 2.3.

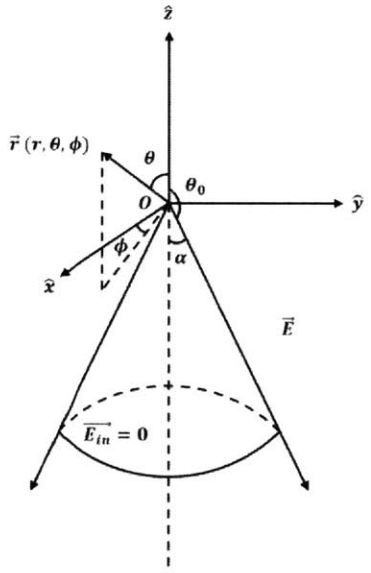

Fig. 2.3 An electrified conical water droplet in the spherical coordinates $< \hat{r}, \hat{\theta}, \hat{\varphi} >$.

The modeling assumptions are:

1. The liquid is perfectly conductive, hence the droplet is an equipotential body and its surface is an equipotential surface as well.
2. The droplet forms a perfect conical shape[2].
3. The conical droplet exists in a steady state equilibrium.

[2] Other geometries (e.g., spherical shape) of the electrified droplet can maintain the steady state equilibrium as well. Here we assume that the conical shape of the droplet has already formed, and then derive the angle of the cone. Which shape the droplet will maintain at the steady state equilibrium depends on the initial state, and for liquid inside a capillary, conical meniscus will form at the tip of the capillary.

4. The steady state equilibrium of the droplet is maintained by the balance between the local pressure difference due to surface tension and the local electromagnetic tensor on the surface of the droplet.

We use the following three steps to obtain the results:

1. Derive the local pressure difference across the surface of the droplet due to surface tension.
2. Derive the local electromagnetic tensor on the surface of the droplet.
3. Apply the pressure balance to maintain the steady state equilibrium of the conical droplet shape to derive the charge distribution on the surface of the droplet, the distribution of the electric field and electric potential in the space, as well as the Taylor cone angle.

$P(r, \pi - \alpha, \varphi)$ is an arbitrary point on the surface of the droplet. According to Young–Laplace equation, the local pressure difference across the surface of the droplet due to surface tension is given by

$$\Delta p = \gamma\left(\frac{1}{R_1} + \frac{1}{R_2}\right) \tag{2.1}$$

where γ is the surface tension of water, R_1 and R_2 are the principal radii of curvature.

At point P on the surface of the conical droplet, we have

$$R_1 = r\sin\alpha \tag{2.2}$$

$$R_2 = \infty \tag{2.3}$$

Hence, the pressure difference across the surface of the droplet due to surface tension at the point P is

$$\Delta p = \gamma\left(\frac{1}{R_1} + \frac{1}{R_2}\right) = \frac{\gamma}{r\sin\alpha} \tag{2.4}$$

The charge has been distributed on the surface of the droplet in the way where: a). the stable conical shape of the droplet is maintained due to the pressure balance; b). the droplet is an equipotential body.

Let us pick a differential piece whose surface charge density is σ and surface area is ds. We have drawn a Gaussian pillbox with the differential piece at the middle of its two parallel planes and the cross sectional area is ds as well. This schematic is illustrated in Fig. 2.4.

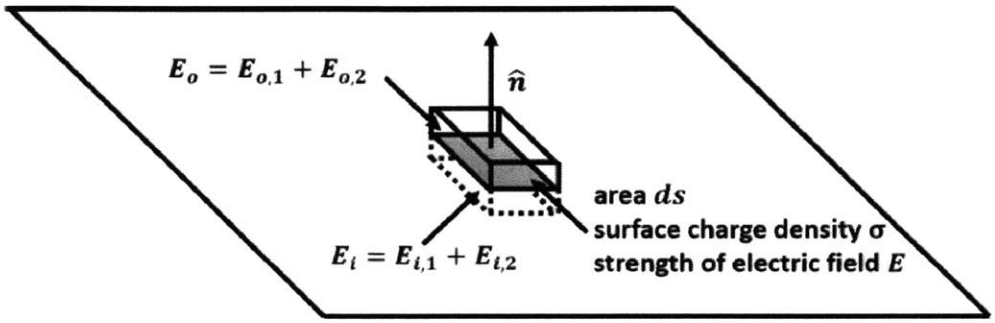

Fig. 2.4 A Gaussian pillbox around a differential piece on the surface of the water droplet.

According to Gauss's flux theorem, we have

$$\nabla \cdot \mathbf{E} = \frac{q_{free}}{\varepsilon} \tag{2.5}$$

$$\oint \mathbf{E} \cdot \partial \mathbf{s} = \frac{q_{free}}{\varepsilon} \tag{2.6}$$

Hence

$$E_i ds + E_o ds = \frac{\sigma ds}{\varepsilon_0} \tag{2.7}$$

where E_i and E_o are the strengths of the electric field right inside and outside the differential piece, respectively.

As the droplet is considered as a perfect conductor, hence

$$E_i = 0 \tag{2.8}$$

Therefore

$$E_o = \frac{\sigma}{\varepsilon_0} \tag{2.9}$$

E_o is the total strength of the electric field right outside the differential piece, which consists of the contribution from both the differential piece itself and the charge on the surface of the droplet other than the differential piece. Hence,

$$E_o = E_{o,1} + E_{o,2} = \frac{\sigma}{\varepsilon_0} \tag{2.10}$$

where $E_{o,1}$ and $E_{o,2}$ are the contribution from the differential piece and other charge, respectively.

Similarly

$$E_i = E_{i,1} + E_{i,2} = 0 \tag{2.11}$$

$E_{i,1}$ and $E_{i,2}$ are the contributions from the differential piece and other charge to the strength of the electric field right inside the differential piece, respectively.

Furthermore, it is obvious that

$$E_{o,1} = -E_{i,1} \tag{2.12}$$

$$E_{o,2} = E_{i,2} \tag{2.13}$$

Thus

$$E_{o,1} = E_{o,2} = E_{i,2} = \frac{\sigma}{2\varepsilon_0} \tag{2.14}$$

$$E_{i,1} = -\frac{\sigma}{2\varepsilon_0} \tag{2.15}$$

Thus the strength of the electric field right at the differential piece is

$$\mathrm{E} = E_{o,2} = E_{i,2} = \frac{\sigma}{2\varepsilon_0} \tag{2.16}$$

as the charge on the differential piece has no contribution to the electric field right at itself.

Hence the pressure difference across the differential piece due to electromagnetic tensor is given by

$$\Delta \mathrm{p}' = \mathrm{E}\sigma = \frac{\sigma^2}{2\varepsilon_0} \tag{2.17}$$

Due to the pressure balance to maintain the steady state equilibrium of the droplet

$$\Delta p = \Delta p' \tag{2.18}$$

Therefore

$$\frac{\gamma}{r sin\alpha} = \frac{\sigma^2}{2\varepsilon_0} \tag{2.19}$$

Hence

$$\sigma \propto r^{-\frac{1}{2}} \tag{2.20}$$

Furthermore,

$$E \propto \sigma \propto r^{-\frac{1}{2}} \tag{2.21}$$

Based on the above analysis, we can now summarize the boundary conditions of the electrified conical droplet:

1. The conical water droplet is an equipotential body whose electric potential is a constant. Denote the constant as V_0.
2. The strength of the electric field on the surface of the droplet only has nonzero $\hat{\theta}$ directed component, while its $\hat{r}$ and $\hat{\varphi}$ directed components are both zero.
3. The $\hat{\theta}$ directed component of the strength of the electric field on the surface of the droplet is proportional to $r^{-\frac{1}{2}}$.

Based on the boundary conditions above, we can calculate the value of the Taylor cone angle as follows. We denote the distribution of the electric potential in the space as

$$V = V(r, \theta) \tag{2.22}$$

where the dependence on the $\hat{\varphi}$ direction is eliminated due to azimuthal symmetry.

By applying separation of variables, the distribution of the electric potential can be represented as

$$V(r, \theta) = R(r)\Theta(\theta) \tag{2.23}$$

The general solutions in spherical coordinates can be denoted as

$$R_l(r) = A_l r^l + \frac{B_l}{r^{l+1}} \tag{2.24}$$

$$\Theta_l(\theta) = P_l(cos\theta) \tag{2.25}$$

where l is a positive real number, A_l and B_l are constant real numbers, $P_l(cos\theta)$ is the l^{th} order Legendre polynomial of the variable $cos\theta$, which is calculated from

$$\frac{d}{dx}\left[(1-x^2)\frac{d}{dx}P_l(x)\right] + l(l+1)P_l(x) = 0 \tag{2.26}$$

Hence,

$$V(r, \theta) = \sum_{l \in R^+} R_l(r)\Theta_l(\theta) = \sum_{l \in R^+} \left(A_l r^l + \frac{B_l}{r^{l+1}}\right) P_l(cos\theta) \tag{2.27}$$

Furthermore, the distribution of the electric field is

$$\mathbf{E} = -\nabla V = -\frac{\partial V}{\partial r}\hat{r} - \frac{1}{r}\frac{\partial V}{\partial \theta}\hat{\theta} - \frac{1}{r sin\theta}\frac{\partial V}{\partial \varphi}\hat{\varphi} = -\frac{\partial V}{\partial r}\hat{r} - \frac{1}{r}\frac{\partial V}{\partial \theta}\hat{\theta} = E_r\hat{r} + E_\theta\hat{\theta} \tag{2.28}$$

where

$$E_r = -\sum_{l\in R^+}\left(lA_l r^{l-1} - (l+1)\frac{B_l}{r^{l+2}}\right)P_l(cos\theta) \tag{2.29}$$

$$E_\theta = -\sum_{l\in R^+}\left(A_l r^{l-1} + \frac{B_l}{r^{l+2}}\right)\frac{d}{d\theta}P_l(cos\theta) \tag{2.30}$$

Consider the boundary condition that when $\theta = \pi - \alpha$, $E_r = 0$ and $E_\theta \propto r^{-\frac{1}{2}}$.

Hence it is obvious by inspection that when $l \neq \frac{1}{2}$, the coefficients

$$A_l = B_l = 0 \tag{2.31}$$

$$B_{\frac{1}{2}} = 0 \tag{2.32}$$

$$A_{\frac{1}{2}} \neq 0 \tag{2.33}$$

The statement $E_r = 0$ will be verified later in this section.

Therefore,

$$\mathbf{E} = -A_{\frac{1}{2}} r^{-\frac{1}{2}}\frac{d}{d\theta}P_{\frac{1}{2}}(cos\theta)\hat{\theta} \tag{2.34}$$

$$\mathrm{V(r,\theta)} = A_{\frac{1}{2}} r^{\frac{1}{2}} P_{\frac{1}{2}}(cos\theta) + V_0 \tag{2.35}$$

where the constant V_0 is the value of the electric potential of the droplet, which satisfies the first boundary condition that the droplet is an equipotential body.

The surface of the droplet is described by $\theta = \pi - \alpha$, hence the electric potential of the surface of the droplet is given by

$$\mathrm{V(r,\theta)}|_{\theta=\pi-\alpha} = -A_{\frac{1}{2}} r^{\frac{1}{2}} P_{\frac{1}{2}}(cos\alpha) + V_0 \tag{2.36}$$

As the surface of the droplet is an equipotential surface, hence $= -A_{\frac{1}{2}} r^{\frac{1}{2}} P_{\frac{1}{2}}(cos\alpha) + V_0$ is a constant, which does not rely on the value of r, hence

$$P_{\frac{1}{2}}(cos\alpha) = 0 \tag{2.37}$$

For $\alpha \in \left(0, \frac{\pi}{2}\right)$, the only value for α to satisfy $P_{\frac{1}{2}}(cos\alpha) = 0$ is

$$cos\alpha \approx 0.652 \tag{2.38}$$

Hence,

$$\alpha \approx 49.3^\circ \tag{2.39}$$

This is the semi-vertical angle of the conical droplet, hence the whole angle is $2\alpha \approx 98.6°$.

Now we will look back into the $\hat{r}$ directed component of the electric field on the surface of the droplet

$$E_r|_{\theta=\pi-\alpha} = \sum_{l\in R^+}\left(lA_l r^{l-1} - (l+1)\frac{B_l}{r^{l+2}}\right)P_l(cos\alpha) \equiv 0 \tag{2.40}$$

as $P_{\frac{1}{2}}(cos\alpha) = 0$.

Moreover, based on the analysis of pressure balance, we will further derive the distribution of the electric potential and the strength of the electric field in the space.

As

$$\mathrm{E} = \frac{\sigma}{2\varepsilon_0} \tag{2.41}$$

$$\frac{\gamma}{r sin\alpha} = \frac{\sigma^2}{2\varepsilon_0} \tag{2.42}$$

Therefore

$$\mathrm{E} = \left(\frac{\gamma}{2\varepsilon_0 sin\alpha}\right)^{\frac{1}{2}} \mathrm{r}^{-\frac{1}{2}} \tag{2.43}$$

where E is the strength of the electric field on the surface of the droplet,

While we have also derived the distribution of the electric field based on the distribution of the electric potential, given by

$$\mathrm{E} = -A_{\frac{1}{2}} r^{-\frac{1}{2}} \frac{d}{d\theta} P_{\frac{1}{2}}(cos\theta)|_{\theta=\pi-\alpha} \tag{2.44}$$

Denote $\mathrm{C} = \frac{d}{d\theta} P_{\frac{1}{2}}(cos\theta)|_{\theta=\pi-\alpha}$. C is a constant which can be calculated numerically, hence

$$-CA_{\frac{1}{2}} r^{-\frac{1}{2}} = \left(\frac{\gamma}{2\varepsilon_0 sin\alpha}\right)^{\frac{1}{2}} \mathrm{r}^{-\frac{1}{2}} \tag{2.45}$$

Hence

$$A_{\frac{1}{2}} = -\frac{1}{C}\left(\frac{\gamma}{2\varepsilon_0 sin\alpha}\right)^{\frac{1}{2}} \tag{2.46}$$

To summarize:

1. The semi-vertical angle of the Taylor cone is $\alpha \approx 49.3^{\circ}$. This is universal for any conductive liquid droplet of any size.
2. The distribution of the electric potential and the distribution of the electric field in the entire space are

$$\mathrm{V}(\mathrm{r},\theta) = \begin{cases} A_{\frac{1}{2}} r^{\frac{1}{2}} P_{\frac{1}{2}}(cos\theta) + V_0, & for\ \theta \in [0, \pi-\alpha] \\ V_0, & for\ \theta \in (\pi-\alpha, \pi] \end{cases} \tag{2.47}$$

$$\mathbf{E}(\mathrm{r},\theta) = \begin{cases} -\frac{1}{2} A_{\frac{1}{2}} r^{-\frac{1}{2}} P_{\frac{1}{2}}(cos\theta)\hat{r} - A_{\frac{1}{2}} r^{-\frac{1}{2}} \frac{d}{d\theta} P_{\frac{1}{2}}(cos\theta)\hat{\theta}, & for\ \theta \in [0, \pi-\alpha] \\ 0, & for\ \theta \in (\pi-\alpha, \pi] \end{cases} \tag{2.48}$$

3. The charge distribution on the surface of the droplet is

$$\sigma(\mathrm{r}) = 2\varepsilon_0 E_r|_{\theta=\pi-\alpha} = -2\varepsilon_0 CA_{\frac{1}{2}} r^{-\frac{1}{2}} = \left(\frac{2\gamma\varepsilon_0}{sin\alpha}\right)^{\frac{1}{2}} \mathrm{r}^{-\frac{1}{2}} \tag{2.49}$$

The above derivation of the Taylor cone angle was made under the assumption of an ideal conducting liquid. However, in practice this is rarely the case. Derivation of the Taylor cone angle of a dielectric liquid has been explored by N. Zubarev. As has been derived above, the semi-vertical

angle of the Taylor cone for a conducting liquid is 49.3°. For dielectric liquids, the semi-vertical angle of the Taylor cone is between 39.3° and 49.3°. The exact value depends on the relative permittivity of the dielectric. [40]

2.2.2. Phase Diagram of the EHD Ejection Modes

Even though EHD jetting through a capillary is conceptually simple, the underlying physics is actually very complicated. The jet formation and ejection process is critical for the EHD driven inkjet printing process, since it determines the optimal printing parameters towards required printing performances, including resolution, positioning accuracy, frequency, throughput, uniformity, and reproducibility.

There are different ejection modes of EHD jetting [41], which are defined as how the liquid droplets/jets are formed and ejected, including the geometry and frequency of the ejection. Usually, for a given type of liquid and system geometry (e.g., capillary size and the separation between the capillary tip and the substrate), the EHD ejection modes depend mainly on the strength of the electric field E and the flow rate Q. Fig. 2.5 shows a generalized qualitative phase diagram of EHD ejection modes with respect to E and Q. The shapes of the regimes for different modes and their threshold values of E and Q depend on the properties of the ink and the system geometry as well.

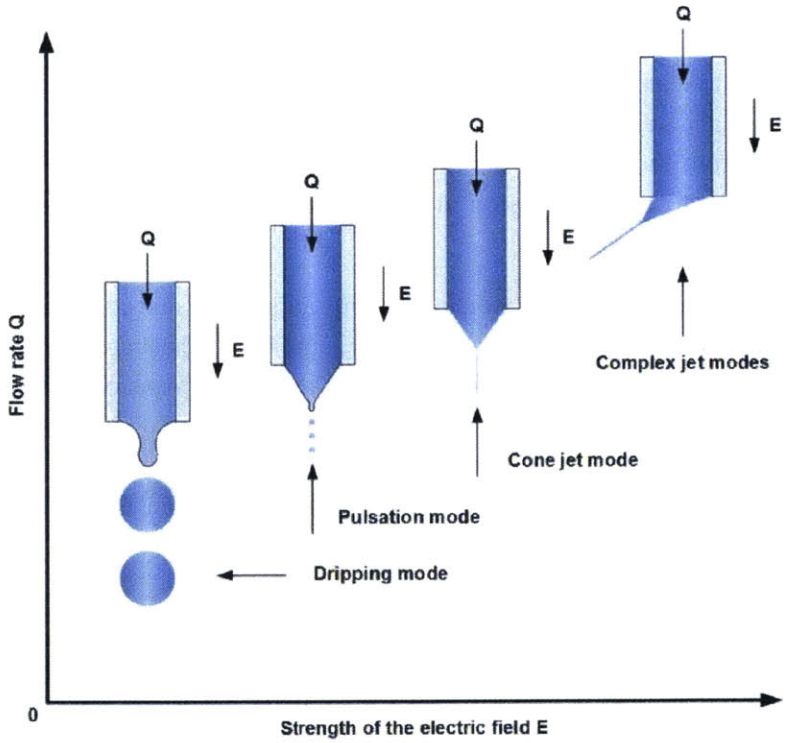

Fig. 2.5 Phase diagram of the EHD ejection modes with respect to the strength of the electric filed E and flow rate Q.

As is shown in the phase diagram in Fig. 2.5, there are mainly four different types of EHD ejection modes: dripping mode, pulsation mode, cone jet mode and complex jet modes (including titled jet mode, twin jets mode and multi-jet mode).

1. Dripping mode:
   In the dripping mode, the bias voltage is not large enough to support the formation of the Taylor cone and hence the gravitational force drives the pendant droplets to pinch off from the tip of the capillary. The size of the droplets are comparable to or even larger than the dimension of the capillary and the ejection happens at a frequency less than 1 Hz.
2. Pulsation mode:
   Pulsation mode is the transition mode from the dripping mode to the cone jet mode. When the bias voltage is increased, the electrostatic force increases and becomes large enough to support the formation of a conical meniscus at the tip of the capillary and only a small portion around the apex of the conical meniscus oscillates and ejects droplets/jets, which are 1~2 orders of magnitude smaller than the dimension of the capillary. Pulsation mode is composed of a sequence of periodical emission pulses (10~100 Hz) and each pulse contains a bunch of droplet/jet ejections (kHz).
3. Cone jet mode:
   With certain combinations of the strength of the electrical field and flow rate, Taylor cone remains stable and only its apex breaks and ejects a fine, stable and continuous jet. This is called the cone jet mode.
4. Complex jet modes:
   When the bias voltage is increased further, the electrostatic force becomes much larger than the surface tension force and hence Taylor cone is hard to maintain anymore. Usually the jet starts to lean towards one side and the axes of the cone may spin about the axis of the capillary and hence this is known as tilted jet mode. In addition, more than one jet will be ejected from the meniscus as the electromagnetic tensor exceeds the local pressure difference due to surface tension at multiple locations on the meniscus, which further induces jets.

Among the four different EHD ejection modes, pulsation mode and cone jet mode are favorable for EHD driven inkjet printing, since: 1) on the one hand, they are capable of generating droplets/jets with size ~2 orders of magnitude smaller than the dimension of the capillary at kHz rate, which enables high speed high resolution patterning of materials; 2) on the other hand, the directions of the ejections are well aligned along the axis, which guarantees the accuracy of the positioning of materials. Moreover, the EHD ejection modes can be identified via the measurements of the printing current. This will be illustrated in detail in Chapter 3.

Refer to the phase diagram of the EHD ejection modes: the strength of the electrical field E can be translated from the bias voltage and the system geometry, while typically there are two different types of the flow rate Q: the external flow rate and the internal flow rate. During ejection, if the flow is provided externally by the motion of the plunger, the flow rate is named as external flow rate. The external flow rate is an input of the EHD ejection process, and determines the EHD

ejection modes together with the electrical field. If the flow is induced only by the bias voltage (e.g., in the cases where the capillary is not attached to a plunger or the plunger is stationary), the flow rate is named as internal flow rate. The internal flow rate is an output of the EHD ejection process and the EHD ejection modes are determined by the bias voltage and the dynamics of the capillary side of the printing system. [42] Hence, in the printing systems with the setup of the external flow rate, there are two degrees of freedom to control the EHD ejection modes and the whole phase diagram can be occupied. While in schemes with the internal flow rate, the flow rate is self-regulated to be a function of the electrical field, hence the achievable regime on the phase diagram is a family of lines (as illustrated in Fig. 2.6). Each line represents a certain type of responses of the flow rate to the electrical filed, which are dependent on the hydrodynamics of the capillary side of the printing systems.

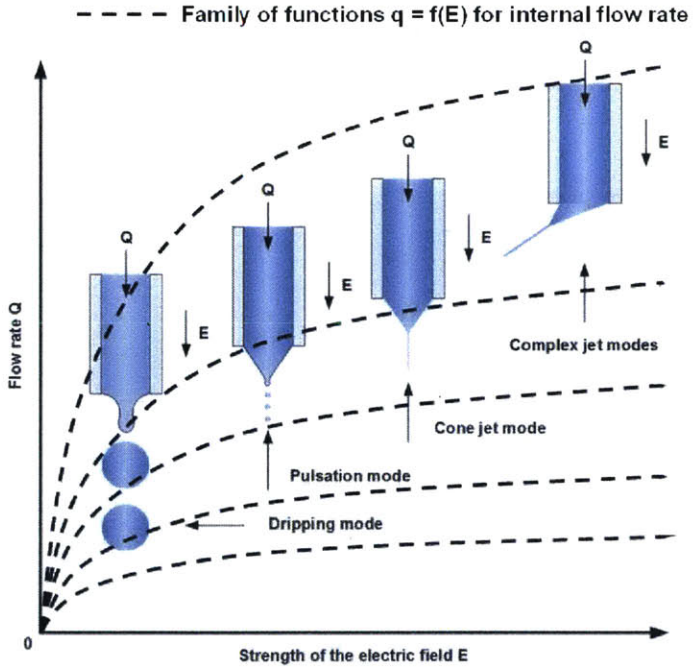

Fig. 2.6 Phase diagram of EHD ejection modes in the self-regulated internal flow rate scheme.

The phase diagrams of the EHD ejection modes provide us roadmaps to choose the optimal printing parameters to achieve the desired printing performances.

2.2.3. Literature Review

EHD driven inkjet printing has been extensively investigated since the beginning of this century and has now grown to be one of the most promising fabrication technologies for additive manufacturing at micro and nanoscale.

Mitsuru Ishikawa and co-workers reported one of the earliest demonstrations of EHD driven inkjet printing, which fabricated dot arrays from rhodamine B with sub 5 μm diameters. [43] Aksay and co-workers were the first to systematically investigate the generation, delivery and positioning of droplets via EHD driven inkjet printing, and demonstrate sub 10 μm resolution which was better than the conventional thermal and piezoelectric driven inkjet printing techniques. [44,45] Rogers and co-workers further demonstrated the capability of the EHD driven inkjet printing technique to print different inks on various substrates to fabricate complex patterns with sub 100 nm resolution, which greatly expanded the capabilities and applications of EHD driven inkjet printing. [46-51] (Fig. 2.7)

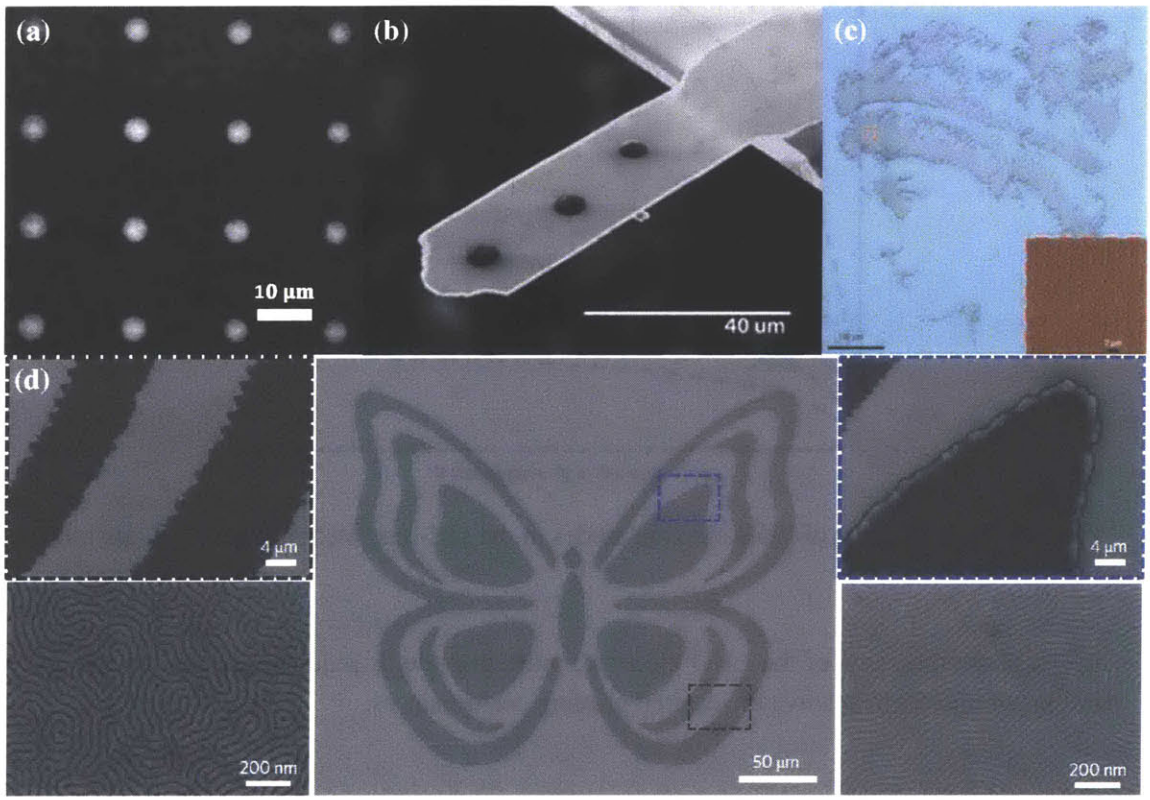

Fig. 2.7 Examples of patterns printed using EHD driven inkjet printing: (a) Microarray of rhB molecules; (b) Polymer droplets on microcantilever gravimetric sensors; (c) Printed portrait of Hypatia, an ancient scholar; (d) Butterfly pattern printed using block-copolymer films. [43-51]

Lee et al. investigated the phase diagrams of the EHD ejection modes and their dependence on the space of the printing parameters, which consists of ten key parameters including the properties of the ink, geometry of the system and the printing conditions. They conducted dimensionless analysis and revealed the phase diagrams of the EHD ejection mode with respect to the dimensionless strength of the electric field and dimensionless flow rate, which provided useful information for choosing the appropriate process conditions. [52] (Fig. 2.8)

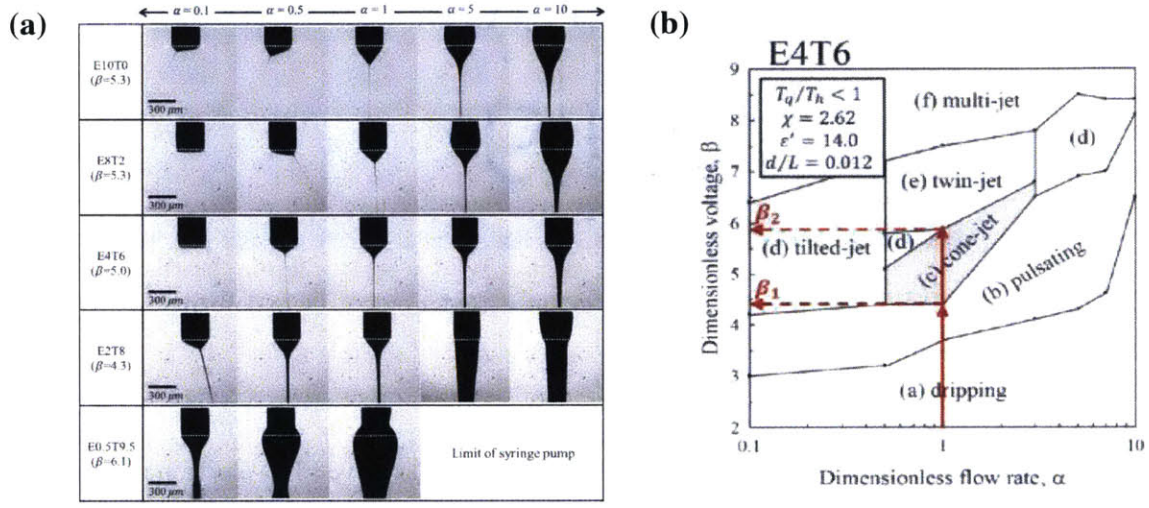

Fig. 2.8 Phase diagram of EHD ejection modes with respect to the dimensionless strength of the electrical field β and flow rate α: (a) Different jetting behaviors of mixtures of ethanol and terpineol with different volume fractions; (b) Phase diagram of EHD ejection modes with 40% ethanol and 60% terpineol in volume fractions respectively. [52]

Basaran and co-workers built thorough models to study the EHD tip streaming from a droplet [53] and a film [54] respectively. They investigated the mechanism of drop formation and succeeded in capturing the entire evolution of EHD ejection process, including the deformation of the meniscus, the formation of the Taylor cone and the disintegration of droplets/jets. Moreover, they revealed via simulations that there were three different scaling regimes concerning the size and charge of the droplets ejected from EHD tip streaming, with respect to the conductivity of the droplet. (Fig.2.9)

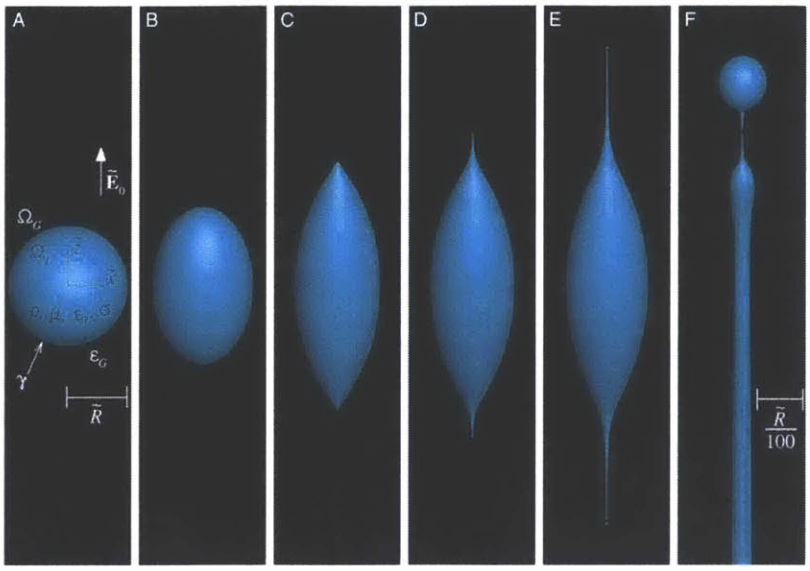

Fig. 2.9 Simulation of the time evolution of an electrified droplet: from deformation to jetting at the apex of the Taylor cone. [53-54]

Researchers have utilized pulsed bias voltage signals to achieve EHD ejection on demand. [55-59] The pulsed bias voltage signals provide more degrees of freedom to control the timing, frequency and size of the droplet ejection, which rely on the time, duration, frequency, amplitude, and the baseline value of the pulsed signals. C. H. Chen and co-workers exploited pulsed EHD ejection to deliver and position microparticles, and also investigated the scaling laws of the self-regulated flow rate and the intrinsic pulsation frequency of EHD ejection with respect to the pulsed bias voltage signals, which presented a good agreement with their experimental results. [45,60] (Fig. 2.10)

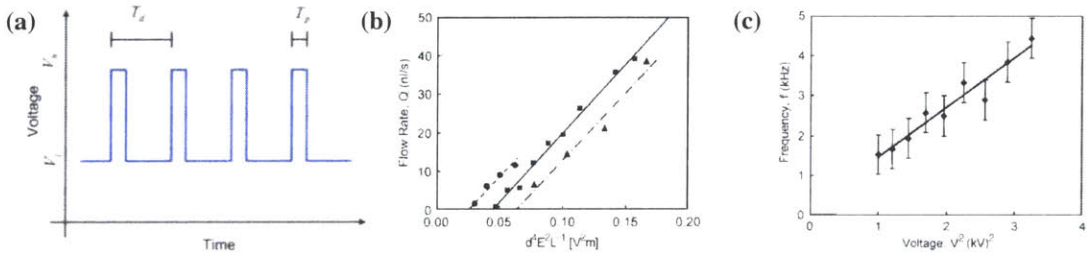

Fig. 2.10 On-demand EHD driven inkjet printing: (a) pulsed bias voltage printing signals; (b) scaling of the self-regulated flow rate of pulsed EHD jetting; (b) scaling of the ejection frequency of pulsed EHD jetting. [45, 55-60]

In order to increase the resolution, uniformity and positioning accuracy of EHD driven inkjet printing, several techniques have been applied to manipulate the distribution of the electric field between the tip of the capillary and the substrate to improve the printing quality. Lee et al. and Barton et al. reported using a ring-type gate electrode and a plate with a hole between the capillary and the substrate, respectively, to direct the electric field towards the substrate, hence to suppress the satellite droplet ejection and to allow uniform printing onto the substrates. [61,62] Dong and co-workers applied AC pulses to induce EHD ejection onto insulating substrates. With AC pulses, charge would be neutralized on the substrate hence would not affect the trajectory of the droplets in fly, which helped enhance the positioning accuracy. [63,64] (Fig. 2.11)

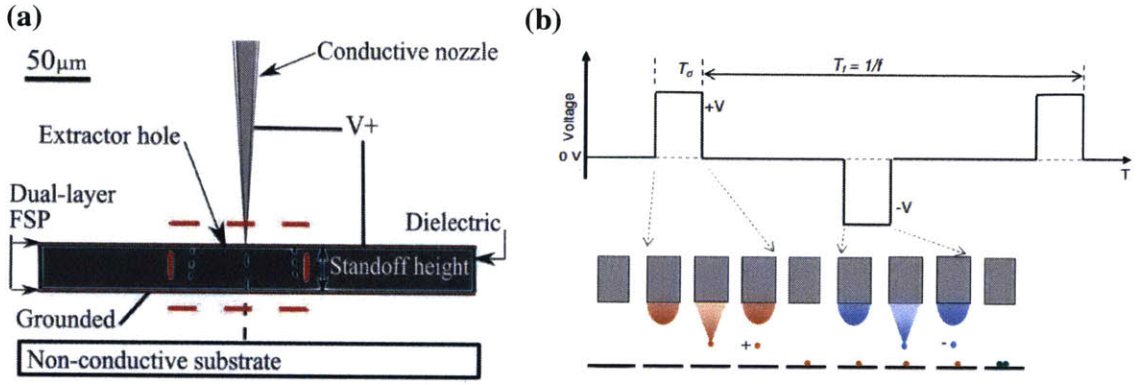

Fig. 2.11 Techniques to modify the distribution of the electrical field between the capillary and the insulating substrate to enhance uniform printing: (a) design of a dual-layer field shaping print head; (b) use of AC-pulsed bias voltage printing signals to eliminate charge accumulation on the insulating substrate. [61-64]

In addition to conventional customized EHD driven inkjet printers which usually operate in a batch mode from a single nozzle onto a single substrate, Andrew G. Alleyne et al. and Hyun Woo Dang et al. have constructed roll-to-roll (R2R) EHD driven inkjet printers. [65,66] These R2R printers are capable of continuous and large area manufacturing on flexible substrates, which pave the way for the development of flexible printed electronics. Rogers and co-workers designed and constructed multi-nozzle printing systems to allow rapid printing of multiple materials with high throughput simultaneously. [67,68] (Fig. 2.12)

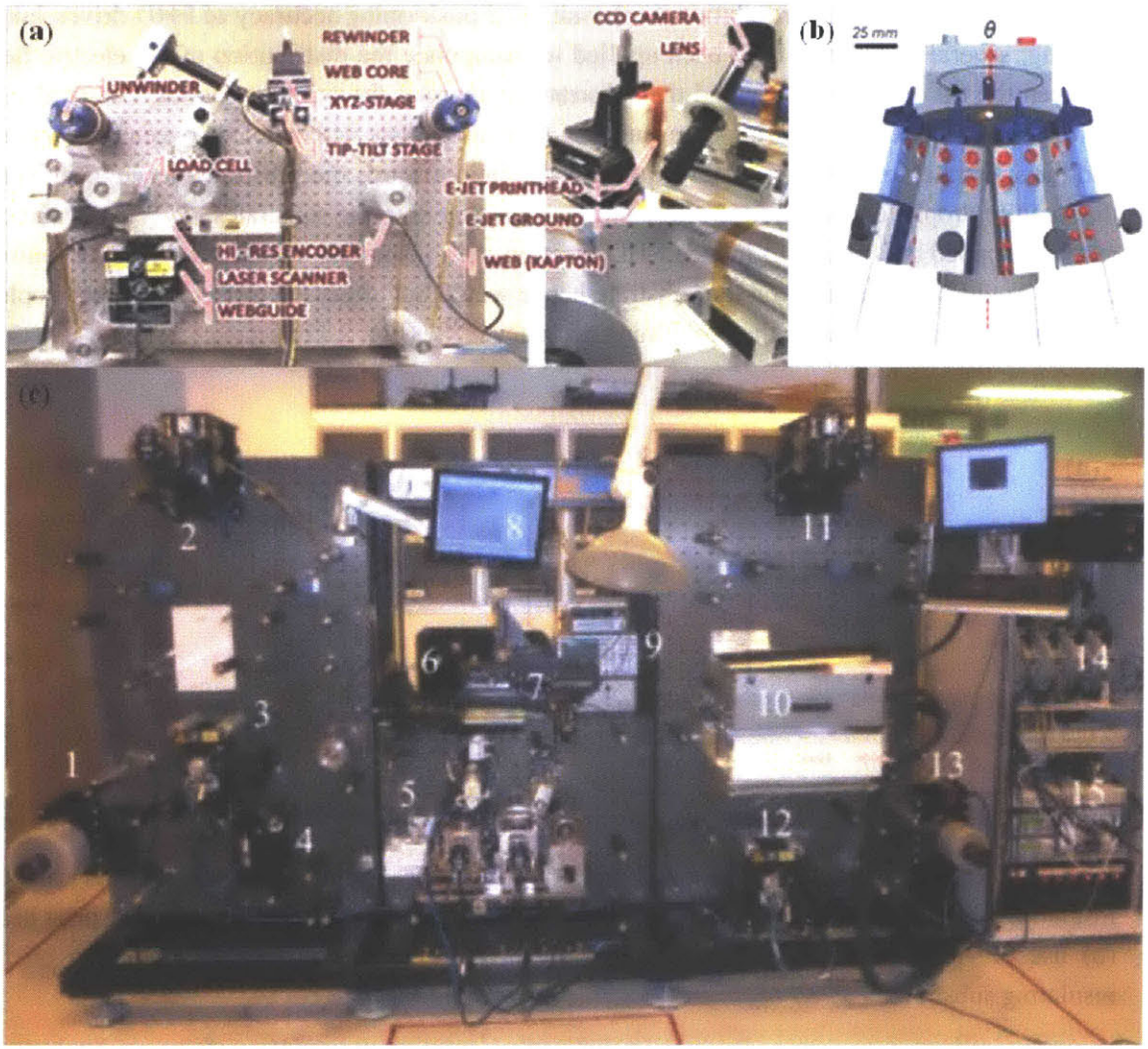

Fig. 2.12 Designs of EHD driven inkjet printing systems: (a) and (c) roll to roll printing systems; (b) multi-nozzle printing system. [65-68]

Researchers have exploited EHD driven inkjet printing as an extrusion-based, direct-write approach to manufacture 3D architectures with feature size in the micro/nano regime. Pietro Ferraro and co-workers rapidly cured polydimethylsiloxane (PDMS) during the printing process to solidify the liquid jets to allowed the fabrication of 3D structures, with an aspect ratio as high as 186. [69] Wang and co-workers printed polycaprolactone (PCL) fibers onto the substrates layer by layer to fabricate 3D PCL scaffolds for enhanced cartilage regeneration. [70] Poulikakos and co-workers applied an autofocus technique which exploited the printed structure on the substrate as the counter electrode to attract newly formed droplets to print high aspect ratio nanostructures from gold nanoparticle inks. These high aspect ratio nanostructures can be bent into different tilted pillar architectures. [71] Dong and co-works used wax as a phase change material to fabricate 3D pillar arrays with sub 10 μm resolution. [72] (Fig. 2.13)

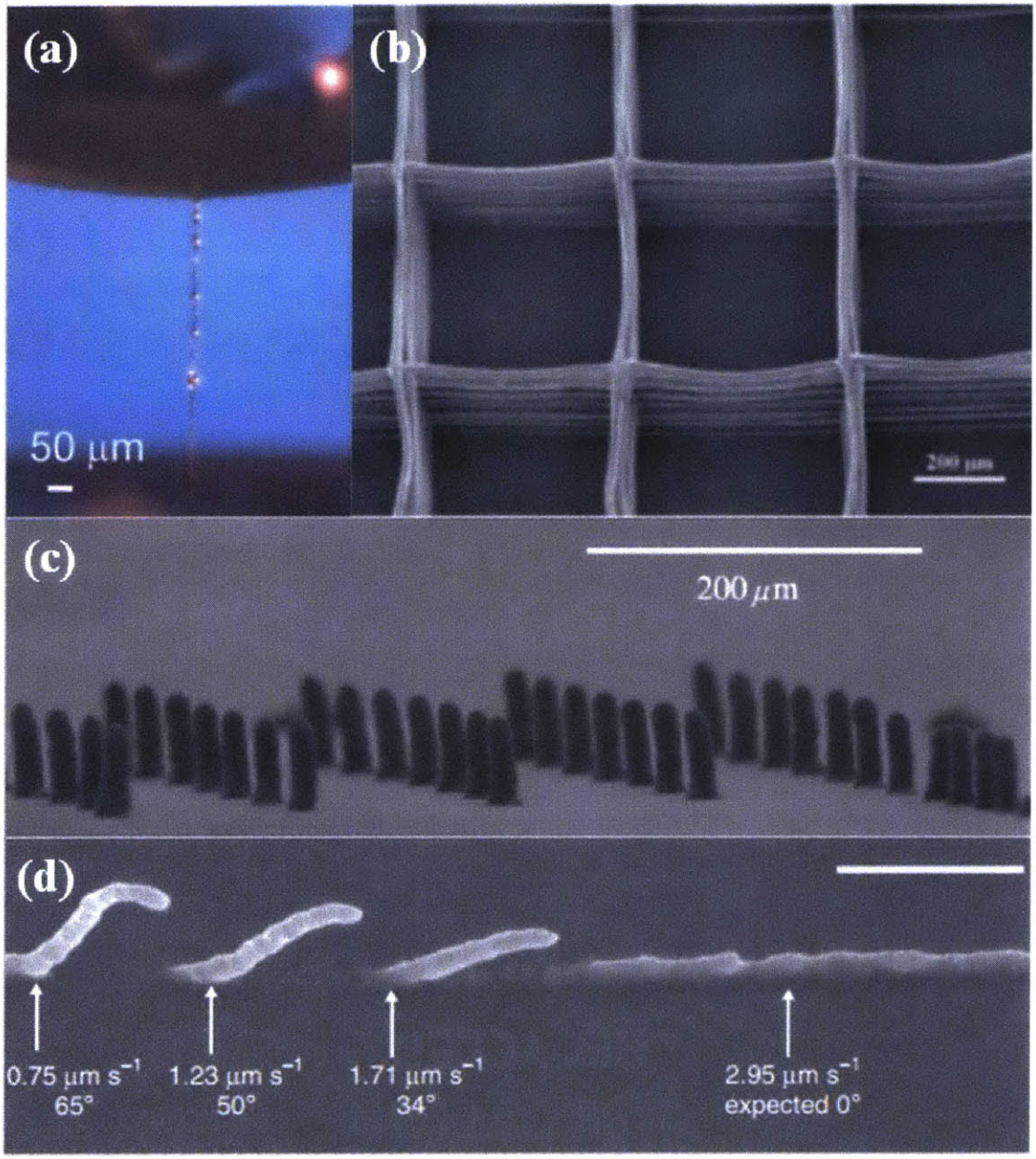

Fig. 2.13 3D architectures fabricated by EHD driven inkjet printing: (a) elongation and consolidation of a PDMS wire with multiple beads from fast cure of its EHD jets; (b) 3D polycaprolactone scaffolds; (c) 3D pillar arrays using wax as phase change inks; (d) tilted nanopillars with different angles. [69-72]

Since firstly demonstrated, EHD driven inkjet printing has been extensively explored in various applications, which poses great potential as a future mass production manufacturing approach. These applications includes printed electronics (transistors [73,74], memristors [75] and display devices [76]), sensors [77,78], biotechnology [79,80], photonic and plasmonic devices [81,82], self-assembly of nanomaterials [83], charge printing [84], 3D printing [85] and etc.

this page intentionally left blank

Chapter 3: Single-Tip Apparatus for EHD Printing of Colloidal Suspensions

This chapter presents a customized single-tip EHD experimental apparatus which has been designed and constructed In Prof. John Hart's Mechanosynthesis Group to investigate the mechanism of EHD printing of colloidal suspensions. The main objectives which guide the design are: 1) to demonstrate EHD driven printing of colloidal suspensions; 2) to understand the science behind the printing process; 3) and to achieve fine control of the printing process for AM.

3.1. System Design and Construction

Fig. 3.1 illustrates the schematic of the experimental apparatus. Fig. 3.2 shows the CAD model and the photograph of the experimental apparatus. The apparatus consists of three subsystems: flow subsystem, positioning subsystem and measurement subsystem. It is capable of both mode-controlled continuous EHD jetting and on-demand printing, along with characterizing the printing process via synchronized high speed imaging, bias voltage printing signals and measurements of printing current and transferred charge.

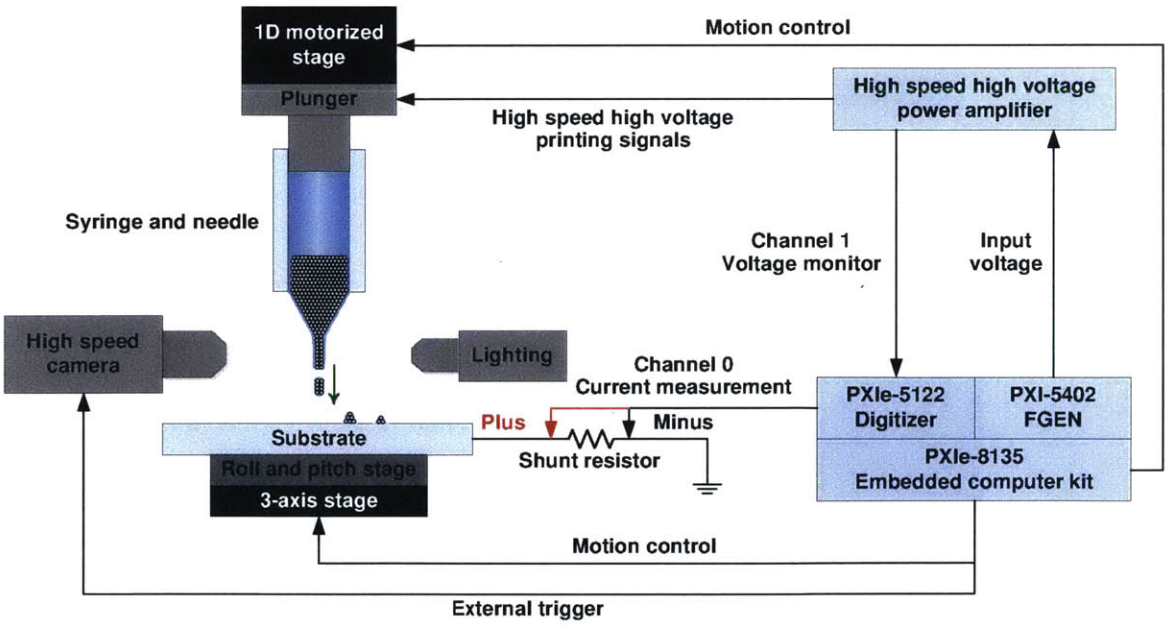

Fig. 3.1 Schematic of the experimental apparatus.

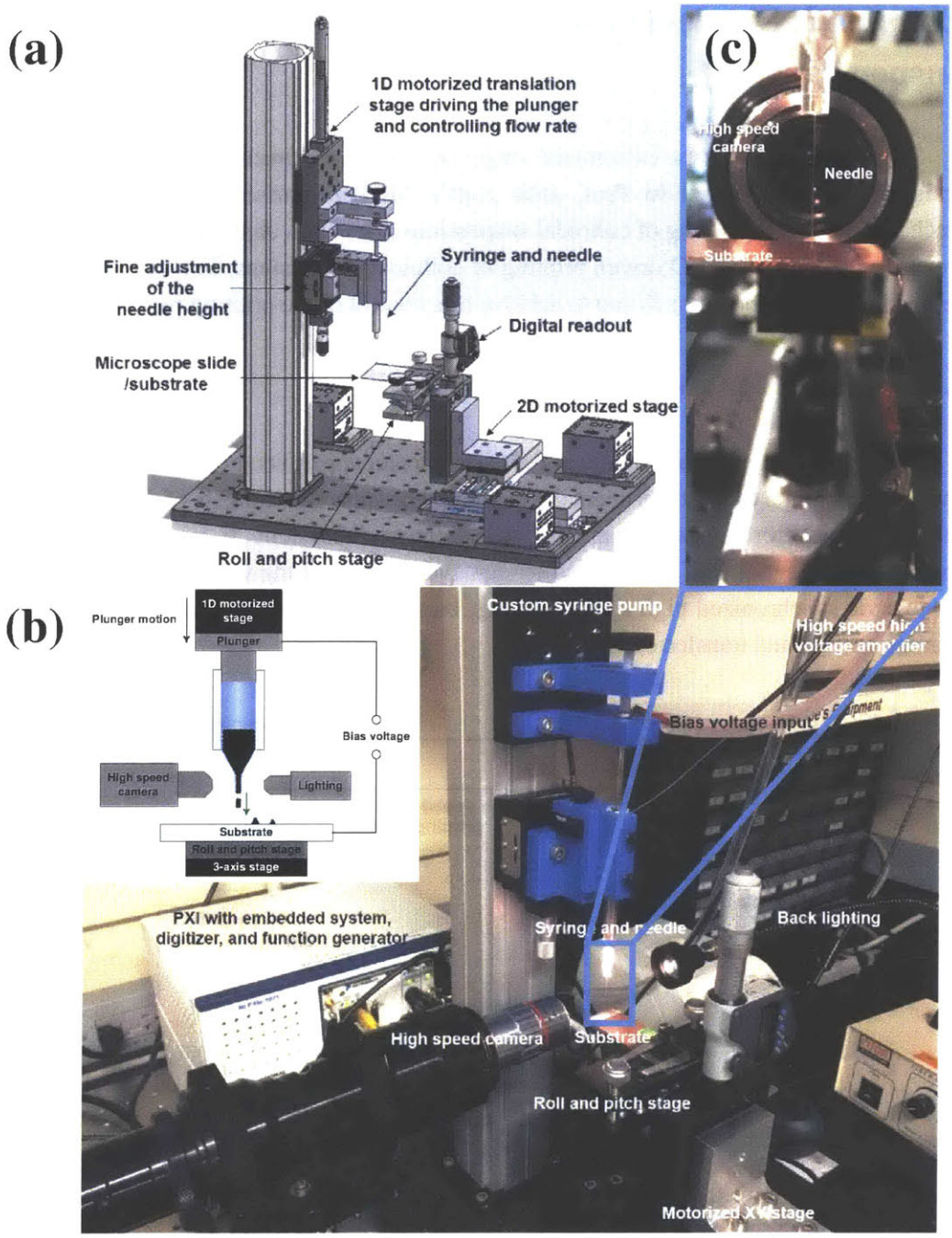

Fig. 3.2 Single-tip EHD experimental apparatus constructed in Prof. John Hart's Mechanosynthesis Group: (a) CAD model of the experimental apparatus; (b) Photograph of the experimental apparatus; (c) Zoom in photograph of the capillary-substrate part.

Table 3.1 lists the specifications of the experimental apparatus.

Subsystem	Component	Parameter	Value	Notes	Verified by measurement ?
Flow Subsystem	High speed high voltage printing signal:	Range	0 - ±10 kV		Yes
		Frequency	up to 20 MHz		
		Slew rate	> 700 V/us		
		Resolution	4 bits		Yes
	Motorized plunger	External flow rate	$10\sim10^4$ nL/s	Covering the EHD regimes of our interest	Yes
Positioning subsystem	Substrate motion	Travel range	50 × 50 mm		Yes
		Maximum velocity	2.4 mm/s		Yes
		Resolution	50 μm		Yes
Measurement Subsystem	Printing current measurement[3]	Range	7.5 nA - 7.5 uA		Yes
		Resolution	0.09 nA		Yes
		Sampling rate	up to 100 MS/s		Yes
		Bandwidth	100 MHz		
		Time constant	~100 us	Able to distinguish printing events separated by ~50 μs (20 kHz)	Yes
	High speed video recording	Recording rate	up to 10k fps		Yes

Table 3.1 Specifications of the experimental apparatus.

[3] Note: the specifications concerning printing current measurement are calculated in the case where a 2 MΩ shunt resistor is used, in parallel with the 2 MΩ input resistance of the digitizer, the effective resistance of the shunt resistor is $\frac{2}{3}$ MΩ.

The experimental apparatus we have constructed consists of three subsystems:

1. **Flow subsystem**

   Flow is induced by the electrical driving force (flow driven by the bias voltage across the capillary and the substrate) and the mechanical driving force (flow driven by plunger motion). The combination of the two driving forces determines the EHD ejection mode.

   1) Electrical driving force:

      The bias voltage is applied to the metal plunger using a function generator, whose output is amplified using a high speed high voltage power amplifier. Usually there are conflicts between high speed and high amplitude voltage signals, hence we combine the high speed capability of the function generator and the high amplitude capability of the amplifier together to achieve high voltages (~kV) at high frequencies (~kHz). Hence, the actual bias voltage across the capillary and the substrate (which is the printing signal) is given by

      $$U = GU_g \tag{3.1}$$

      where G=1000 is the gain of the amplifier, and U_g is the output of the function generator. In the experimental apparatus, both conductive and non-conductive colloidal suspensions are used. When the bias voltage is applied across the plunger and the substrate, since the liquid is charged and tends to flow from the capillary towards the substrate, the colloidal suspensions are transported by the liquid. In the case of conductive colloidal suspensions, in addition to the momentum of the fluid, the potential difference between the colloidal suspensions and the substrate provides additional driving force as the particles are charged as well.

   2) Mechanical driving force:

      The external flow rate is controlled by a customized syringe pump, in which the plunger is attached to and is driven by a motorized stage. The external flow rate is given by

      $$q = A_p v_p = \pi r_p^2 v_p \tag{3.2}$$

      where A_p, v_p and r_p are the cross sectional area, velocity and diameter of the plunger, respectively. We are also able to shape the meniscus at the tip of the capillary via controlling the position of the plunger to facilitate on-demand printing. This will be further explained in Chapter 4.

2. **Positioning subsystem**

   The substrate can be positioned in the XY plane using a two-axis motorized stage. The distance between the capillary tip and the substrate is set using a manual stage with a digital readout. The substrate is placed on a roll and pitch stage which is used to ensure that the plane of the substrate is parallel with the XY plane, hence the distance between the capillary tip and the substrate remains constant across the XY plane.

3. **Measurement Subsystem**

   In the experimental apparatus, the whole printing process can be observed and characterized via three synchronized measurement signals:

   1) Measurement signal 1, vision module: visual observation of the printing process via the high speed camera recording.

2) Measurement signal 2, printing current measurement module: measurements of the current and transferred charge during the printing process.
3) Measurement signal 3, bias voltage measurement module: measurements of the high speed high amplitude bias voltage printing signal.

The above three measurement signals are synchronized using a LabVIEV program. The measurements of the bias voltage and the printing current/charge are synchronized inside the program, while the program uses a TTL pulse to externally trigger the recording of high speed videos, ensuring that the three signals are all synchronized by timestamps.

Table 3.2 lists the devices used in the experimental apparatus.

Subsystems	Modules	devices		Part numbers
Flow Subsystem	Bias voltage generation and measurement	Function generator		National Instruments, PXI-5402
		Power amplifier		Trek, INC., 10/10B-HS
		Voltmeter		Vitrek corporation, 4700
	Customized syringe pump	Motor		Physik Instrumente, M-229.26S
		Controller		Physik Instrumente, C-663
Positioning Subsystem	XY motorized stage	Motor		Thorlabs, MTS50-Z8
		Controller		Thorlabs, TDC001
	Z axis motion	Roll and pitch stage		Customized from Thorlabs, AMA027
		Digital readout		Thorlabs, DM713
Measurement Subsystem	Vision module	High speed camera		Vision Research, Phantom Miro M310
		Lens tube	Upper zoom module	Edmund Optics, NT56-219
			Focusable lower module	Edmund Optics, NT59-698
			1 inch dovetail	Edmund Optics, NT56-205
		Objective lens		Mitutoyo, 5X
		Light source		Cuda Products Corp.,

			1-150
	Printing current measurement module	Digitizer	National Instruments, PXIe-5122
		Shunt resistor	Mouser Electronics, 71-RN55E2004B
Others	PXI sets	PXIe chassis	National Instruments, PXIe-1071
		Embedded computer kit	National Instruments, PXIe-8135
	3D printed parts[4]		Stratasys Mojo, 690-10000

Table 3.2 Devices used in the experimental apparatus.

3.2. Printing Current Measurement

When EHD driven ejection of colloidal suspensions occurs, there will be electric potential difference between the ejected material and the substrate which is held at ground potential. Hence when the droplets/jets hit the substrate, the tendency for them to reach the same electric potential drives charge to transfer from the droplets/jets to the substrate, which induces current through the substrate to its connecting lead. Similarly, after ejecting material, the meniscus needs the same amount of charge which has been ejected to restore the constant bias voltage across the meniscus and the substrate. Hence there will also be charge delivered to the meniscus via its connecting lead and inducing printing current on the capillary side as well.

Moreover, when the meniscus is shaped before ejection, charge is redistributed on the meniscus and the substrate. Hence, there will also be printing currents on both sides of the experimental apparatus. This process is illustrated in Fig. 3.3.

[4] The syringe holders are made of plastic via 3D printing in order to isolate the other parts of the experimental apparatus from the plunger since it is at ~kV.

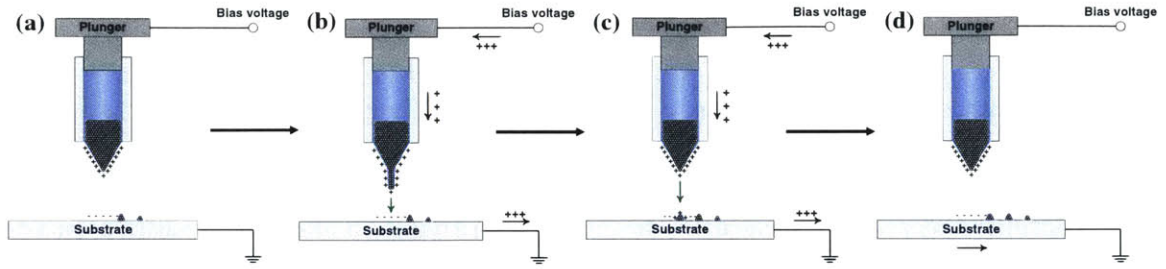

Fig. 3.3 Schematic of the EHD ejection process to induce current and transfer charge: (a) Steady state before ejection happens; (b) Ejection starts and the meniscus deforms; (c) Ejected colloidal suspensions hit the substrate; (d) Steady state after ejection finishes.

The net charge delivered to the meniscus and the charge that is transferred from the meniscus to the substrate must be equal as the whole system just transforms from a steady state to another steady state due to ejection, while the two states are identical as long as the bias voltage remains constant. However, the printing currents can be totally different as they also depend on the electrical dynamics of the system.

The printing current and charge transferred are important signatures of the EHD driven printing process, as they provide us much more information other than high speed videos alone, enabling further characterization and a physics based model of the process beyond the scope of this thesis.

The measurements of the printing current and charge transferred can be used to

1. Recognize the EHD modes of printing:
   The current measurement plots can be used to identify different EHD ejection modes since the shape of the current measurement plots vary based on the EHD ejection mode. This subject is explained in more details in the Chapter 3.2.2 below.
2. Identify and correlate individual printing events:
   As which is shown in Fig. 3.8, the peaks in the current measurement plots correlate with printing events. Each peak corresponds to a printing event and vice versa. Hence, printing current is an accurate indicator of printing events and hence could be used to implement feedback controls in real time. Whereas image analysis using high speed videos alone is computationally intensive and hence infeasible for real time control implementation.
3. Calibrate the amount of materials deposited:
   The amount of the charge transferred per ejection is related to the geometry of the droplet, properties of the colloidal suspensions and the bias voltage signals (future work will be revealing the relationships). Hence, the measurements of printing current and transferred charge can be potentially applied to detect the amount of ejected colloidal suspensions, after calibration with respect to the properties of the colloidal suspensions and bias voltage signals.

3.2.1. Selection of Shunt Resistor Value

The instantaneous printing current is measured by measuring the voltage drop across a shunt resistor. Thus the printing current can be calculated using

$$\mathrm{I} = \frac{U}{R} \tag{3.3}$$

where U is the voltage drop across the shunt resistor and R is the effective resistance of the shunt resistor.

The shunt resistor can be connected either on the capillary side or on the substrate side (Fig. 3.2 shows the current measurements on the substrate side), to measure the printing current delivered to the meniscus or dissipated from the substrate to the ground, respectively.

Furthermore, the charge transferred during ejection of colloidal suspensions is calculated by

$$\mathrm{Q} = \int I dt. \tag{3.4}$$

The value of the shunt resistor is chosen according to the order of magnitude of the printing current, which is estimated as follows. Let us denote r as the radius of the droplet ejected, f as the frequency of the droplet ejection, hence the period as $\mathrm{t} = \frac{1}{f}$, and U as the bias voltage across the capillary and the substrate.

Assuming that the liquid to be a perfect conductor[5], the droplet is an equipotential body with potential U. The charge carried by the droplet is given by

$$\mathrm{Q} = \mathrm{UC} \tag{3.5}$$

where C is the self-capacitance of the droplet. The self-capacitance of a spherical conductor is given by

$$\mathrm{C} = 4\pi\varepsilon_0 r. \tag{3.6}$$

Thus, the printing current can be estimated as

$$\mathrm{I} = \frac{Q}{t} = 4\pi\varepsilon_0 r U f \tag{3.7}$$

For typical values of the printing parameters r = 15 μm, f = 10 kHz, $\mathrm{t} = \frac{1}{f} = 100\ \mu s$ and U = 3 kV, the printing current is estimated to be 50 nA,

$$\mathrm{I} = 4\pi\varepsilon_0 r U f \approx 50\ nA \tag{3.8}$$

The noise level of the digitizer is approximately 5 mV. In order to achieve a signal to noise ratio (SNR) of 10, the voltage drop across the shunt resistor should be $U_d \approx 50\ mV$. Thus the effective shunt resistance must be

$$R_e = \frac{U_d}{\mathrm{I}} \approx 1\ M\Omega \tag{3.9}$$

Hence, the shunt resistor of $R_s = 2\ M\Omega$ was chosen. The input resistance of the digitizer is $R_i = 1\ M\Omega$. The effective shunt resistance is the shunt resistor in parallel with the input resistor of the digitizer, which can be calculated by

[5] This assumption will be further discussed based on the leaky dielectric model later in this chapter.

$$R_e = \frac{R_s R_i}{R_s + R_i} = \frac{2}{3}\ M\Omega \tag{3.10}$$

Usually the effects from the input resistance of the voltage measuring device is negligible as it is much larger than the value of the resistor to be measured, thus the effective resistance is close to the actual resistance of the resistor. However here in our application, as the current to be measured is very small, the value of the shunt resistor has been chosen comparable to the input resistance of the digitizer, thus the input resistance of the digitizer should be taken into consideration.

3.2.2. Identification of the EHD Ejection Modes

The current measurements from different EHD ejection modes have different characteristics due to different natures of how the colloidal suspensions are ejected from the capillary tip. Hence, in the experimental apparatus, the printing current measurement module is capable of recognizing different EHD ejection modes, including dripping mode, pulsation mode, cone jet mode, and complex jet modes (tilted jet mode, twin jets mode and multi-jet mode).

3.2.2.1. Dripping Mode

In dripping mode, the bias voltage is relatively small hence the mechanical driving force is the dominant cause of ejection. The bias voltage is not large enough to support the formation of a conical shape at the tip of the meniscus. So the pendant drops pinch off from the nozzle end mainly due to the gravitational force. Additional electrostatic force from the electric field counters the surface tension and helps the gravitational force to pinch off the droplets. As a result, dripping mode happens at a much slower rate than the other modes (typically < 1 Hz) and the droplets are large, comparable or even larger than the dimension of the nozzle.

A series of snapshots from high speed recording of the dripping mode and the corresponding current measurement plots are shown in Fig. 3.4.

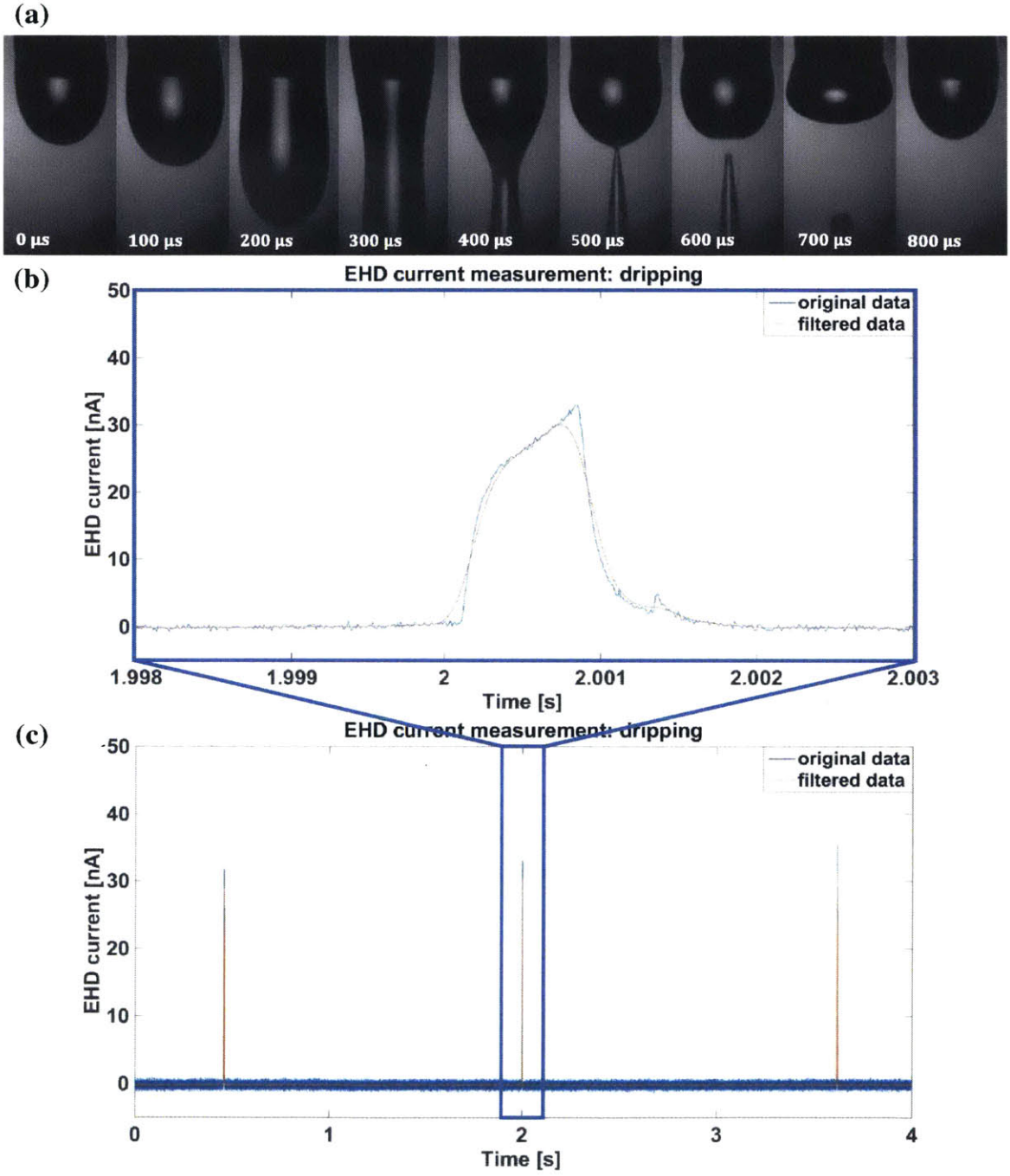

Fig. 3.4 Measurements of the printing current in the EHD dripping mode: (a) A series of snapshots of the ejection process; (b) Zoom in plot of the current measurements of one droplet ejection; (c) Plot of the current measurements of a sequence of droplet ejections.

Hence, in the corresponding current measurement plots, the separation between the peaks are long (usually more than 1 s, the frequency is usually smaller than 1 Hz as stated above) and the amplitude of the current is smaller (absolute value depends on the printing parameters) compared to other modes.

3.2.2.2. Pulsation Mode

Pulsation mode is a transition mode from dripping mode to cone jet mode. When the bias voltage is increased, the electrostatic force increases and is more dominant than the gravitational force in driving the ejection of colloidal suspensions.

The electric stress is large enough to support the formation of a conical meniscus at the tip of the capillary. Only a small portion at the tip of the meniscus oscillates and ejects colloidal suspensions in the form of either short jets or small droplets, which are 1~2 orders of magnitude smaller than the dimension of the nozzle. A series of snapshots from high speed recording of pulsation mode and the corresponding current measurement plots are shown in Fig. 3.5.

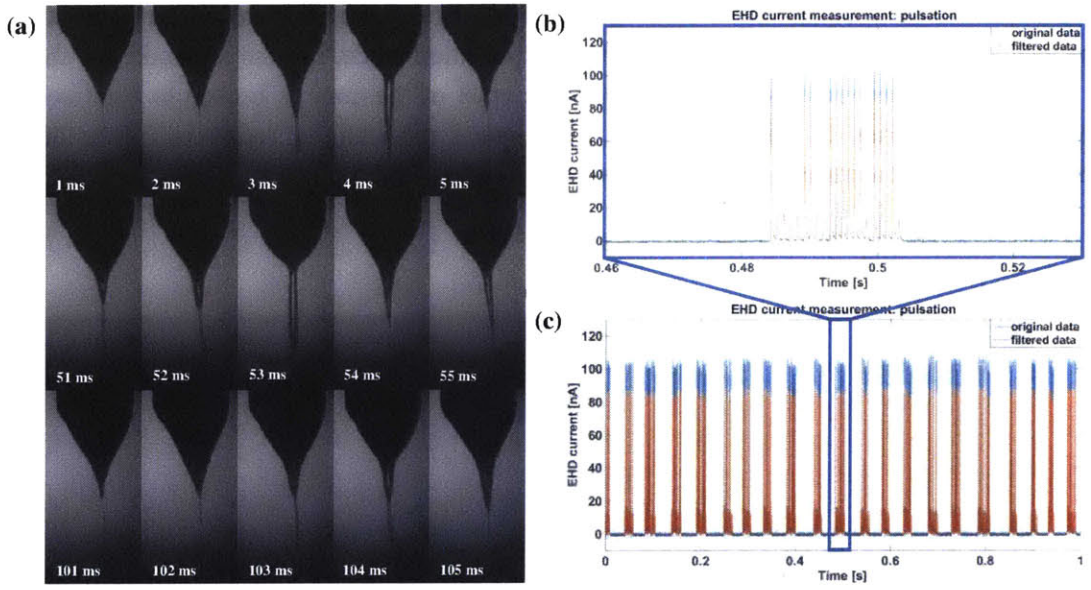

Fig. 3.5 Measurements of the printing current from the EHD pulsation mode: (a) A series of snapshots from the ejection process, each row represents one low frequency pulse; (b) Zoom in plot of the current measurements of one low frequency pulse which contains bunch of ejections; (c) Plot of the current measurements of a sequence of low frequency pulses.

Pulsation mode consists of two different frequency components [86]:

1. The low frequency component consists of a sequence of emission pulses with frequency in the range of 10~100 Hz. This frequency component is due to an imbalance between the addition of colloidal suspensions to the cone volume and their removal via the sequence of emission pulses.
2. The high frequency (~kHz) component consists of a series of short jets or small droplets within one of the low frequency pulses. The number of the droplets/jets contained in one of the low frequency pulses typically vary from ~1-100, according to the printing parameters. This frequency component is related to the transient emission of colloidal

suspensions via a cone jet and are caused by an imbalance between the emission rate of colloidal suspensions and their supply rate to the apex of the cone.

Hence, the corresponding current measurement plots consist of both the low and high frequency components: a sequence of long current pulses (f ≈ 10~100 Hz) form the envelopes for tens of short current spikes due to the ejection of small droplets/short jets (f~kHz).

3.2.2.3. Cone Jet Mode

Cone jet mode is operated by applying a steady flow of liquid using the plunger and the bias voltage deforms the meniscus to form a stable conical meniscus at the tip of the nozzle, after which a fine, stable and continuous jet is ejected out from the apex of the cone.

The balance between the rate of removal and supply of colloidal suspensions to the apex of the cone enables stable and continuous jetting. Unlike pulsation mode, in cone jet mode, the shape of the conical meniscus remains stable and only the apex of the cone is broken to eject colloidal suspensions. A series of snapshots from high speed recording of cone jet mode and the corresponding current measurement plots are shown in Fig. 3.6.

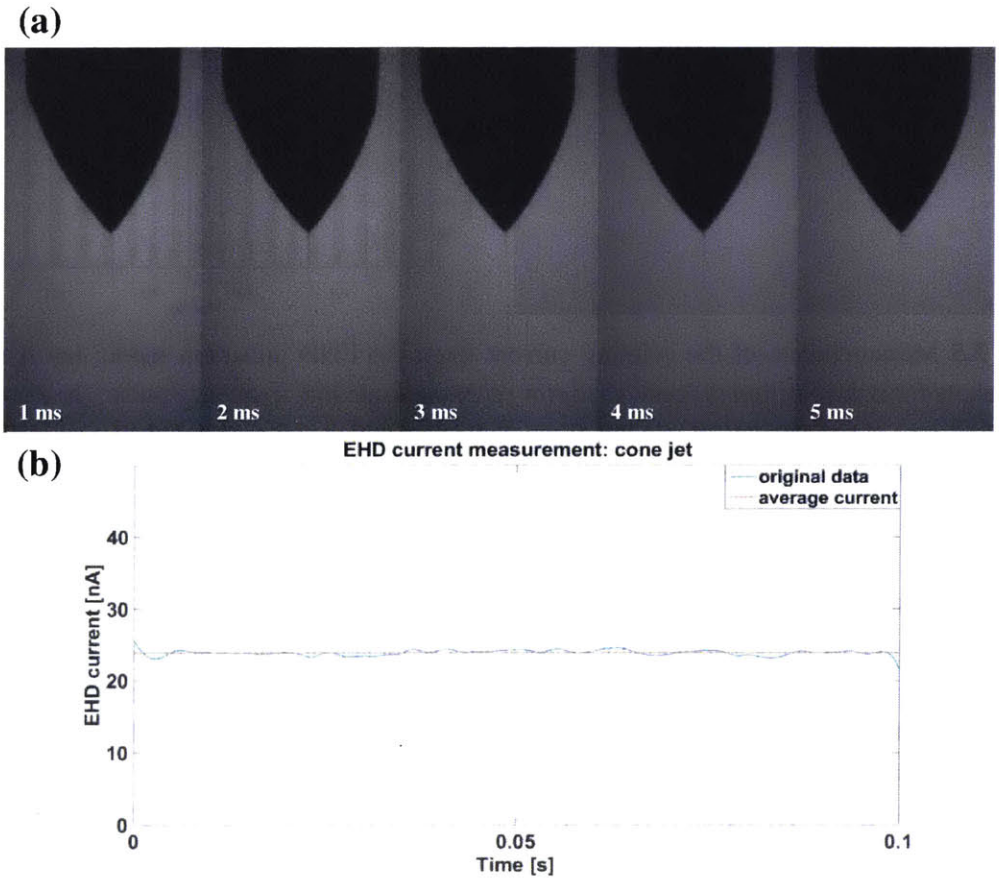

Fig. 3.6 Measurements of the printing current from the EHD cone jet mode: (a) A series of snapshots of the ejection process; (b) Plot of the measurements of the printing current.

Hence, the printing current measured during the cone jet mode of ejection is ~constant.

3.2.2.4. Complex Jet Modes

When the bias voltage is increased further, the electrostatic force becomes much larger than the force due to surface tension and the conical meniscus is hard to maintain and complex jet modes ensue. Usually the jet starts to lean towards one side and the axes of the cone may spin about the axis of the capillary and hence this is known as tilted jet mode. In addition, more than one jet will be ejected from the meniscus as the magnitude of the electrostatic pressure exceeds the local pressure difference due to surface tension at multiple locations on the meniscus, which further induces jets. A series of snapshots from high speed recording of complex jet modes (including tilted jet mode, twin jets mode and multi jets mode) and the corresponding current measurement plots are shown in Fig. 3.7.

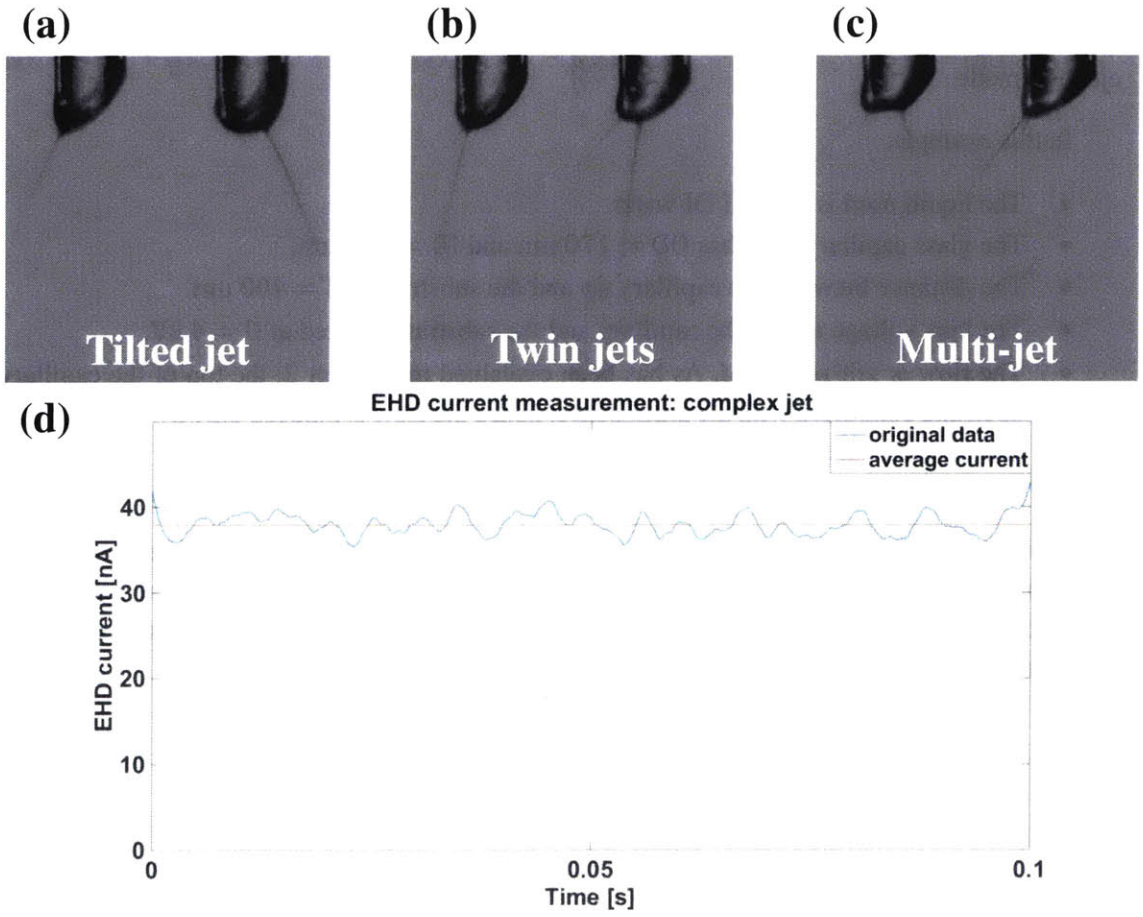

Fig. 3.7 Measurements of the printing current from the EHD complex jetting modes: (a) Snapshots from the ejection process of the tilted jet mode; (b) Snapshots from the ejection process of the twin jets mode; (c) Snapshots from the ejection process of the multi-jet mode; (d) Plot of the measurements of the printing current.

Though the shapes of the meniscus and the jets are complex and unstable, the current measured during this mode still remains constant, since the ejection is continuous enabled by the constant bias voltage and plunger driven external flow rate. However the amplitude of the current is larger than that of the cone jet mode given the same set of printing parameters and this fact can be used to distinguish the cone jet mode from the complex jet modes.

As described above, using measured printing current signatures we are able to distinguish different EHD ejection modes. One future direction of this capability is to achieve automatic mode-controlled EHD ejection, which is one of the requirements to use EHD driven printing of colloidal suspensions as a mass manufacturing technique for industrial applications.

3.2.3. Correlation of Printing Events

Here it is shown how the measurements of printing current can be correlated with the synchronized high speed videos to identify individual printing events under the pulsation EHD ejection mode.

In this example:

- The liquid used is type III DI water.
- The glass capillary used has OD = 170 μm and ID = 100 μm.
- The distance between the capillary tip and the substrate is d = 400 μm.
- The bias voltage across the capillary and the substrate is fixed at U = 4 kV.
- The flow is self-regulated. As has been explained in Chapter 2, the top of the capillary is open and connected with the atmosphere, hence the flow is induced only by the bias voltage and the flow rate is a function of the bias voltage.

Pulsation mode is the EHD ejection mode where the ejection has two different frequency components (which has been shown in Fig. 3.8): the low frequency component consists of a sequence of emission pulses and the high frequency component consists of a series of short jets or small droplets within each of the low frequency pulses.

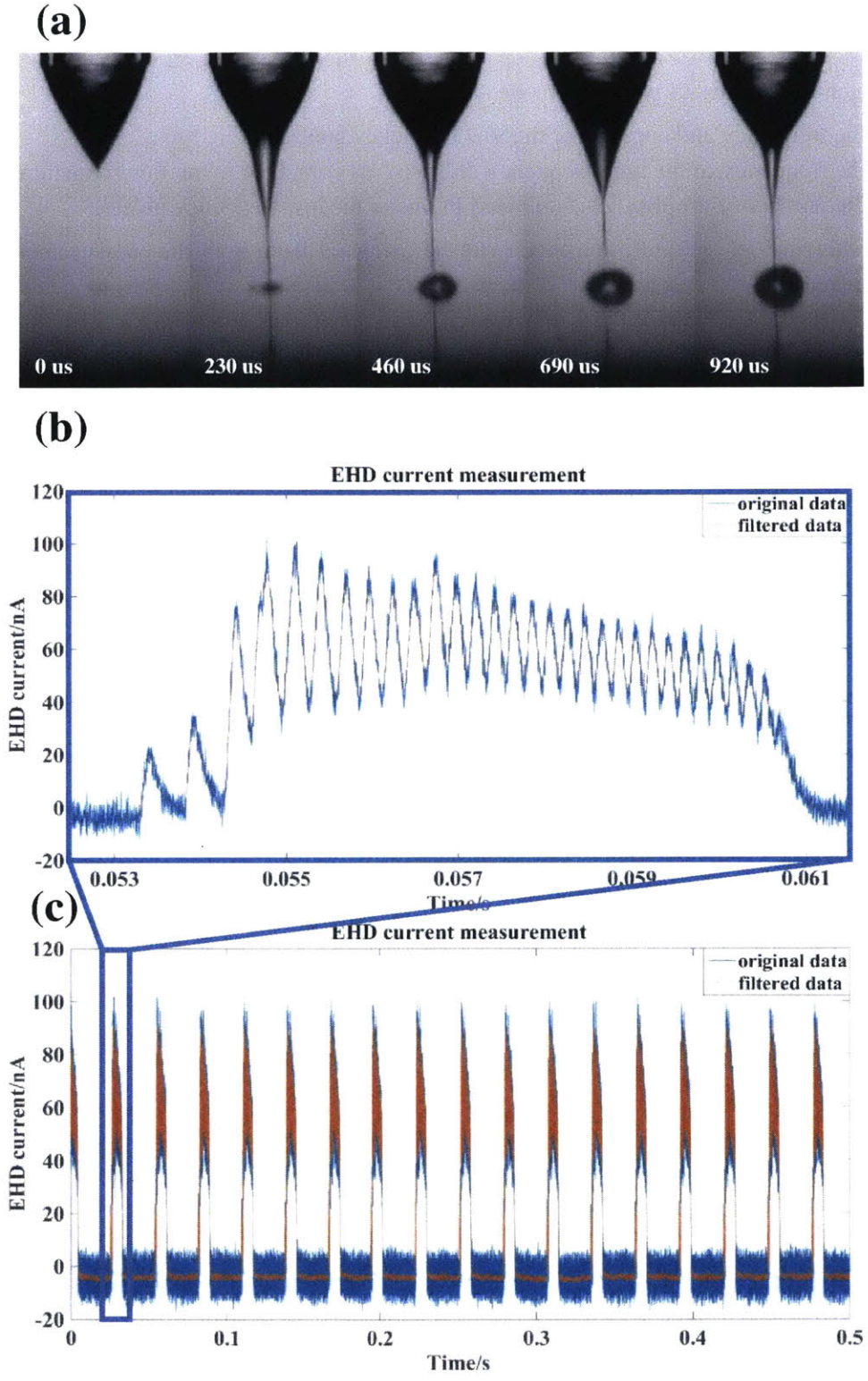

Fig. 3.8 Correlation of the measurements of printing current with the synchronized high speed videos: (a) A series of snapshots from the ejection process of the pulsation mode; (b) Zoom in plot

of the current measurements from one low frequency pulse; (c) Plot of the current measurements of a sequence of low frequency pulse.

Hence the characteristics of pulsation mode are:

1. The frequency and duration of the low frequency pulses.
2. The frequency of the high frequency droplets/jets contained in the low frequency pulses.
3. The number of droplets/jets contained in one of the low frequency pulses.

The characteristics of the pulsation mode can be extracted from both the measurements of the printing current and the synchronized high speed videos, which are summarized in Table 3.3.

Characteristics	From the measurements of printing current	From the high speed videos[6]
Frequency of the low frequency pulses	37.5 Hz	38.0 Hz
Duration of the low frequency pulses	7.9 ms	8.0 ms
Frequency of the high frequency droplets/jets	3.9 kHz	4.3 kHz
Number of the droplets/jets contained in one of the low frequency pulses	31	33

Table 3.3 Comparison of the characteristic information of the pulsation mode obtained from the current measurements and the high speed videos.

As can be seen from table, there is a good agreement between the quantities obtained from the measurements of printing current and high speed videos[7]. Hence we are able to correlate individual printing events from the high speed videos with the measurements of printing current. More specifically, in pulsation mode from this example, one short peak corresponds to one high frequency droplet/jet ejection and one long peak represents one low frequency pulse which contains the ejection of tens of small droplets/jets.

Further, we can apply a scaling analysis to verify the accuracy of the printing current measurements as follows. In this example, though type III DI water is used, it could still be treated as a perfect conductor according to Prof. D. A. Saville's leaky dielectric model [32].

From the measurements of printing current and the synchronized high speed videos, the fastest mechanical time scale, which is the period of high frequency pulses contained in the low frequency pulses, is

[6] The measurement were performed by counting the number of frames in the high speed videos. The start and the end of the pulse/spike of the printing current was indicated by the breakup of the Taylor cone and the contact of the droplet with the substrate, respectively.

[7] In this example, the measurements of printing current are characteristic information from the substrate side, while the high speed videos are that from the capillary side. They present good agreements.

$$\tau_m \approx 2.7 \times 10^{-4} s \tag{3.11}$$

The electrical time scale is the electrical relaxation time, defined as

$$\tau_e = \frac{\varepsilon \varepsilon_0}{\sigma} = 2.8 \times 10^{-5} s \tag{3.12}$$

where $\varepsilon = 80.1$ is the permittivity of type III DI water at 20 °C and $\sigma = 2.5 \times 10^{-5}$ S/m is the conductivity of the type III DI water. In this example, $\tau_e \ll \tau_m$ indicates that the timescale for charge redistribution of the droplet to achieve another equipotential state due to mechanical perturbation is much smaller than the timescale of its geometrical deformation due to EHD ejection, thus the liquid behaves more like a conductor than a dielectric.

From the high speed videos, the average droplet size leaving the meniscus can be measured by counting the number of pixels, and the typical value measured is

$$\mathrm{D} \approx 29\ \mu\mathrm{m} \tag{3.13}$$

The total charge transferred within one of the low frequency pulses can be integrated from the measurements of printing current

$$\mathrm{Q} = \int I dt \approx 2.58 \times 10^{-10}\ C \tag{3.14}$$

Hence the average charge transferred by one droplet measured from the digitizer is

$$\mathrm{q} = \frac{Q}{N} \approx 8.32 \times 10^{-12}\ C \tag{3.15}$$

where N=31 is the number of droplets contained in one of the low frequency pulses.

As has been explained above, in this example the droplets can be treated as conductors so their self-capacitances are that of a spherical conductor given by

$$\mathrm{C} = 4\pi\varepsilon_0 r \approx 1.62 \times 10^{-15}\ F \tag{3.16}$$

Thus the charge transferred by one droplet is estimated to be

$$q' = UC \approx 6.49 \times 10^{-12}\ C \tag{3.17}$$

which has a good agreement with the transferred charge measured from the digitizer. The difference between the estimated and measured charge transfer value can be attributed to the inaccuracy of the digitizer to measure ~10nA current and the assumption of the leaky dielectric model.

3.3. Experimental Methods

This section outlines the general experimental procedure for inducing EHD ejection of colloidal suspensions to print desired patterns onto the substrate, and observing and characterizing the entire printing process.

As explained in section 3.1 bove, there are two main driving forces in the single-tip printhead experimental apparatus to induce the ejection of colloidal suspensions: 1) mechanical driving force via plunger motion to push the colloidal suspensions out of the capillary; 2) electrical driving force via the bias voltage across the capillary and the substrate to pull the colloidal suspensions out of the capillary.

Accordingly, there are mainly two different EHD ejection mechanisms in our experiments, mode-controlled continuous jetting and on-demand printing, which are different methods of incorporating the two driving forces.

1. Mode-controlled continuous jetting:
   The two driving forces are applied simultaneously to induce the ejection of colloidal suspensions. The plunger motion speed and, hence the external flow rate and the bias voltage are fixed as constants in this method to determine the EHD ejection modes. When the substrate translates in the XY plane, desired patterns, including dot arrays (onto hydrophobic substrate, due to Plateau-Rayleigh instability) and continuous lines (onto hydrophilic substrate) can be printed. This mechanism is illustrated in Fig. 3.9.

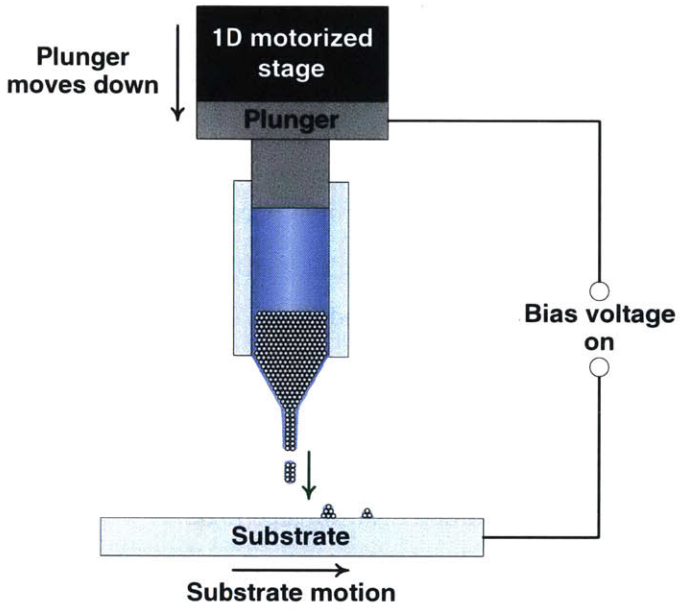

Fig. 3.9 Schematic of the mode-controlled continuous jetting mechanism.

2. On-demand printing:
   The two driving forces are applied in turn to induce the ejection of colloidal suspensions in an on-demand fashion. Without plunger motion, the bias voltage alone cannot induce printing as the colloidal suspensions will be confined in the capillary due to atmospheric pressure. In this mechanism, plunger motion supplies the colloidal suspensions to the tip of the capillary and the bias voltage induces printing. The plunger jogs down to form a free standing meniscus at the tip of the capillary, which remains stable due to surface tension. Afterwards short bias voltage pulses are applied to drag the colloidal suspensions out from the capillary onto the substrate. The EHD ejection modes and the amounts of the colloidal suspensions being ejected depend on the free standing volume, pulse amplitude and duration. This process is on demand compared to continuous jetting mechanism since: when to eject colloidal suspensions and how much colloidal suspensions will be ejected

are determined by the timing of the applied voltage pulses, free standing volume, as well as the amplitude and duration of the pulses. This mechanism is illustrated in Fig. 3.10.

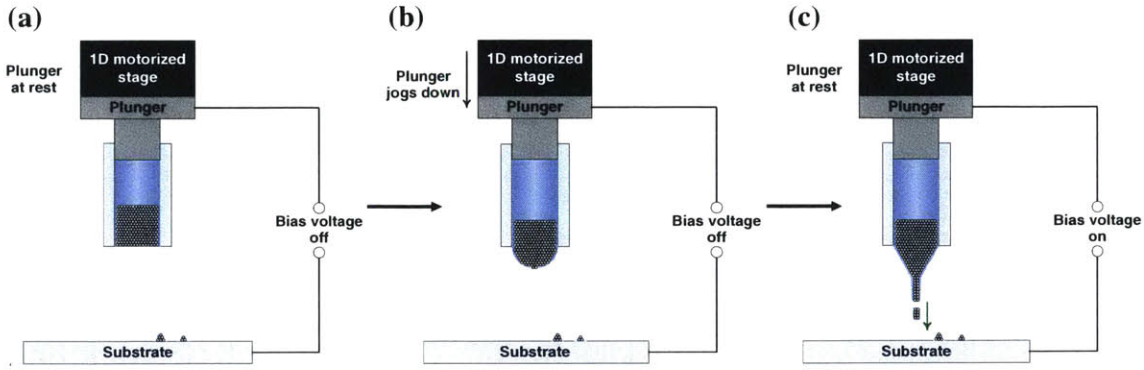

Fig. 3.10 Schematic of the mechanism of the on-demand printing: (a) Before printing: plunger is at rest and the bias voltage is off; (b) Printing starts: plunger jogs down to form a freestanding volume at the tip of the capillary and the bias voltage is off; (c): Stop the motion of the plunger and turn on the bias voltage to induce printing.

As has been explained above, in our experimental apparatus, the whole printing process is observed and characterized via three synchronized signals:

1. Visual observation via the high speed camera recording.
2. Measurements of the current and charge transfer during printing.
3. The high speed high amplitude bias voltage printing signals.

The three signals together provide us comprehensive information to investigate the underlying physics of the EHD printing of colloidal suspensions for additive manufacturing.

this page intentionally left blank

Chapter 4: Mode-Controlled Continuous EHD Jetting

In this chapter, we will demonstrate the capability of the experimental apparatus of printing microparticle patterned dot arrays and continuous lines via the mode-controlled continuous EHD jetting mechanism. Two different types of colloidal suspensions which contain 3 μm diameter polystyrene (PS) microparticles and 3 μm diameter alumina microparticles are used respectively. A mathematical model to predict the radius and spacing of the dot arrays is proposed and compared with the experimental data as well.[8]

4.1. Process Requirements

As has been explained in Chapter 3, in the mode-controlled continuous jetting EHD scheme (Fig. 3.9), constant bias voltages across the capillary and the substrate and constant external flow rates enabled by the motorized plunger motion are applied to the printing system. The combination of the amplitude of the bias voltage and the external flow rate determines the EHD ejection mode (Fig. 2.5).

In order to deposit colloidal suspensions onto the substrate to form a fine, continuous and uniform line in the first place right after ejection, apart from the constant flow rate of ejection, there are two more requirements:

1. **The substrate is required to move in a constant velocity.**
   Denote v as the velocity of the motorized substrate motion, q as the external flow rate of the EHD ejection, and θ as the contact angle of the colloidal suspensions on the substrate. Hence the width of the initial printing line right after ejection can be calculated by (Fig. 4.1)

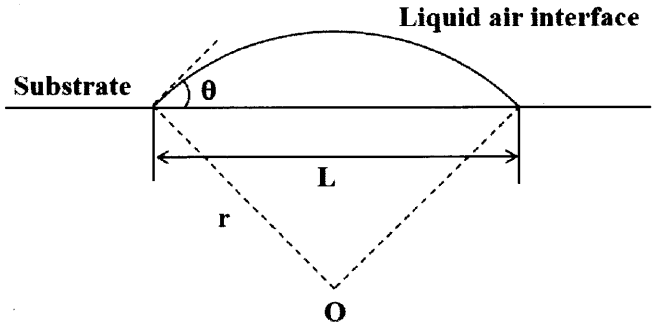

Fig. 4.1 Schematic of calculating the initial line width.

[8] The results shown in this chapter were initially done as the final project of the course 18.357 Interfacial Phenomena, thanks to Prof. John Bush for his efforts in organizing the awesome lectures and helping with the project.

$$L = 2r \sin\theta \tag{4.1}$$

where r is the diameter of the cross section of the printed line, which can be calculated by

$$\theta r^2 - \sin\theta \cos\theta r^2 = A \tag{4.2}$$

and A is the cross sectional area of the printed line, given by

$$A = \frac{q}{v} \tag{4.3}$$

2. **The subsequent ejections of droplets/jets are required to overlap with each other on the substrate.**

   Therefore the cone jet mode where colloidal suspensions are ejected in a continuous, uniform and stable fashion, and the pulsation mode which is capable of positioning droplets with sizes 1~2 orders of magnitude smaller than the dimension of the capillary at kHz rate, are favorable. Additionally, in the pulsation mode, as colloidal suspensions are deposited onto the substrate in a discrete fashion, two more requirements to enable the overlapping of the subsequent droplets after being deposited on the substrate: 1) The ejection is within one low frequency pulse through the motion of the substrate, which is ensured by inspection from the high speed camera; 2) The projected distance of the two droplets which are ejected successively on the substrate should be much smaller than their diameters, in order to guarantee their overlapping and to form a continuous line on the substrate. This can be expressed by

$$\frac{v}{f} \ll d \tag{4.4}$$

   where f is the frequency of the high frequency component of the pulsation mode, d is the diameter of the ejected droplets. For a typical set of parameters observed in our experiments: $v = 2$ mm/s, $f = 10$ kHz, $d = 10$ μm, we can verify that

$$\frac{v}{f} = 0.2\ \mu m \ll d = 10\ \mu m \tag{4.5}$$

   This satisfies equation (4.4), hence the formation of the initial continuous lines right after ejection can be guaranteed.

After the sequence of continuous jets or overlapping droplets has been deposited onto the substrate, the final patterns consisting of the colloidal suspensions which remain on the substrates have two different conditions according to previous literatures [87,108]:

- For substrates with low wettability, the lines will break up into separated droplets due to Plateau-Rayleigh instability, as the interface between the colloidal suspensions and the substrate must be minimized to minimize the total surface energy of the system. When the breakup time scale is much smaller than the time scale for the solvent to evaporate, dot arrays composed of the microparticles will be left on the substrate after the solvent dries out. The process is illustrated in Fig. 4.2.
- For substrates with high wettability, the line will remain stable due to the pinning of contact lines hence a continuous line composed of microparticles will be left on the substrate after the solvent dries out.

These two distinct cases have been observed in our experiments with substrates of different wettabilities, which will be demonstrated below.

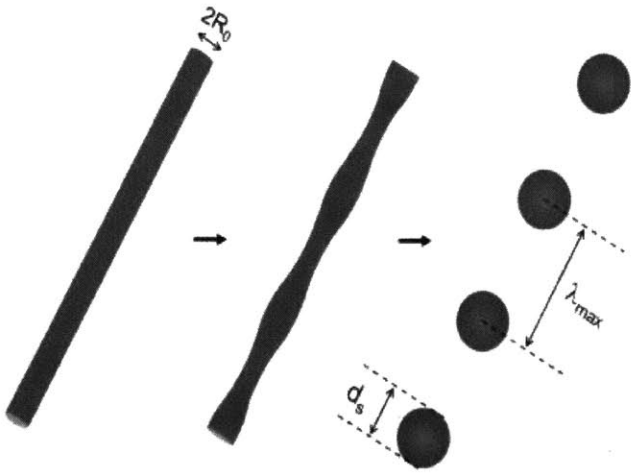

Fig. 4.2 Breakup of the initial continuous line due to Plateau-Rayleigh instability. [109]

4.2. Experimental Methods

In this section, we will briefly explain the procedures of the continuous EHD jetting experiments and the parameters of the model system.

4.2.1. Experimental Procedures

Colloidal suspensions containing 3 μm diameter PS microparticles (Polybead® Microspheres 3.00 μm from Polysciences, Inc.) and 3 μm diameter alumina microparticles (Plain Alumina Microspheres 3 μm from Corpuscular Inc.) in water solution are mixed with glycerin with a volume fraction of 1:1. Glycerin is added to increase the viscosity of the solvent in order to facilitate the formation of the cone jet mode or the pulsation mode. The mixtures are then mixed and sonicated for 20 minutes before use, to ensure sufficient mixing and reduce the aggregation of microparticles. The syringe (without the needle connected) is filled with a water glycerin mixture with a volume fraction of 1:1 and make sure there are no air bubbles introduced by inspection. The plunger is pressed down to form a convex meniscus at the nozzle of the syringe and then carefully connected with the needle to prevent any air bubbles from being trapped on the interface of the syringe and the needle. Next, the plunger is further pushed down to fill the needle with the solvent and form a convex meniscus at the tip of the needle. Afterwards the tip of the needle is dipped into the vial which contains the colloidal suspensions and make sure that the meniscus at the needle tip directly contact the interface of the colloidal suspensions by inspection from the high speed camera, in order to prevent any air bubbles from being trapped on the interface of the needle and the colloidal suspensions. Then the colloidal suspensions are loaded into the needle and syringe by pulling up the plunger using its attached motorized stage. After the colloidal suspensions have been loaded, the bias voltage is turned on and the plunger starts to move down. The appropriate values of the amplitude of the bias voltage and the external flow rate are chosen to ensure that either the cone jet

mode or the pulsation is achieved for the EHD printing of colloidal suspensions, by inspection from the high speed camera. The substrate then moves via its attached motorized stage after the appropriate EHD ejection mode has been achieved. Thereby the initial continuous lines will be deposited onto the substrate.

4.2.2. System Parameters

We will use the colloidal suspensions containing 3 μm diameter PS microparticles mentioned above as the model system, to investigate how dot radii and spacings are dependent on the printing parameters and compare with previous studies as well.

1. Colloidal suspensions

The as purchased PS microparticle suspensions are dispersed in deionized (DI) water with a volume fraction of 2.5%. The final colloidal suspensions after glycerin has been added consist of 1.25% PS microparticles, 48.5% water and 50% glycerin, all in volume fraction.

The important properties of the colloidal suspensions involved in this problem are the surface tension, density and viscosity. The values can be found from previous literatures which worked on measuring the properties of water glycerin mixture [88,89]. The contributions of the PS microparticles can be calculated using a model of effective viscosity below. The values of the surface tension, density and viscosity of the colloidal suspensions are listed as follows (detailed calculation are not presented for simplicity): surface tension $\sigma \approx 0.0506$ N/m, density $\rho = 1037$ kg/m^3, viscosity $\mu = 0.046$ Pa · s.

The viscosity μ listed above has already taken into the contribution of the PS microparticles. The presence of the PS particles increases the viscosity of the colloidal suspensions, the contribution is calculated via a modified Einstein's effective viscosity model [90-92]. The relative viscosity of the colloidal suspensions with respect to that of the solvent is given by

$$\mu_r = 1 + 2.5\phi + 10.05\phi^2 + Ae^{B\phi} \tag{4.6}$$

where A=0.00273 and B=16.6 are constants, ϕ is the volume fraction of the PS microparticles. The relative viscosity of the colloidal suspensions only depends on ϕ while does not rely on the size of the microparticles, as long as they are monodisperse microparticles. Hence the absolute viscosity of the colloidal suspensions can be calculated by

$$\mu = \mu_r \mu_l \tag{4.7}$$

where μ_l is the original viscosity of the solvent without any PS microparticles inside.

2. Geometric parameters

The needles used here are glass capillaries purchased from Hilgenberg GmbH, with ID = 82 μm and OD = 120 μm. The distance from the capillary tip to the substrate is fixed at 1 mm.

3. Printing input parameters

In the continuous EHD jetting experiments, there are three input parameters we can vary in order to print dot arrays with different radii and spacings. The parameters and the corresponding ranges are:

- The bias voltage: $U = 1.2 \sim 1.5$ kV.
- The external flow rate: $q = 5 \sim 150$ nL/s.
- The speed of the substrate motion: $v = 0.5 \sim 24$ mm/s.

The combination of the bias voltage and the external flow rate is determined in order to generate either the cone jet mode or the pulsation mode.

4. Contact angle

The substrates are glass microscope slides covered with copper tapes in order to increase the contact angle. The static contact angle of the colloidal suspensions (with glycerin added) on the substrate is measured to be $\theta \approx 90^{\circ}$ by optical imaging.

4.3. Printing Dot Arrays

Fig. 4.3 shows the preliminary results of printing dot arrays onto substrates with low wettability. The colloidal suspensions are composed of 3 μm diameter PS microparticles. The leftmost picture is an optical image of dot arrays with different radii and spacings taken by a digital camera. The large dots on both of the top and bottom sides of the arrays are the starting and ending points of the printing, respectively, which are formed simply due to the collection of colloidal suspensions instead of breakup due to Plateau-Rayleigh instability. The picture in the middle is a zoomed in microscope image of a dot array with a feature radius around 150 μm. The rightmost picture is a further zoomed in microscope image of one dot, where individual PS particles can be observed from the edge of the dot. The printing parameters are listed in the above section 4.2.2.

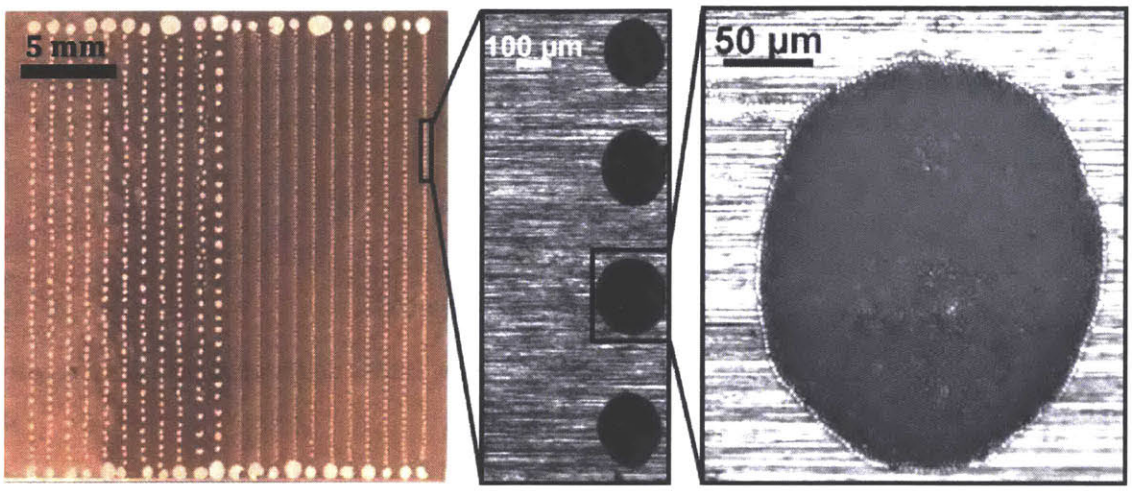

Fig. 4.3 Printed dot arrays consisting of 3 μm diameter PS microparticles with different feature sizes.

4.3.1. Experimental Results

We will rationalize the dependence of the radius and spacing of the dot arrays on the input parameters (including the bias voltage, the external flow rate and the substrate motion speed) and furthermore develop mechanisms to control the radius and spacing of the dot arrays. Dot arrays with different radii and spacings are printed and measured. The results are summarized as follows.

4.3.1.1. Dependence on the Bias Voltage

Fig. 4.4 shows the experiments when the external flow is fixed at 34 nL/s, varying the bias voltage and the substrate motion speed, the radii (Fig. 4.4(a)) and spacings (Fig. 4.4(b)) of the corresponding printed dot arrays.

(a)

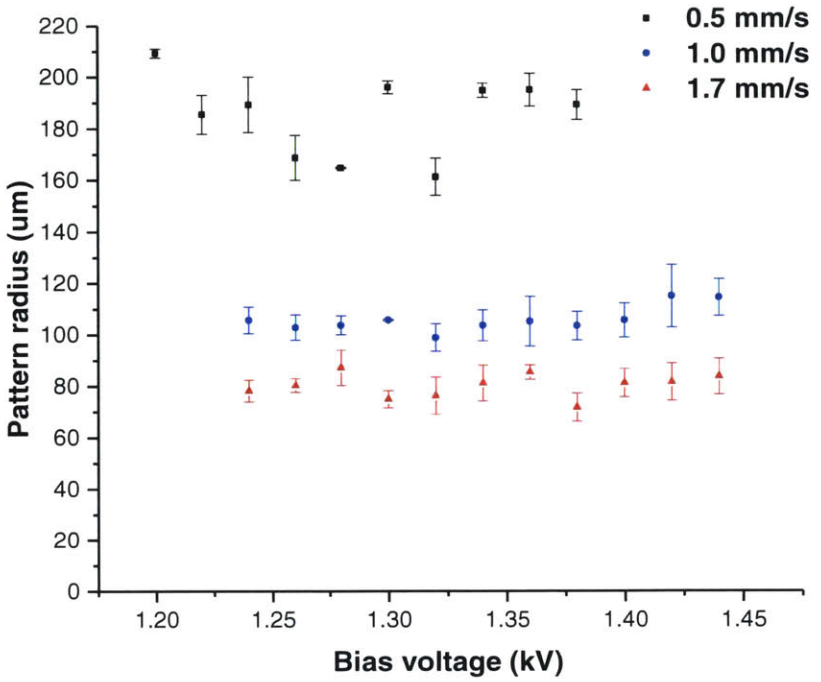

(b)

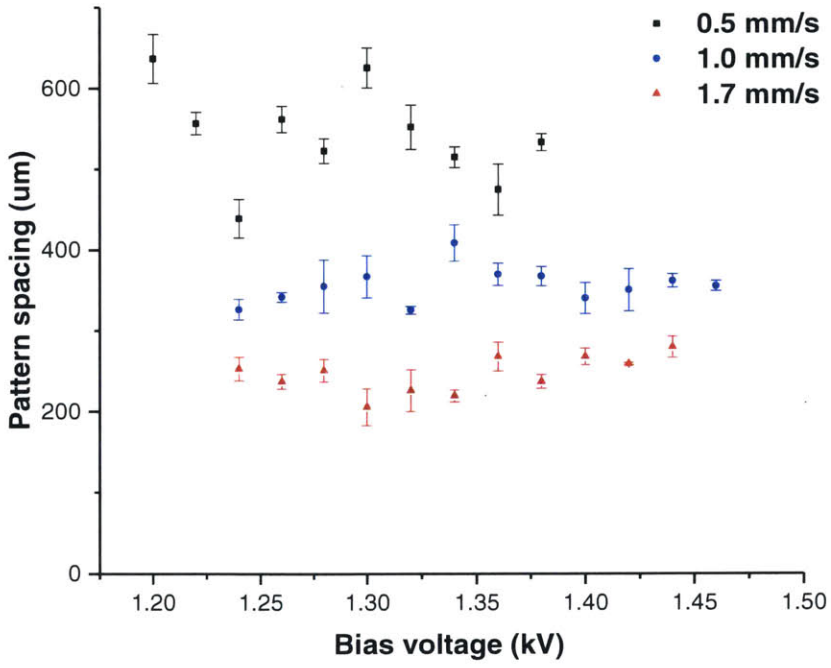

Fig. 4.4 The radius and spacing of the printed dot arrays with respect to the bias voltage and the substrate motion speed: (a) pattern radius; (b) pattern spacing.

Fig 4.4 shows that with a given substrate motion speed, though there are variations on both the radii and spacings of the dot arrays, there are no clear correlations between their trends with respect to the amplitude of the bias voltage. Therefore we can conclude that the bias voltage has no direct impacts on the radius and spacing of the dot arrays, as long as the cone jet mode or the pulsation mode is formed to guarantee the formation of the initial lines on the substrate in. This is because within the cone jet mode or the pulsation mode, the initial line width only depends on the external flow rate and the substrate motion speed (according to equation (4.1) - (4.3)), while the amplitude of the bias voltage only affects other parameters of the ejection excluding the flow rate. Hence for the experiments in Fig. 4.4 with the same substrate motion speed, the initial lines on the substrate are supposed to be the same, therefore the final patterns are the same. Though the bias voltage will not directly affect the radius and spacing of the dot array, according to the phase diagram of the EHD ejection modes (Fig. 2.5), it actually affects the achievable external flow rate which can be applied to guarantee the cone jet mode or the pulsation mode, therefore affects the achievable radius and spacing of the dot arrays in an indirect fashion.

The variations of the radius and spacing of the dot arrays measured in Fig. 4.4 may result from multiple sources, the main reasons we anticipate which cause the variations are: 1) the substrate is covered with copper tapes whose surface roughness may affect the uniformity of the of the breakup process; 2) the oscillations of the substrate during motion and the sputtering of the liquid when contacting the substrate affect the uniformity of the initial line width; 3) and the distribution of the PS microparticles affects the motion of the contact lines.

4.3.1.2. Dependence on the Substrate Motion Speed

From the Fig. 4.4 above, conclusions can be drawn that both of the radius and spacing of the dot arrays increase when decreasing the substrate motion speed v. This is intuitive as when the substrate moves slower, the width of the initial line will increase (the scalings will be discussed later in this section), thus resulting in dot arrays with larger radius and spacing.

4.3.1.3. Dependence on the External Flow Rate

Fig. 4.5 shows experiments when fixing the bias voltage at 1.36 kV and the substrate motion speed at 2.3 mm/s, varying the external flow rate q.

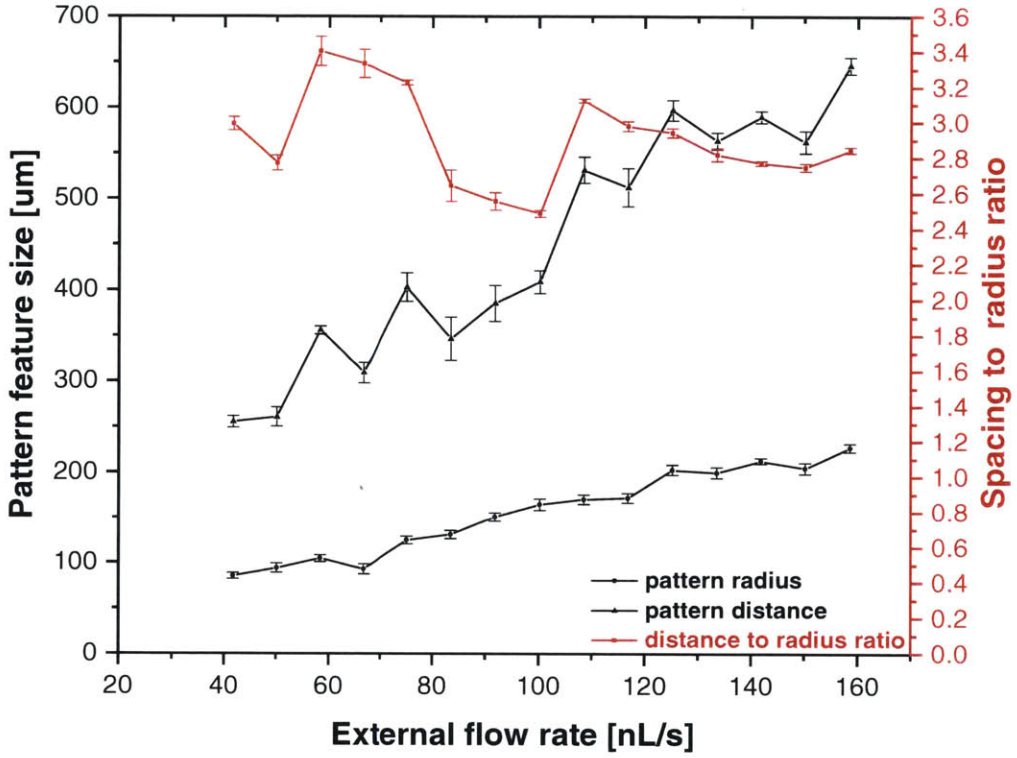

Fig. 4.5 The radius, spacing and spacing to radius ratio of the printed dot arrays with respect to the external flow rate.

The plots of the corresponding radius, spacing and spacing to radius ratio of the dot arrays are shown in Fig. 4.5. It is clear that both radius and spacing of the dot arrays increase while increasing the external flow rate. This is straightforward as well since the increase in the external flow rate will also result in the increase of the initial line width, hence increase the radius and the spacing of the dot arrays. The scaling will be discussed later in this section as well.

Moreover, though there are variations of the spacing to radius ratio of the dot arrays with respect to the external flow rate, there is no clear trend between them. In fact, this ratio is related to the dimensionless wave number corresponding to the fastest growing rate of Plateau-Rayleigh instability, which will be explained in the modeling part of this section later. We could conclude that the external flow rate has no clear influence on the spacing to radius ration, and hence the dimensionless wave number (will be verified in section 4.3.2 below). The origins of the variations on this ratio may result from the poor uniformity of the initial line width explained above.

4.3.2. Dimensional Analysis

In the following section, we will identify the dominant forces of the break up process via analysis of their order of magnitude, based on which the appropriate model is chosen to predict the radius and spacing of the dot arrays theoretically.

The break up process due to Plateau-Rayleigh instability has already been observed in our experiments. This process originates from the minimization of the total surface energy of the system, hence surface tension is obviously one of the dominant driving forces. In order to determine whether other forces, including gravitation force, inertial force and viscous force play a role, the corresponding dimensionless numbers are calculated as follows.

The characteristic length scale is $r_0 \sim 100\ \mu m$, which is the initial width of the lines. The characteristic breakup time scale t is unknown here. It can be measured carefully from the high speed recording of the break up process. However this has not been done as it is not necessary for the purpose of dimensional analysis. Though the exact breakup time scale is unknown, it is low bounded by the breakup time scale of inviscid fluid t_0 (as viscosity is a resisting force of the breakup process, hence t_0 is the fastest possible breakup time scale), which is sufficient for our analysis below.

It should be noted that we use the linear axisymmetric stability theory for a viscous jet to estimate the expected dominant wavelength because of the lack of a theory for capillary instability of viscous liquid filaments on substrates. This idea has been used by literatures working on similar problems (breakup of viscous liquid filaments on substrates) and the scaling relations derived from the models turn out to be in good agreements with the experiments [93].

Therefore the break up time scale of cylindrical lines composed of the colloidal suspension is low bounded by that of inviscid fluid, given by [94,95]

$$t \geq t_0 \sim 2.91\sqrt{\frac{\rho {r_0}^3}{\sigma}} \tag{4.8}$$

The capillary length λ_c is the characteristic length scale for an interface where the surface tension force is of the same magnitude as the gravitational force, here

$$\lambda_c = \sqrt{\frac{\sigma}{\rho g}} \approx \sqrt{\frac{5.06\times10^{-2}}{1.037\times10^{3}\times10}} \approx 2.21mm \gg L \sim 100\ \mu m \tag{4.9}$$

Therefore gravitational force is negligible compared with surface tension force.

The capillary number Ca compares the magnitudes of the viscous force versus the surface tension force, here

$$Ca = \frac{\mu v}{\sigma} = \frac{\mu r_0}{\sigma t} \leq \frac{\mu r_0}{\sigma t_0} = \frac{\mu}{2.91}\sqrt{\frac{1}{\sigma r_0 \rho}} \approx \frac{0.046}{2.91} \times \sqrt{\frac{1}{5.06\times10^{-2}\times50\times10^{-6}\times1.037\times10^{3}}} \approx 0.2 \tag{4.10}$$

Therefore surface tension force dominates over viscous force.

The Weber number We compares the magnitudes of the inertial force versus the surface tension force, here

$$We = \frac{\rho v^2 r_0}{\sigma} = \frac{\rho {r_0}^3}{\sigma t^2} \leq \frac{\rho {r_0}^3}{\sigma {t_0}^2} = \frac{1}{2.91^2} \approx 0.12 \tag{4.11}$$

Therefore surface tension force dominates over inertial force.

The Reynolds number Re compares the inertial force versus the viscous force, here

$$Re = \frac{\rho v r_0}{\mu} = \frac{\rho {r_0}^2}{\mu t} \leq \frac{\rho {r_0}^2}{\mu t_0} \approx 0.54 \tag{4.12}$$

Therefore viscous force is larger than inertial force, which indicates that viscosity does play a role in the breakup process. Hence viscosity should be taken into consideration when estimating the feature sizes of the dot arrays below.

In conclusion, surface tension, inertial force and viscous force should all be taken into consideration during this break up process, while gravitational force can be neglected.

When viscosity comes into play, the model of Plateau-Rayleigh instability used for inviscid liquid is not accurate enough anymore. The dispersion relations of the growth rate of the instability ω with respect to the dimensionless wavenumber x for viscous liquids have been investigated by previous researchers[9], which is given by

$$\omega^2 = \frac{\sigma}{\mu R_0} \frac{1-x^2}{2\left[\frac{x^2 I_0^2(x)}{I_1^2(x)} - (1+x^2)\right]} \tag{4.13}$$

where $I_0(x)$ and $I_1(x)$ are Bessel functions, R_0 is the initial radius of the line.

The family of the dispersion curves can be found in Figure 129 of ref 96 by Chandrasekhar [96]. In this figure the dimensionless number J which distinguishes different curves in the family is derived from the differential equation describing the instability, given by

$$J = \frac{\sigma R_0 \rho}{\mu^2} \tag{4.14}$$

Different curves correspond to different values of J.

The dispersion curves indicate that for any given solution, the dimensionless wavenumber x only depends on the initial radius of the line R_0, hence the wavelength can be formulated as

$$\lambda_{max} = f(R_0) R_0 \tag{4.15}$$

where $f(R_0)$ is a function of R_0 from the dispersion curves.

[9] Again here we are using the model of linear axisymmetric stability theory for a viscous jet.

From equation (4.2) and (4.3), the initial radius of the lines R_0 can be calculated via mass conservation. For the contact angle $\theta = 90^\circ$,

$$R_0 = \sqrt{\frac{2Q}{\pi v}} \tag{4.16}$$

Denote R as the radius of the droplets immediately after breaking up, via mass conservation

$$V' = \lambda_{max} A = \frac{1}{2}\pi f(R_0){R_0}^3 \tag{4.17}$$

where V' is the volume of single droplet immediately after breaking up. For the contact angle of 90°, the droplet has a semispherical shape, hence

$$V' = \frac{2}{3}\pi R^3 \tag{4.18}$$

Therefore,

$$R = \sqrt[3]{\frac{3}{4} f(R_0)} R_0 \tag{4.19}$$

Now, we will use R to estimate the radius of the patterns after the solvent dries out, assuming that: 1) due to coffee ring effect, PS microparticles will move towards the edge of the droplets [97]; 2) the contact lines will remain pinned throughout evaporation.

We will use data from the set of experiments where U = 1.36 kV, v = 2.3mm/s, q varies in the range of 20~160 nL/s, to compare with the above prediction model. The range of the corresponding R_0 in this input parameter range is $R_0 = \sqrt{\frac{2Q}{\pi v}} = 100\sim230\ \mu m$. For our colloidal suspensions, $J = \frac{\sigma R_0 \rho}{\mu^2} = 170\sim500$. Though this range of J cannot be referred in the dispersion curves, we notice that the dimensionless wavenumber x increases while increasing J. However, x cannot be larger than 1 otherwise the instability will not happen. Hence we can, to a sufficient approximation, estimate that $x \equiv 1$. Hence

$$f(R_0) = \frac{2\pi}{x} = 2\pi \tag{4.20}$$

and

$$R = 1.68\sqrt{\frac{2Q}{\pi v}} \tag{4.21}$$

The plots of the predicted and measured radii of the dot arrays are shown in Fig. 4.6.

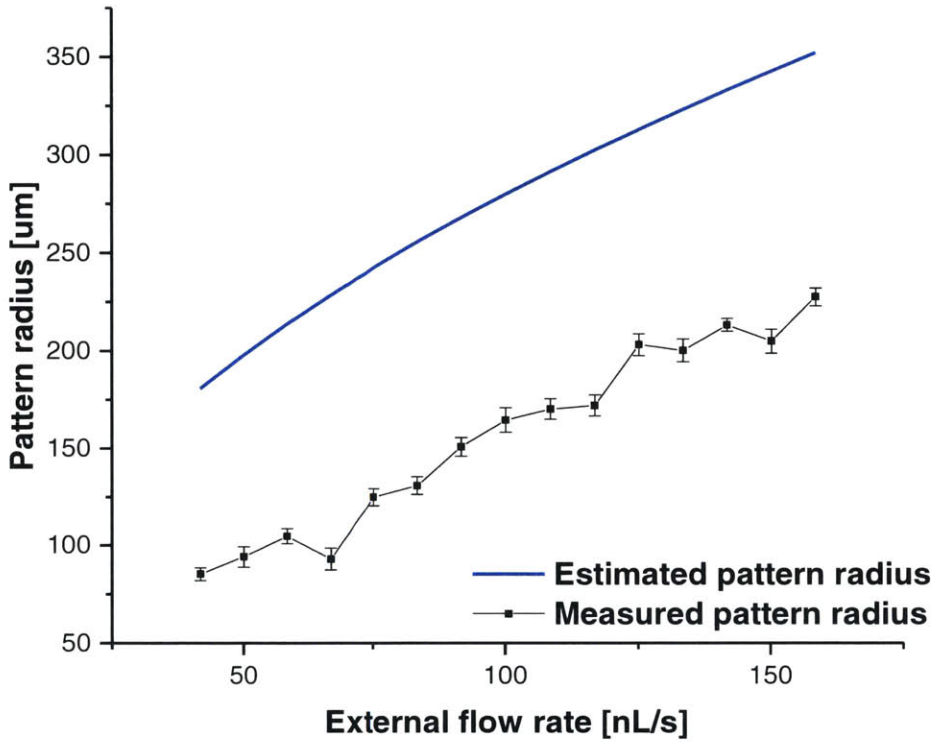

Fig. 4.6 Measured pattern radius versus estimated pattern radius.

According to the model above, when the bias voltage U and the substrate motion speed v are fixed, both the radius R and spacing s of the dot arrays scale with the square root of the external flow rate q, i.e., $R \sim \sqrt{q}$ and $s \sim \sqrt{q}$. The plots of R and s with respect to $\sqrt{Q}$, as well as their linear fits are shown in Fig. 4.7.

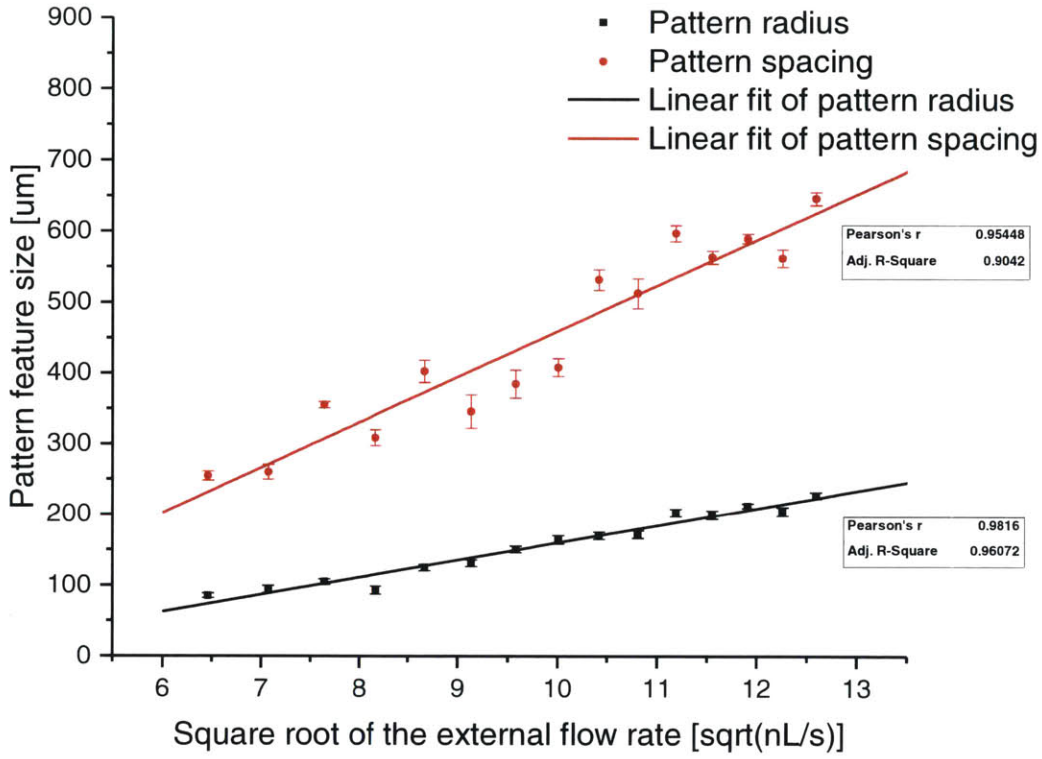

Fig. 4.7 The radius and spacing of the printed dot arrays with respect to the square root of the external flow rate, as well as their linear fits.

Therefore, conclusions can be drawn from Fig. 4.4 – 4.7 that

1. The overall trends of both the radius R and spacing s of the dot arrays agree with the model, i.e., increase with the external flow rate Q, roughly scale with $\sqrt{Q}$.
2. The spacing to radius ratio of the dot arrays is not dependent on the external flow rate in this set of the experiments, which agrees with the assumption that within the parameter space of our experiments, the dependence of the dimensionless wave number on the initial width of the lines is negligible.

However, we noticed that the actual radius of the dot arrays is significantly smaller than that from the estimation. Two possible reasons are:

- The presence of PS microparticles affects the hydrodynamics during the breakup process in addition to changing the effective viscosity.

- The contact lines are not completely pinned during evaporation. This has been observed from the high speed recording of the evaporation process. Fig. 4.8 shows a sequence of snapshots from a high speed video recording how the contact line jumps and shrinks during evaporation, which makes the radius of the pattern smaller than the radius of the droplet immediately after breaking up.
-

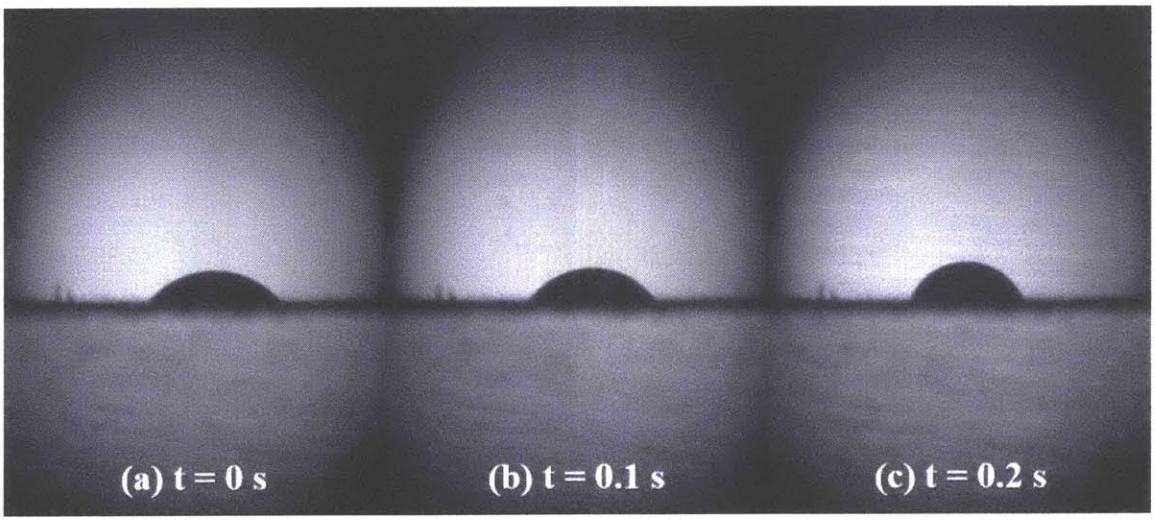

Fig. 4.8 A sequence of snapshots of high speed recording of the contact line jumping of the droplet during evaporation.

In order to reduce the radius of the dot arrays, one can (within the cone jet mode and the pulsation mode):

1. Decrease the external flow rate. This is limited by the diameter of the plunger and the speed of its motorized motion, as well as the requirements of generating cone jet or pulsation mode.
2. Increase the substrate motion speed. This is limited by the specifications of the motors which drive the substrate motion.

In our experimental apparatus, the theoretical minimum radius we can achieve is

$$R_m = 1.68\sqrt{\frac{2Q_m}{\pi v_M}} \approx 19.3\,\mu m \tag{4.22}$$

where $Q_m = 5\,nL$ is the minimum achievable external flow rate and $v_M = 24\,mm/s$ is the maximum achievable substrate motion speed.

We have successfully printed dot arrays of 10 μm radius, with Q_m and v_M listed above, which is shown in Fig. 4.9. The reasons why this radius is even smaller than the minimum radius estimated from the mode are attributed to the presence of the PS particles and contact line jumping.

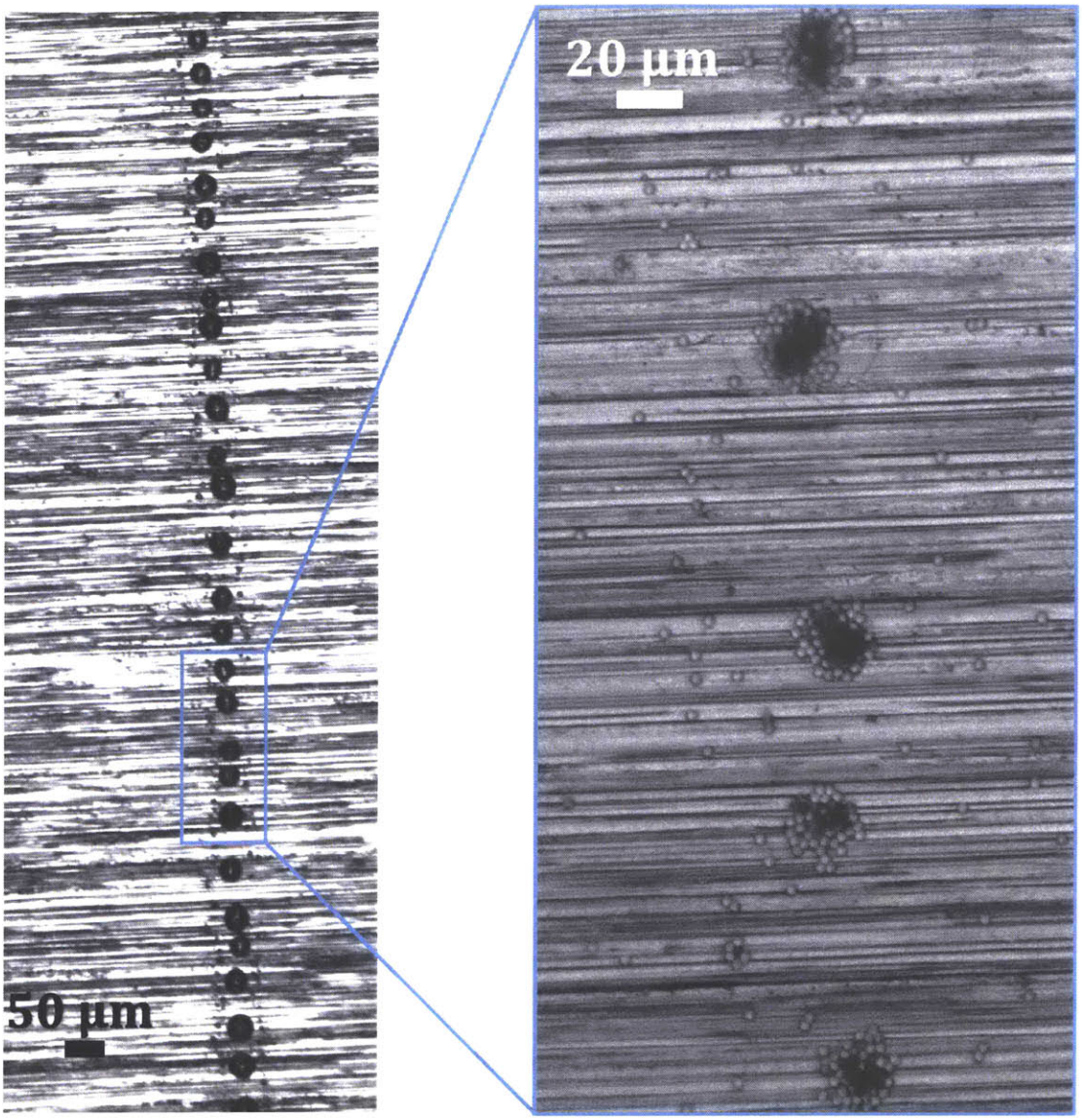

Fig. 4.9 Dot arrays printed with 3 μm PS microparticles of 10 μm feature radius.

Moreover, we have also printed 10 μm radius dot arrays from colloidal suspensions containing 3 μm diameter alumina microparticles. These colloidal suspensions are less monodispersed compared with the PS microparticles. Their nominal mean diameter is 3 μm while the diameter actually ranges from 1 μm to 5 μm under the inspection from the microscope. The dot arrays are shown in Fig. 4.10. The uniformity is worse than that of the dot arrays printed from PS microparticles mainly because the density of alumina ($3.95 g/cm^3$) is much larger than that of the solvent, hence the alumina microparticles will quickly settle down to the tip of the capillary and stack into layers of particles inside the meniscus. In this case the solid phase is separated from the liquid phase in the colloidal suspensions instead of being homogeneously dispersed, which affects the uniformity of the continuous EHD ejection process.

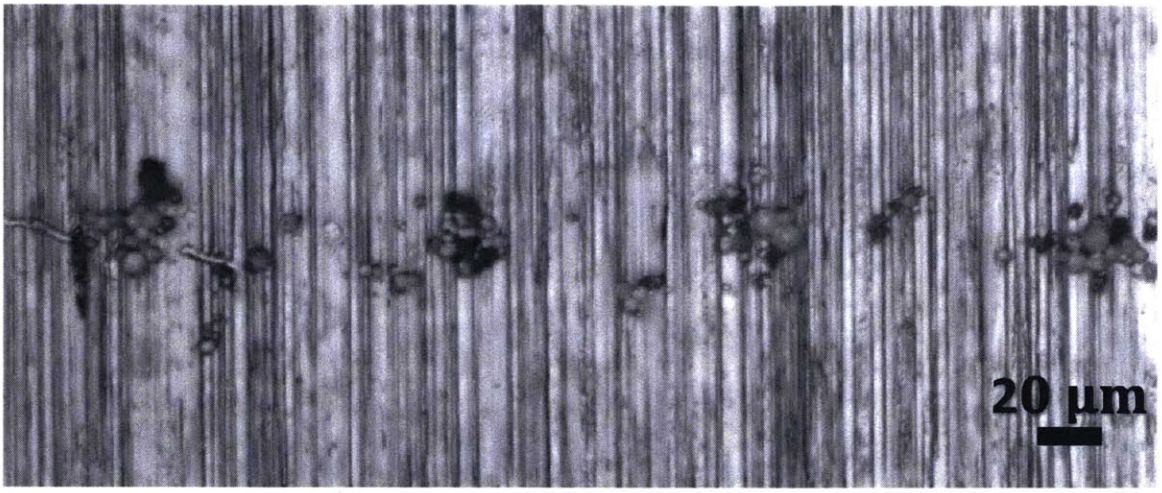

Fig. 4.10 Dot arrays printed with 3 μm alumina microparticles of 10 μm feature radius.

4.4. Printing Continuous Lines

We have also demonstrated the capability of our experimental apparatus to print continuous line patterns onto substrates with high wettability from colloidal suspensions using the mode-controlled continuous jetting mechanism.

As has been explained above, the initial lines printed onto substrates with high wettability will not break up because:

- Contact lines are more likely to be pinned hence suppress the break up process which requires the contact lines to move from two parallel lines into an array of separate circles.
- The time scale of the breakup process due to Plateau-Rayleigh instability is much larger on substrates with high wettability than that on substrates with low wettability. Hence if this time scale is much larger than the time for the solvent to evaporate, the pattern will remain as continuous lines as the initial lines will not break up before the solvent dries out. In our experiments of printing continuous line patterns, we did not add glycerin to the solvent in order to increase the evaporation rate of the solvent.

The colloidal suspensions are the same as above and the substrates are glass microscope slides. The contact angle between the colloidal suspensions and the substrates is measured to be $\theta = 16.2^{\circ}$ through imaging.

Fig. 4.11 shows the pattern of a continuous line composed of 3 µm diameter PS microparticles with a line width of $L_{PS} \approx 45\ \mu m$.

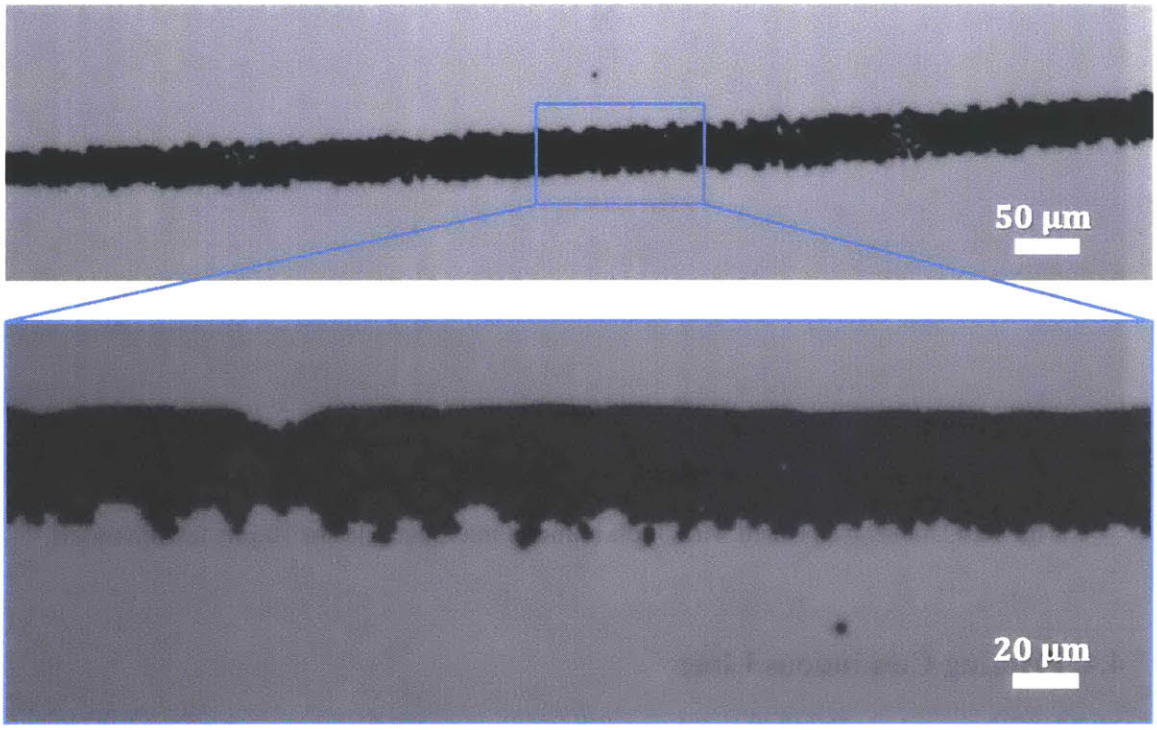

Fig. 4.11 A continuous line printed with 3 μm PS microparticles.

Fig. 4.12 shows the pattern of a continuous line composed of 3 µm diameter alumina microparticles with a line width of $L_{alumina} \approx 40\ \mu m$. Again, the uniformity of the line pattern printed from alumina microparticles is not as good as that from PS microparticles mainly because the sedimentation of the alumina microparticles affects the uniformity of the continuous EHD ejection process.

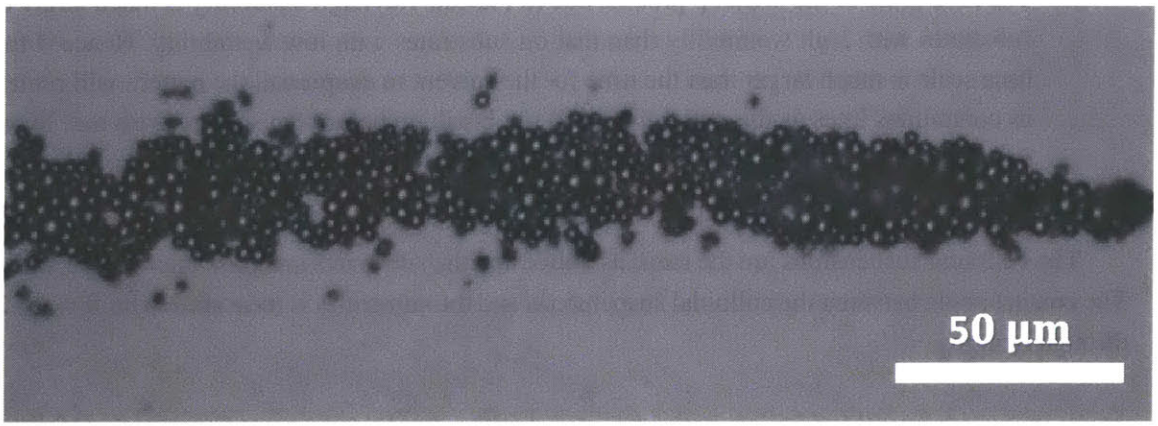

Fig. 4.12 A continuous line printed with 3 μm alumina microparticles.

Chapter 5: On-Demand EHD Printing of Particle Streams

In this chapter, we extends EHD-driven inkjet printing to a novel regime of on-demand direct depositing microparticulate materials, where the microparticles are ejected via EHD in the form of particle streams. The requirements, process control and three different ejection modes of this regime are discussed, and its capability of printing colloidal suspensions containing microparticles with different sizes and different materials is demonstrated. Moreover, the force balance of the microparticle at the apex of the Taylor cone upon ejection is analyzed to investigate the problem of particle aggregations during printing, and the constitutive laws of the typical printing modes are discussed. Furthermore, EHD printing of particle streams onto porous media is demonstrated and envisioned for future applications in AM.

5.1. On-Demand Printing

Unlike the mode-controlled continuous EHD jetting mechanism discussed in the previous chapter, in the on-demand printing mechanism, motorized plunger motion and the bias voltage pulses are applied in turns to induce flow (Fig. 3.10). An on-demand printing sequence is established by first incrementally moving the plunger to shape the meniscus at the tip of the capillary and then applying a bias voltage pulse between the capillary and the counter electrode to induce EHD ejection.

As has been explained in Chapter 2, in the on-demand printing scheme the flow rate is self-regulated and therefore a function of the amplitude of the bias voltage pulse. The expression of the function depends on the hydrodynamics of the capillary side of the system, more specifically in our experimental apparatus, on the free standing volume of the meniscus. Therefore as illustrated in Fig. 2.6, the dashed lines represent the family of the dispersion relations of the internal flow rate with respect to the electric filed, each dispersion curve is associated with one specific shape of the free standing meniscus. The bias voltage pulse finally determines the EHD ejection mode according to the corresponding dispersion curve.

Fig. 5.1 shows a sequence of snapshots from high speed recording of ejecting a 1/10 picoliter water droplet using the on-demand printing mechanism. Water is loaded into the needle and syringe in the same way as described in chapter 4. The baseline voltage is 1 kV, the amplitude and duration of the bias voltage pulse is 1 kV and 5 ms, respectively.

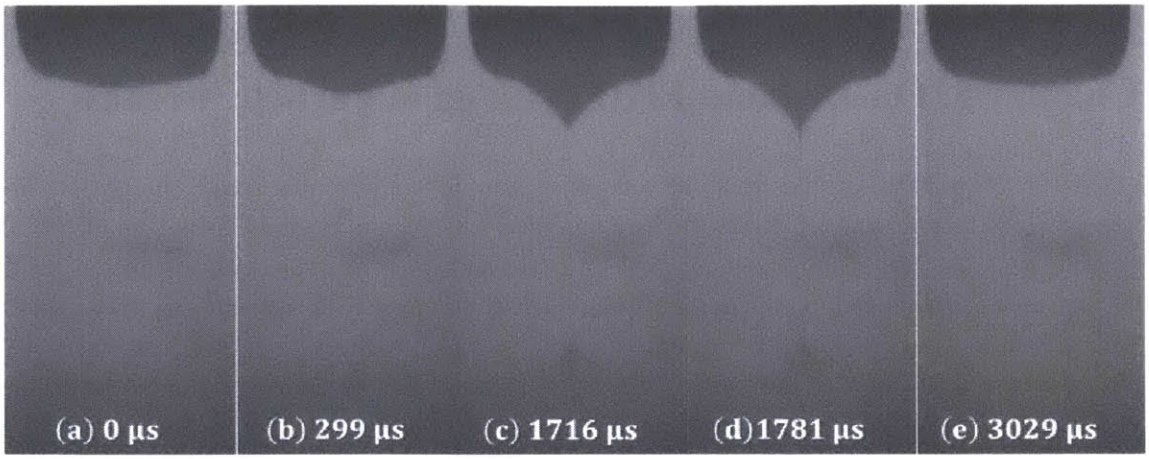

Fig. 5.1 A sequence of snapshots from high speed recording of printing a water droplet with 1/10 picoliter volume on demand: (a) Free standing meniscus before the bias voltage pulse is applied; (b) The meniscus starts to deform duo to the bias voltage pulse; (c) Taylor cone; (d) Taylor cone breaks at its apex and ejects a jet; (e) The pulse is released.

5.2. Introduction to EHD Printing of Particle Streams

In the EHD regime of printing microparticulate materials, the size of the microparticles are chosen to be range from 1 μm to 10 μm, which enables their sedimentation to the tip of the capillary and form stacks of particles near the meniscus. For simplicity, we refer the particle stacks as "slurry" throughout the following content of this chapter (Fig. 5.2).

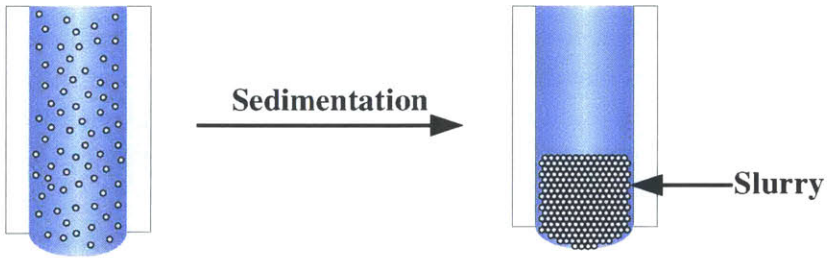

Fig. 5.2 Microparticles settle down to the tip of the capillary and form a "slurry" near the meniscus.

The critical size of the colloidal suspensions to form such a slurry ready for EHD printing depends mainly on the relative density of the microparticles versus that of the solvent. We have conducted experiments to print different colloidal suspensions with different sizes and materials and determined the minimal diameter[10] for the microparticles to form the slurries. Table 5.1

[10] The minimal diameters are determined by inspection from the high speed camera that the microparticles settle down to the tip of the capillary due to gravity and form slurries with a height of at least 1 mm rapidly, for practical use in our experiments, within 5 minutes.

summarizes the minimal diameters required for colloidal suspensions with different materials, with the solvent of a mixture of water and glycerin at a volume ratio of 10:1.

Material	Density [g/cm^3]	Minimal diameter to form slurries [μm]
PS	1.04	10
Melamine	1.57	5
Silica	2.65	3
Alumina	3.95	2

Table 5.1 Particle sizes of each material that were observed to form slurries at the tip of the needle.

Unlike conventional EHD-driven inkjet printing of homogeneously dispersed functional inks which behaves similar to pure liquids, in the regime of microparticles, the solid state is separated from the liquid state in the colloidal suspension, therefore the printing process behaves in a different way. Fig. 5.3 compares the ideal process of printing microparticles versus that of homogeneously dispersed functional inks, with the microparticles behaving in the following three subsequent steps:

1. Stacking into layers near the meniscus
   After the colloidal suspensions are loaded into the vertically aligned needle, microparticles are delivered to the tip of the needle to stack into layers near the meniscus, either via the gravitational sedimentation for large particles or other transport mechanisms for small particles.
2. Filling in the meniscus
   When a bias voltage pulse is applied, the microparticles inside the needle fill in the meniscus when it starts to deform into a conical shape. The meniscus functions as the envelope of the microparticles. The slurry is required to be "soft" as it needs to fill in the meniscus and does not disturb the shape during its deformation.
3. Being ejected in particle streams
   When the amplitude and duration of the bias voltage pulse are large enough to break the apex of the Taylor cone and exert sufficient force on the submerged microparticles near the apex, the particles will be ejected in the form of short and fine streams, which consists of small particle clusters sequentially. We name this as EHD printing of particle streams.

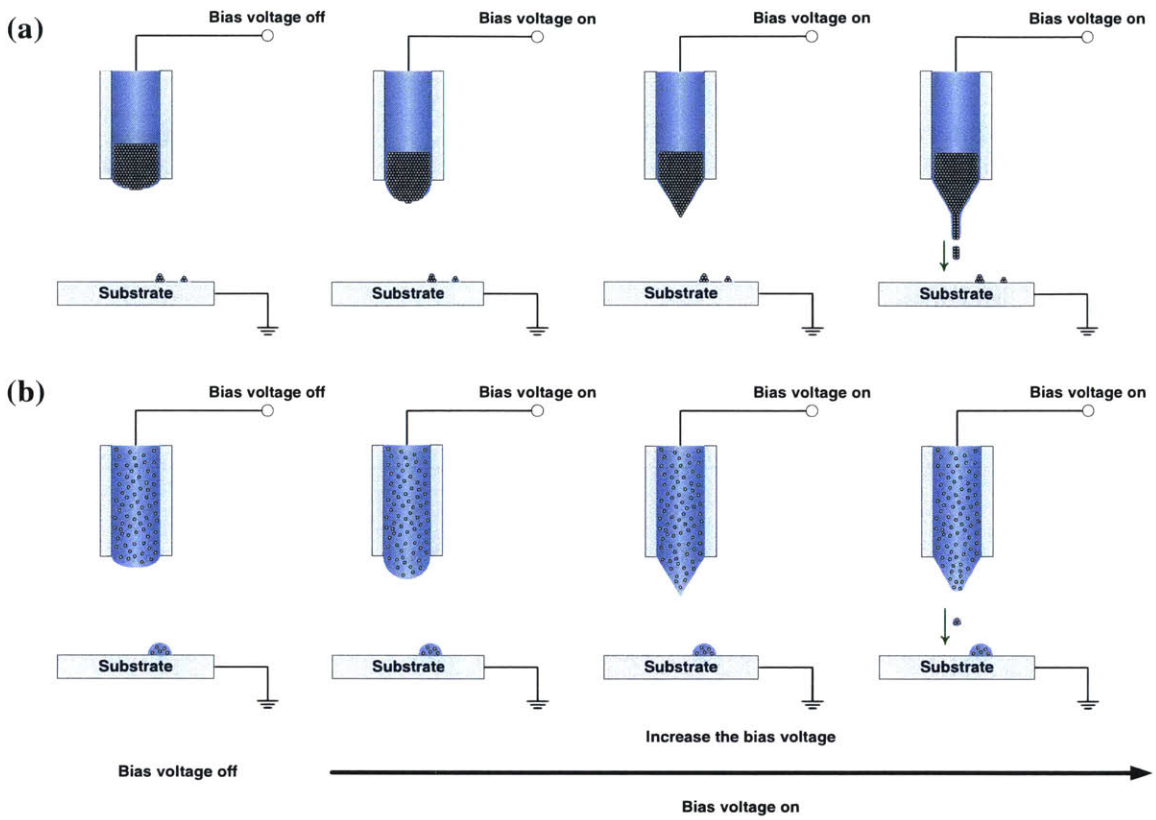

Fig. 5.3 Schematics of EHD printing of particle streams versus the conventional EHD driven inkjet printing of homogeneously dispersed functional inks.

5.3. Demonstrations of EHD Printing of Particle Streams

We have demonstrated the capability of on-demand EHD printing of particle streams of depositing colloidal suspensions containing microparticles with different sizes and materials. The sequences of snapshots of high speed recording of the printing processes and the corresponding printed patterns are shown in Fig. 5.4 – 5.8. The printing parameters are summarized in Table 5.2.

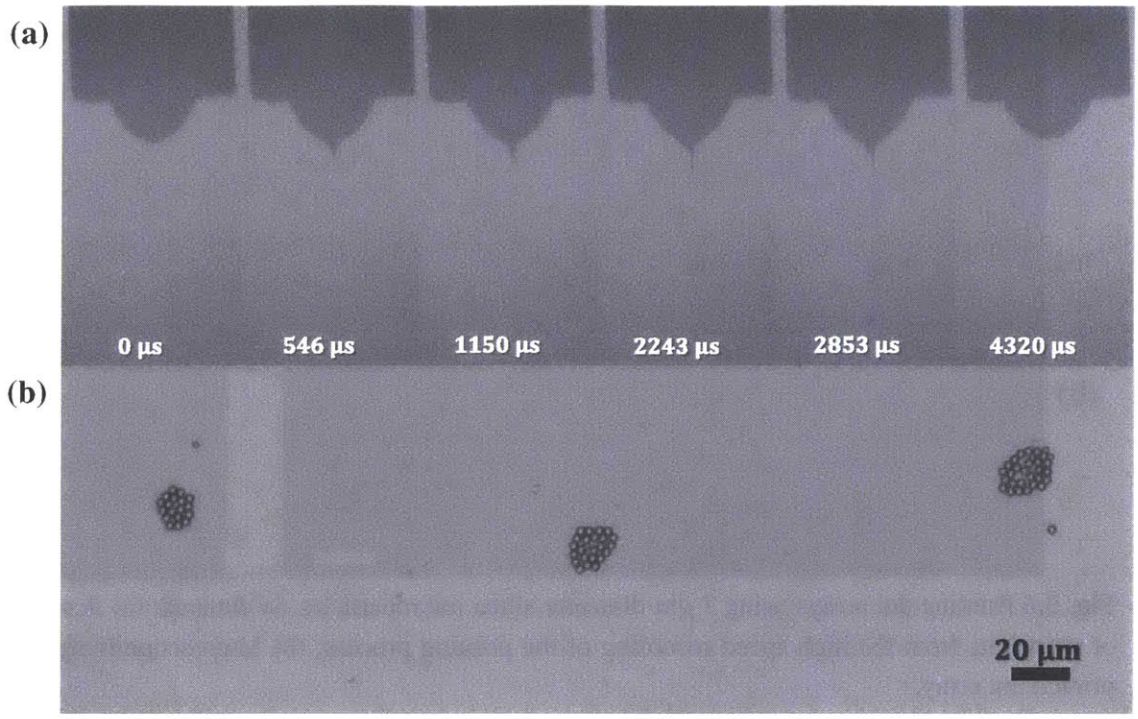

Fig. 5.4 Printing dot arrays using 3 μm diameter silica microparticles on demand: (a) A sequence of snapshots from the high speed recording of the printing process; (b) Microscope image of the printed dot array.

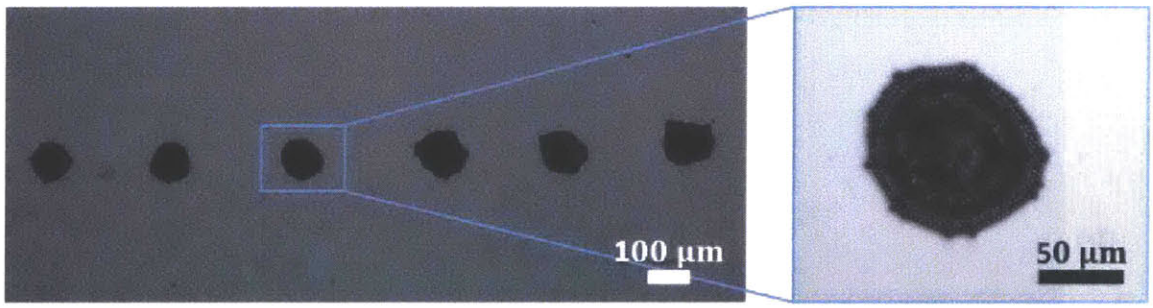

Fig. 5.5 A larger dot array printed from 3 μm diameter silica microparticles on demand.

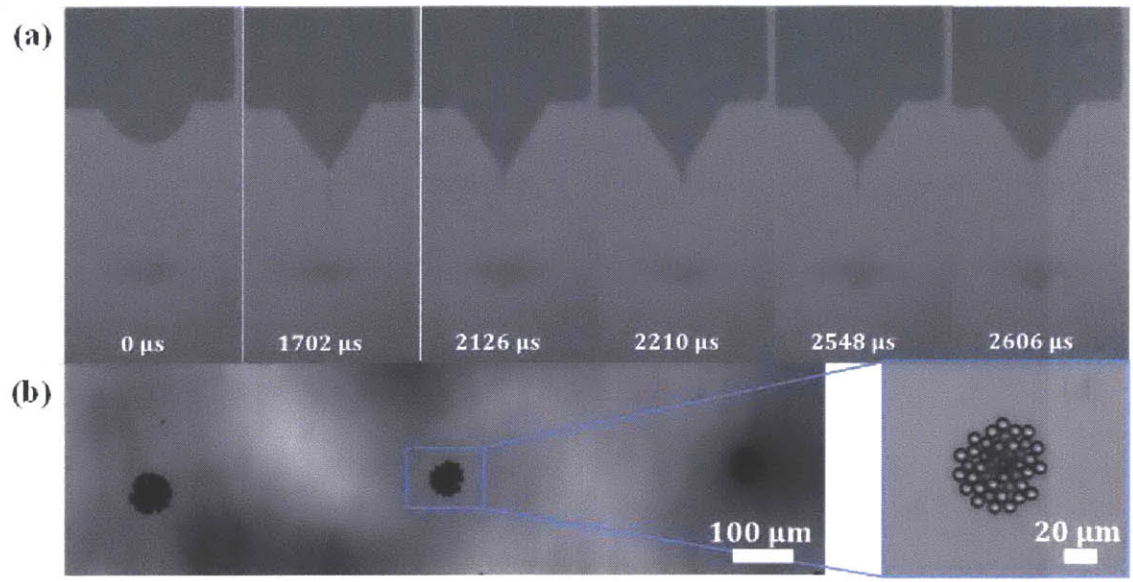

Fig. 5.6 Printing dot arrays using 7 μm diameter silica microparticles on demand: (a) A sequence of snapshots from the high speed recording of the printing process; (b) Microscope image of the printed dot array.

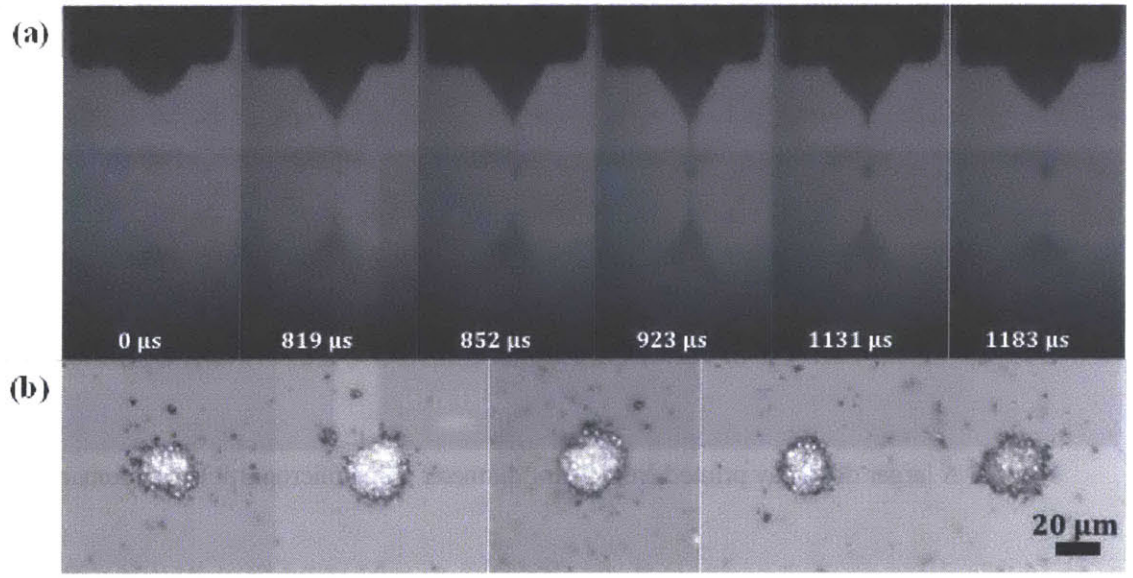

Fig. 5.7 Printing dot arrays using 3 μm diameter alumina microparticles on demand: (a) A sequence of snapshots from the high speed recording of the printing process; (b) Microscope image of the printed dot array.

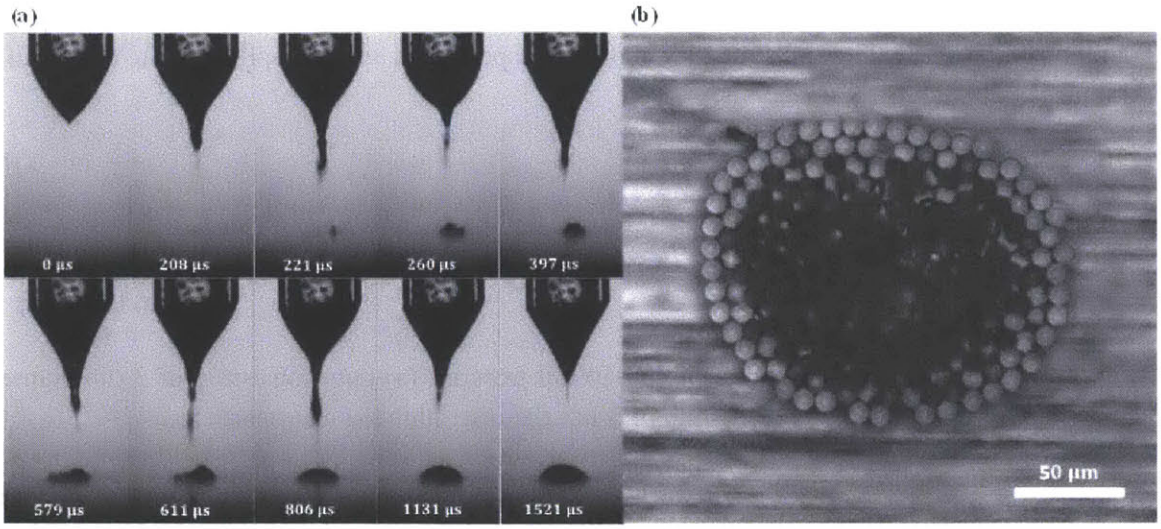

Fig. 5.8 Printing a dot using 10 μm diameter PS microparticles on demand: (a) A sequence of snapshots from the high speed recording of the printing process; (b) Microscope image of the printed dot.

	Fig. 5.4	**Fig. 5.5**	**Fig. 5.6**	**Fig. 5.7**	**Fig. 5.8**
Material	Silica	Silica	Silica	Alumina	PS
Size [µm]	3	3	7	3	10
Baseline voltage [kV]	1	1	1	1	1
Pulse amplitude [kV]	1.5	2.5	1.5	1.5	1.5
Pulse duration [ms]	5	5	5	5	5
Separation between the capillary tip and the substrate [µm]	~300	~300	~300	~200	~400
Pattern diameter [µm]	~15	~100	~60	~25	~120
Pattern spacing [µm]	~100	~300	~500	~1000	-

Table 5.2 Printing parameters and pattern sizes.

The separation from the tip of the capillary to the substrate is usually chosen to be between 200 µm and 400 µm. On the one hand the separation needs to be large enough to prevent the substrate from contacting with the Taylor cone, on the other hand it should not be too large in order to eliminate the instability when the particle streams are too long. The specific value is determined during each print, which mainly depends on the shape of the Taylor cone

Moreover, we have successfully printed patterns with sub-10 µm features using 3 µm diameter silica microparticles and 3 µm diameter alumina microparticles respectively, which are shown in

Fig. 5.9. The printing conditions are the same with a baseline voltage at 1 kV, the amplitude and duration of the bias voltage pulse at 1 kV and 3 ms respectively, and the capillary tip to the substrate distance at 200 μm.

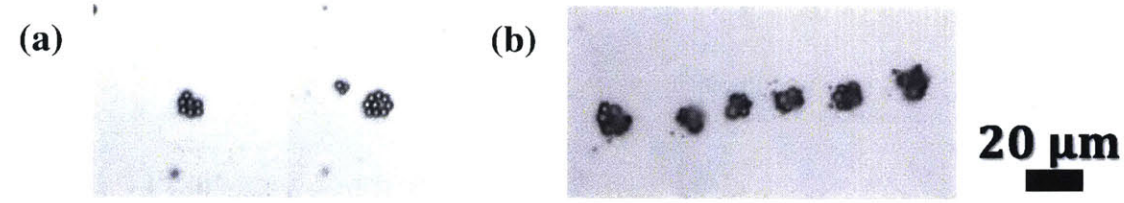

Fig. 5.9 On-demand EHD printing of sub-10 μm features: (a) dots consisting of 3 μm diameter silica microparticles; (b) dots consisting of 3 μm diameter alumina microparticles.

5.4. Printing Modes

We have observed three distinct ejection modes within the regime of printing microparticles (summarized in Table 5.3). The schematic and sequences of snapshots from high speed recording of the three printing modes are shown in Fig. 5.10 respectively.

Printing mode	**Description of the printing mode**	**Particle concentration**
Particle stream	Taylor cone is formed at the tip of the capillary before ejection happens and small particle clusters are ejected in the form of streams afterwards.	High
Chunk of particles	Taylor cone is not formed before printing and a large (with size usually comparable to the dimension of the capillary) chunk of particles pinches off from the nozzle.	High
Particles in droplets	Slurries are not well formed. Taylor cone is formed before ejection and small droplets containing several microparticles are ejected.	Low

Table 5.3 Definition and description of the ejection modes of printing microparticles.

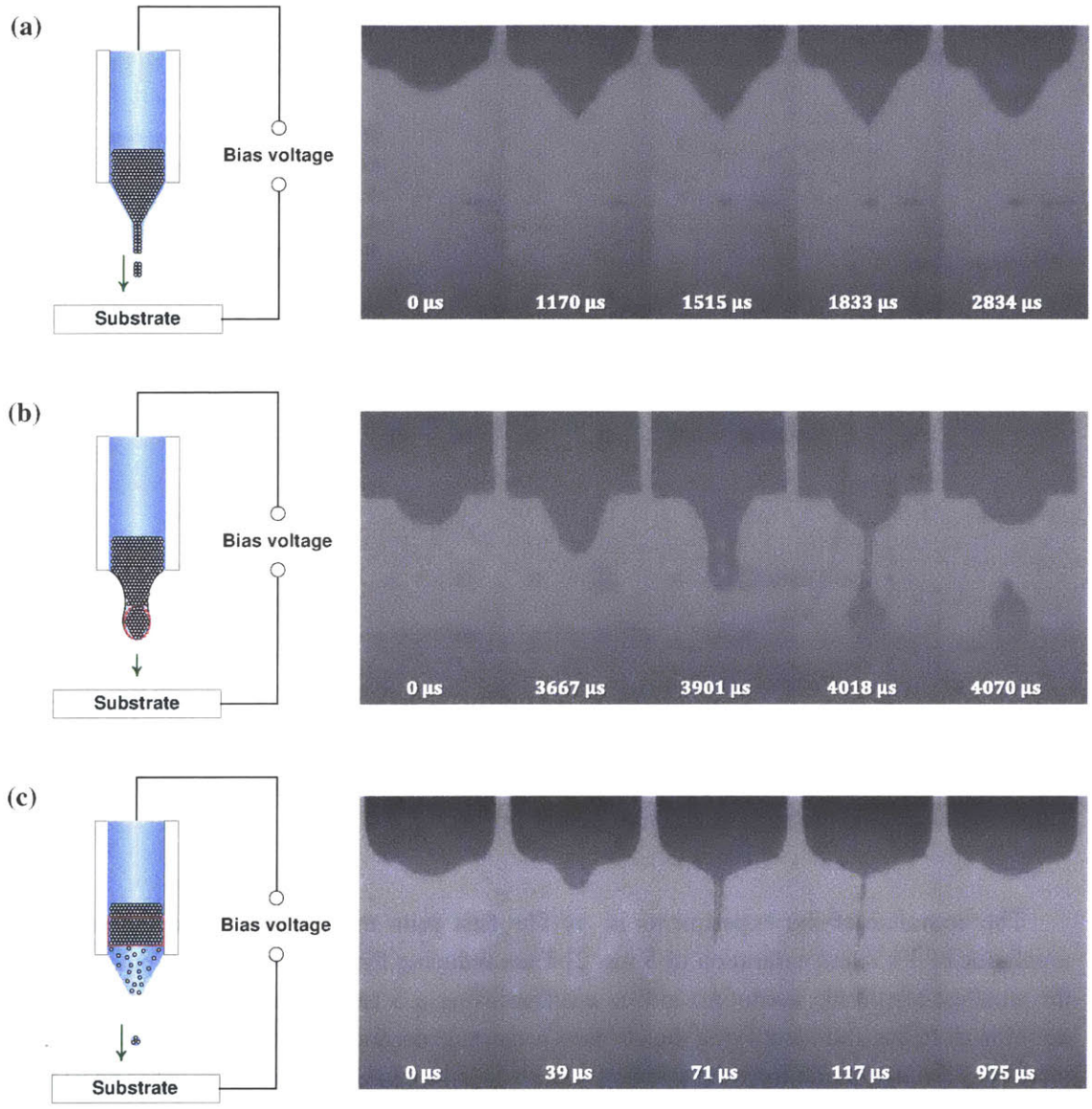

Fig. 5.10 Schematics and sequences of snapshots of high speed recording of the three different printing regimes of microparticles (red dashed lines indicate large particle clusters): (a) particle streams; (b) chunk of particles; (c) particles in droplets.

In order to understand the underlying mechanisms and the requirements to generate each printing mode, a series of identical experiments was conducted where the amplitude and the duration of the bias voltage pulses are varied. The colloidal suspensions are those contain silica microparticles with 3 µm diameter. The solvent is a mixture of water and glycerin at a volume ratio of 10:1. The baseline voltage is fixed at 1 kV, and the separation between the capillary tip and the substrate at 250 µm and the free standing meniscus at a semispherical shape. Moreover, between each print, we waited for >5 minutes to guarantee that the colloidal suspensions in the needle had reached an equilibrium steady state after the disturbance from the previous print.

Fig. 5.11 shows the phase diagram of the ejection modes of printing microparticles, with respect to the amplitude and duration of the bias voltage pulses.

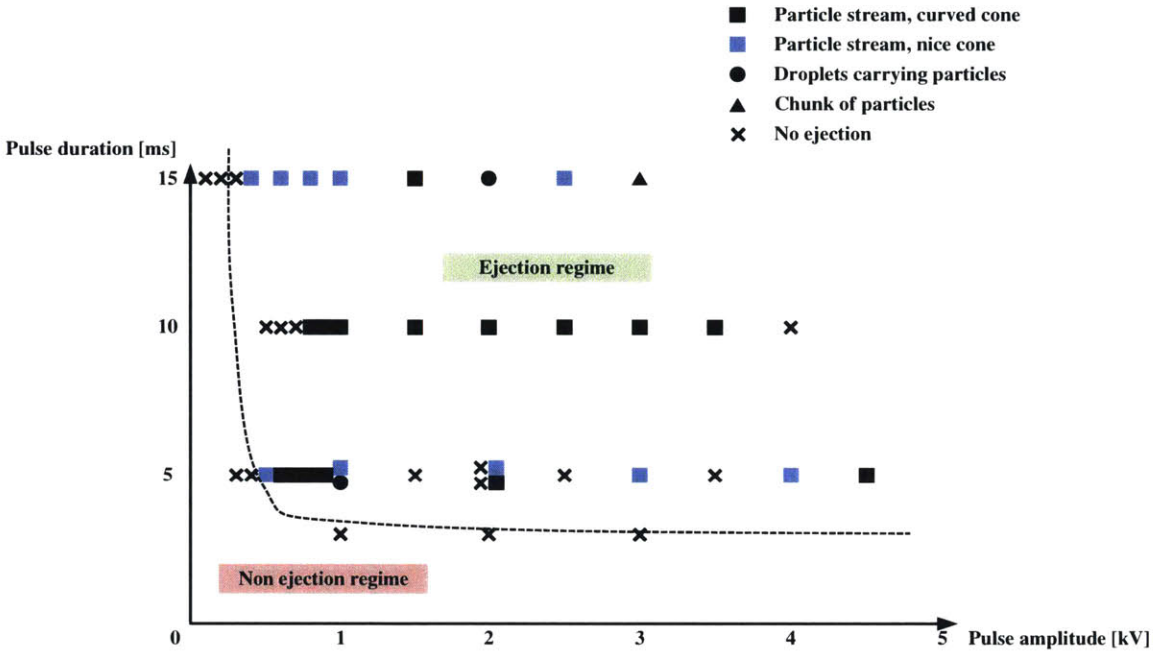

Fig. 5.11 Phase diagram of the ejection modes of 3 μm diameter silica microparticles with respect to the amplitude and duration of the bias voltage pulses.

The sequence of the experiments is: 1) The first print using a bias voltage pulse with an amplitude of 1 kV and a duration of 5 ms. 2) Then reducing the amplitude of the pulse to identify the smallest amplitude needed to induce ejection using a 5 ms duration. 3) Next increasing the duration to 15 ms and identifying the smallest amplitude needed to induce ejection. 4) Afterwards increasing the amplitude from the smallest value which has just been identified in the previous step to 5 kV. At each value of the amplitude, recording the printing modes at the duration of 15 ms, 10 ms and 5 ms respectively and identifying the smallest duration needed to induce ejection. The threshold values of the amplitude and duration of the bias voltage pulses mentioned above in our experiments are chosen based on our experience from the large amount of experiments we have conducted.

The dashed line in the phase diagram distinguishes the explicit non-ejection regime from the ejection regime. This is straightforward as the amplitude of the bias voltage needs to be large enough to deform the meniscus and break the apex of the Taylor cone to induce ejection, while the duration needs to be large enough for the meniscus to deform from a hemisphere to a cone. The minimal duration is inversely proportional to the amplitude.

However, from the phase diagram we notice that: 1) the non-ejection cases exist in the explicit ejection regime; 2) for pulse voltage pulses with the same amplitude and duration, different printing behaviors exist. Looking into the high speed recordings of the corresponding printing events, we find that the conditions of the ideal soft slurry described above are seldom the case. Instead, it has

been commonly observed that microparticles aggregate and form rigid particle clusters inside the meniscus and does not fill in the conical shape of the meniscus.

Therefore the printing performances (resolution, positioning accuracy and repeatability) is highly degraded by the aggregations of the microparticles inside the needle in the following aspects:

- **The consistency of printing is poor:**
  From our experimental observations, the morphology of how the microparticles pack inside the meniscus affects the dynamics of the particle stacks and hence the ejection behaviors, including: 1) whether or not ejection happens (Fig. 5.12 shows a sequence of snapshots of the high speed recording of the printing experiment with a 4 kV/10 ms pulse referred in the phase diagram Fig. 5.11, where the ejection is held back by aggregation); 2) the amount of solids being ejected. Hence, different printing events can happen though the free standing meniscuses and the profile of the bias voltage pulses are the same (e.g., the (2 kV, 5 ms) point in Fig. 5.11). Moreover, the aggregation process is hard to control and rationalizing the morphology of the aggregations is not practical for now, which makes the consistency of the printing process even more stochastic.

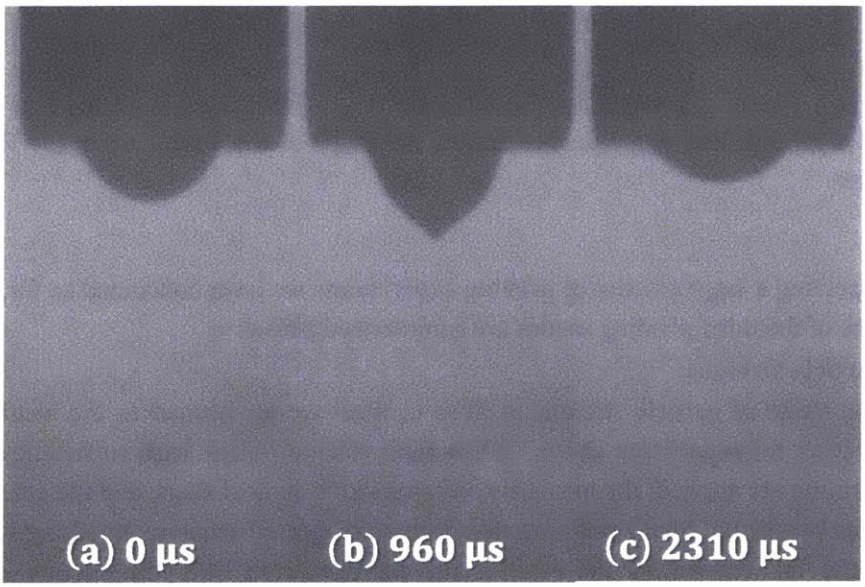

Fig. 5.12 A sequence of snapshots from high speed recording of a printing event where the ejection is held back by aggregations: (a) Free standing meniscus before apply the bias voltage pulse; (b) Taylor cone has formed and remained until the end of the pulse while no ejection happens; (c) The bias voltage pulse is released.

- **The trajectory of the ejected particle clusters deviates from the axis of the capillary:**
  When aggregation happens, the microparticle clusters are usually too rigid to fill into the meniscus. The shape of the meniscus is disturbed by the presence of the rigid aggregations and does not remain a vertically aligned cone anymore. This makes the direction of the particle streams deviate from the axis of the capillary, therefore affects the positioning accuracy of the printing. Fig. 5.13 shows a snapshot from the high speed recording of a

printing event where the Taylor cone is tilted due to the existence of the aggregations inside the meniscus and the direction of the particle stream deviates from the vertical direction with a large angel up to 30°.

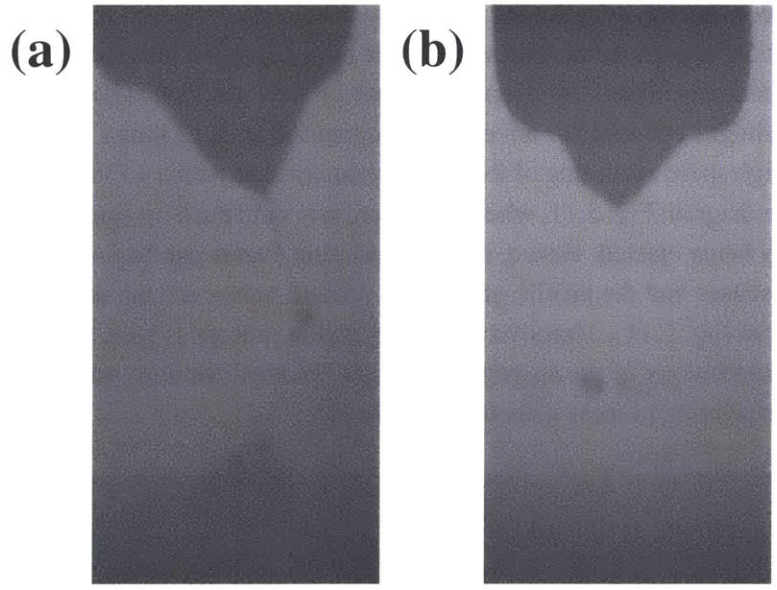

Fig. 5.13 Large and rigid aggregations disturb the shape of the Taylor cone: (a) Tilted cone; (b) Curved cone.

By inspecting a large amount of printing experiments we have conducted so far, the formation mechanisms of the three printing modes are summarized below:

- **Particle streams:**
  The mode of particle streams is close to what we envisioned as the ideal conditions of printing microparticles above. When bias voltage pulses with sufficient amplitude and duration are applied, the meniscus deforms into a conical shape and the apex of the Taylor cone breaks up. Small wet particle clusters are ejected sequentially along with streams of liquid in between by the electrostatic force exerted from the counter electrode. The amplitude and duration of the bias voltage pulses are usually larger than those needed to print pure solvent, as the presence of the microparticles increases the effective viscosity of the functional inks. In this mode, microparticles either do not form large particle clusters or the interparticle adhesion in the clusters are not strong to resist the electrostatic force. Fig. 5.14 shows a sequence of snapshots from high speed recoding of a printing event where the large particle cluster is elongated and broken up at its tip by the electrostatic forces and particle streams are ejected.

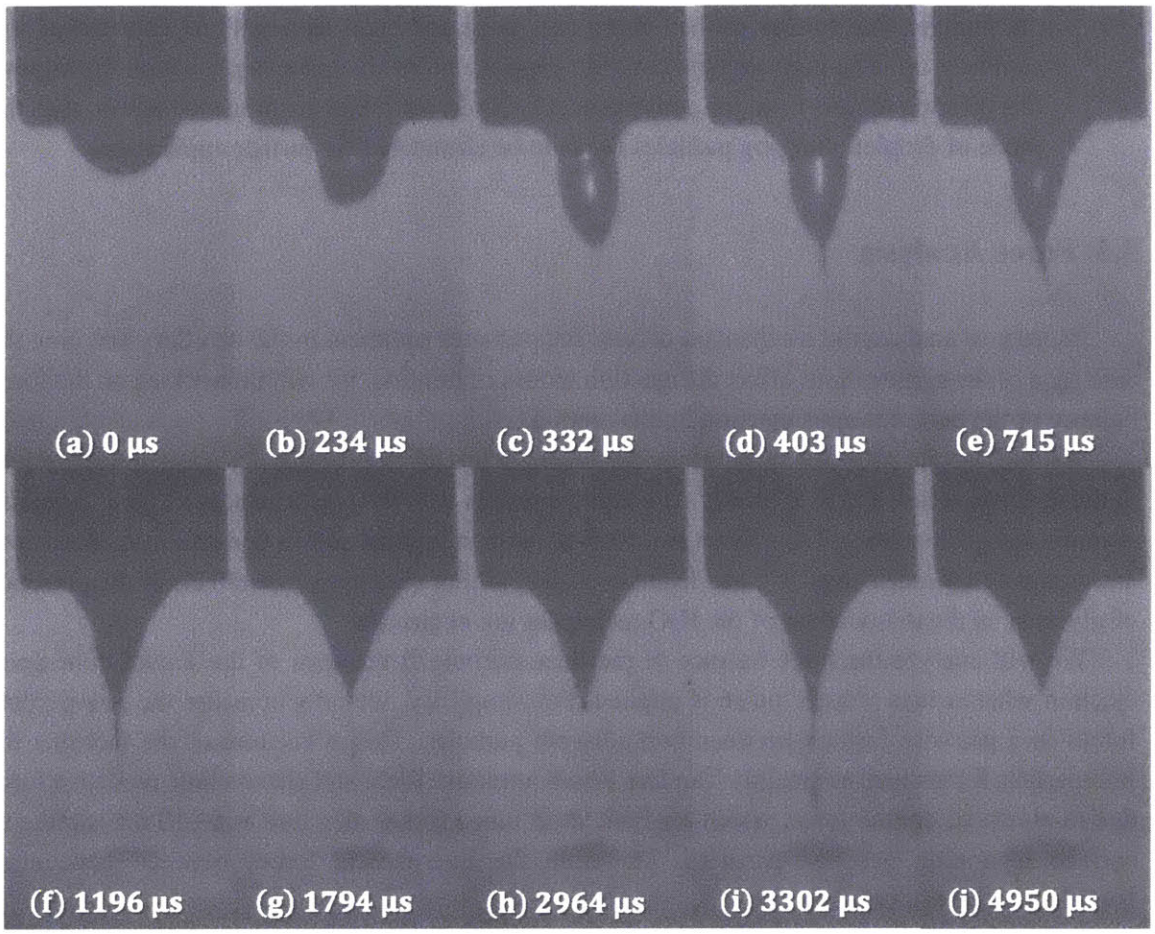

Fig. 5.14 A sequence of snapshots of high speed recording of a printing event where the aggregations has formed, but the interparticle bondings within are not strong enough to resist the electrostatic forces, therefore the aggregation is teared to eject particle stream.

- **Chunk of particles:**
  Microparticles aggregate to form large and rigid particle clusters inside the meniscus, and the interparticle adhesion is too strong for the electrostatic force to break up the clusters. Therefore ejection happens at the interfaces between adjacent large particle clusters where the interparticle adhesion are the weakest, and chunks of particles are ejected in single pieces instead of particle streams.
- **Particles in droplets:**
  In the printing regime of microparticulate materials, particles settle down to the tip of the capillary and make the local particle concentration much higher than its original concentration (can be as high as 74% in volume fraction for random close pack). The only reason for the low particle concentration near the meniscus in the mode of particles in droplets is that, particles sediment into large and rigid clusters above the tip of the capillary and prevent other microparticles from reaching the capillary tip. This hypothesis has been verified from the experimental observation that after printing droplets carrying particles,

the plunger was further pushed down and large and rigid aggregations approached the capillary tip. The high particle concentration is one of the advantages which distinguish this printing regime from the conventional EHD driven inkjet printing techniques, thus the mode of droplets carrying particles needs to be eliminated for further applications.

5.5. Force Analysis

In order to analyze the mechanism of how the particles sediment in the capillary and how the existence of the aggregations affect the ejection modes of printing, we will be working on the force balance of the particles upon ejection in this section.

We will use the colloidal suspensions containing 3 μm silica microparticles as a model system in the analysis below and then briefly compare the results with the performances of other colloidal suspensions qualitatively. The solvent has 10% glycerin in volume and its density, surface tension, and viscosity are calculated [88,89] and listed in Table 5.4. For simplicity, the effects of the presence of glycerin on the dissociation of the H_2O molecules are neglected.

We will analyze the force balance of the microparticle at the apex of the Taylor cone upon ejection when a bias voltage pulse is applied. For simplicity, we only consider the interparticle forces in a pairwise fashion between two adjacent particles. This is because of the fact that the interparticle forces here are mainly Van Der Waals attractive force and electrostatic repulsive force due to electrical double layer, which are both short range forces effective at a ~10 nm surface to surface separation between particles. Therefore the interparticle forces between noncontact particles can be neglected.

The forces exerted on this microparticle are listed as follows: (Fig. 5.15)

- Electrostatic force exerted by the counter electrode F_Φ
- Surface tension force due to capillary bridge with the adjacent microparticles: F_γ
- Electrostatic repulsive force due to electrical double layer F_{DL}
- Van der Waals attractive forces: F_{VDW}
- Gravitational force from the microparticles stacking above F_g
- Viscous drag F_μ
- Inertial drag F_ρ
- Self-weight of the microparticle W[11]

[11] The buoyant force has been considered in calculation by subtracting the density of the solvent.

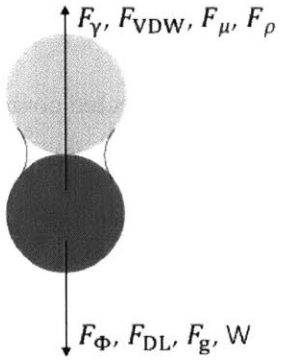

Fig. 5.15 Forces exerted on the microparticle at the apex of the Taylor cone upon ejection.

Characteristic dimensions and parameters are listed in the Table 5.4 below:

Parameters	**Value**	**Note**
Characteristic speed of particle ejection	$v = 2$ m/s	Obtained from the high speed videos
Characteristic length scale	$r = 1.5$ μm	Radius of the particle
Characteristic amplitude of the bias voltage	$\Phi = 5$ kV	
Characteristic separation between the capillary tip and the substrate	$s = 250$ μm	
Dynamic viscosity of the solvent	$\eta = 1.34 \times 10^{-3} Pa \cdot s$	
Surface tension of the solvent	$\gamma = 71$ mN/m	
Density of the solvent	$\rho = 1022$ kg/m^3	
Density of the particle	$\rho_p = 2650$ kg/m^3	

Table 5.4 Characteristic dimensions and parameters during printing of microparticles.

Order of magnitude analysis of F_μ, F_ρ and W versus F_γ:

The capillary length is

$$\lambda_c = \sqrt{\frac{\gamma}{\rho g}} = \sqrt{\frac{71\times10^{-3}}{1022\times10}} \approx 2.64mm \gg r = 1.5\,\mu m \tag{5.1}$$

Therefore the gravity of the solvent can be neglected compared to surface tension.

The capillary number is

$$Ca = \frac{\mu v}{\gamma} = \frac{1.34\times10^{-3}\times2}{71\times10^{-3}} \approx 0.038 \ll 1 \tag{5.2}$$

Therefore viscous drag can be neglected compared to surface tension.

The Weber number is

$$We = \frac{\rho v^2 r}{\gamma} = \frac{1022\times2^2\times1.5\times10^{-6}}{71\times10^{-3}} \approx 0.086 \ll 1 \tag{5.3}$$

Therefore inertial drag can be neglected compared to surface tension.

The self-weight of the microparticle versus surface tension force:

$$\frac{W}{F_\gamma} = \frac{\frac{4}{3}\pi r^3(\rho_p-\rho)g}{2\pi r\gamma} = \frac{\frac{4}{3}\pi\times(1.5\times10^{-6})^3\times(2650-1022)\times10}{2\pi\times1.5\times10^{-6}\times71\times10^{-3}} = 3.44\times10^{-7} \ll 1 \tag{5.4}$$

Therefore the self-weight of the microparticle can be neglected compared to surface tension force.

5.5.1. Interaction Free Energy

5.5.1.1. Electrical Double Layer Force

In this section, we will estimate the electrostatic repulsive force which is resulted from the electric double layer on the interface of the silica microparticles and water.

Silica surfaces acquire a charge when in contact with water due to the dissociation of silanol groups

$$\mathrm{SiOH} \rightleftharpoons \mathrm{SiO^-} + H^+ \tag{5.5}$$

In order to estimate the surface charge density of the silica microparticles and the interaction free energy, firstly the Debye length of the colloidal suspensions in our experiments is calculated in order to choose the appropriate model. The solvent we used in our experiments are water from the DI water tap in our lab. We will calculate its Debye length.

The Debye length in colloidal suspensions with a symmetric monovalent electrolyte (e.g., water) is given by

$$\kappa^{-1} = \frac{1}{\sqrt{8\pi\lambda_B N_A I}} \tag{5.6}$$

where λ_B is the Bjerrum length of the medium, for water at room temperature (25 °C), $\lambda_B \approx 0.7\ nm$, N_A is the Avogadro number, and I is the ionic strength of the colloidal suspensions with a unit of mol/m^3.

Therefore

$$\kappa^{-1} = \frac{0.304}{\sqrt{I(M)}}\ (\text{nm}) \tag{5.7}$$

where $I(M)$ is the ion strength with a unit of mol/L

We measured[12] the PH value of the DI water to be 6. Thus

$$I(M) = 10^{-PH} = 10^{-6}\ mol/L \tag{5.8}$$

Therefore the Debye length of the solvent is

$$\kappa^{-1} = \frac{0.304}{\sqrt{I(M)}} = \frac{0.304}{\sqrt{10^{-6}}} = 304\ \text{nm} \tag{5.9}$$

While the diameter of the silica microparticles in the colloidal suspensions is d = 3 μm, which is substantially larger than the Debye length of the solvent $\kappa^{-1} = 304$ nm. Hence DLVO theory is applied in this study to estimate the interaction free energy (U) between two spherical microparticles under the Debye-Huckel approximation, which is given by

$$U_{DL} = \frac{Q^2}{4\pi\varepsilon\varepsilon_0}\left(\frac{e^{\kappa r}}{1+\kappa r}\right)^2 \frac{e^{-\kappa L}}{L} \tag{5.10}$$

where Q is the effective surface charge on each silica microparticle, $\varepsilon_0 = 8.85 \times 10^{-12}\ F/m$ is the absolute permittivity in vacuum, ε is the relative permittivity of water, $\varepsilon \approx 80$ at room temperature, r is the radius of the silica microparticles, and L is the center to center distance between the silica microparticles

Assume that the effective surface charge is uniformly distributed on the surface of the silica microparticles, hence

$$Q = 4\pi r^2 \sigma \tag{5.11}$$

where σ is the effective surface charge density of the silica microparticles, which can be estimated via [98]

$$\sigma = \varepsilon\varepsilon_0\kappa\Psi\left(1 + \frac{1}{\kappa r}\right) \tag{5.12}$$

where Ψ is the surface potential of the silica water interface.

Insert equation (5.11) and (5.12) into equation (5.10), the interaction free energy between the two microparticles due to double layer can be given by

[12] The measurement was done using a HMDPHM80 digital pH/temperature meter in our lab.

$$U_{DL} = 4\pi\varepsilon\varepsilon_0 r^2\Psi^2 \frac{e^{-\kappa h}}{2r+h} \tag{5.13}$$

where h is the surface to surface distance between the two microparticles. As the double layer force is a short range force which is usually effective on the length scale of ~10 nm and can be neglected when the particles are separated with a distance more than 100 nm. Hence in this study h~10 nm, while the size of the microparticles are usually on the order of microns, i.e., $2r \gg h$, thus $2r + h \approx 2r$. Therefore we can further simplify equation (5.13) to

$$U_{DL} = 2\pi\varepsilon\varepsilon_0 r\Psi^2 e^{-\kappa h} \tag{5.14}$$

Hence the double layer forces can be derived by

$$F_{DL} = -\frac{dU_{DL}}{dh} = 2\pi\varepsilon\varepsilon_0 r\kappa\Psi^2 e^{-\kappa h} \tag{5.15}$$

For our model system: r = 1.5 μm. According to previous work [98-100], the surface potential of the silica microparticles Ψ usually ranges −10~50 mV. To a sufficient approximation, we estimate that $\Psi = -20$ mV for the following calculation. Insert the values into equation (5.14) and (5.15) we can get

$$U_{DL}(h) = 2\pi\varepsilon\varepsilon_0 r\Psi^2 e^{-\kappa h} = 2.67 \times 10^{-18}\exp(-3.29 \times 10^{-3}h) \tag{5.16}$$

$$F_{DL}(h) = 2\pi\varepsilon\varepsilon_0 r\kappa\Psi^2 e^{-\kappa h} = 8.78 \times 10^{-12}\exp(-3.29 \times 10^{-3}h) \tag{5.17}$$

where h has a unit of nm.

5.5.1.2. Van der Walls Force

The non-retarded Van der Waals interaction free energy between two silica microparticles with the same radius is given by

$$U_{VDW} = \frac{-Ar}{12h} \tag{5.18}$$

under the condition that h ≪ r, and A is the Hamaker constant.

Hence the Van der Waals force is given by

$$F_{VDW} = -\frac{dU_{VDW}}{dh} = -\frac{\mathrm{Ar}}{12}\frac{1}{h^2} \tag{5.19}$$

For our model system, r = 1.5 μm. And for silica microparticles dispersed water, it has been measured that $A \approx 0.46 \times 10^{-20} J$. [101,102] Insert the values into equation (5.18) and (5.19) we can get

$$U_{VDW} = \frac{-Ar}{12h} = -5.75 \times 10^{-19}\frac{1}{h} \tag{5.20}$$

$$F_{VDW} == -\frac{\mathrm{Ar}}{12}\frac{1}{h^2} = -5.75 \times 10^{-10}\frac{1}{h^2} \tag{5.21}$$

where h has a unit of nm. The negative sign in equation (4.43) indicates that the Van der Waals force is attractive.

Hence, based on the DLVO theory [103-105], the total interaction free energy in the colloidal suspensions between two microparticles, including the contributions from the double layer force and the Van der Waals force is given by

$$U_1 = U_{DL} + U_{VDW} = 2\pi\varepsilon\varepsilon_0 r\Psi^2 e^{-\kappa h} - \frac{Ar}{12h} \tag{5.22}$$

And the net force is

$$F_1 = F_{DL} + F_{VDW} = 2\pi\varepsilon\varepsilon_0 r\kappa\Psi^2 e^{-\kappa h} - \frac{\mathrm{Ar}}{12h^2} \tag{5.23}$$

For our model system:

$$U_1 = U_{DL} + U_{VDW} = 2.67 \times 10^{-18}\exp(-3.29 \times 10^{-3}h) - 5.75 \times 10^{-19}\frac{1}{h} \tag{5.24}$$

$$F_1 = F_{DL} + F_{VDW} = 8.78 \times 10^{-12}\exp(-3.29 \times 10^{-3}h) - 5.75 \times 10^{-10}\frac{1}{h^2} \tag{5.25}$$

Fig.5.16 shows the plot of the total interaction free energy between the two silica microparticles with respect to their surface to surface distance. It is clear from the plot that the electrostatic self-repelling between the two particles dominates over the Van der Waals force, therefore the energy barrier is hard to overcome. Moreover, the thermal energy scales with

$$U_t \sim K_B T \approx 1.381 \times 10^{-23} \times 298.15 \approx 4.14 \times 10^{-21} J \tag{5.26}$$

where $K_B = 1.381 \times 10^{-23}\, m^2 \cdot kg \cdot s^{-2} \cdot K^{-1}$ is the Boltzmann constant and T = 298.15 K is the room temperature. The thermal energy is much smaller than the energy barrier of $2.5 \times 10^{-18} J$ indicated in Fig 5.16, hence the silica microparticles will not come close to stick together and cause aggregation.

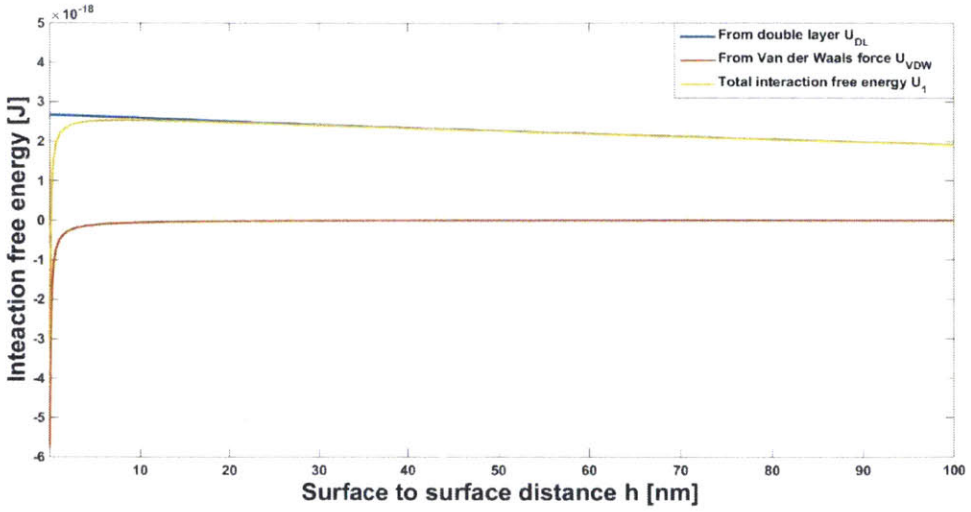

Fig. 5.16 Interaction free energy between two 3 μm diameter silica microparticles in water, with respect to their surface to surface distance.

5.5.1.3. Effects of Particle Stacking

However, in our experiments when colloidal suspensions are loaded into the needle, aggregations happen most frequently near the needle. This is due to the fact that when the microparticles settle down to the tip of the capillary and stack inside the meniscus, the particles at the bottom feel the compression from the weights of the particles above. Hence, the gravitational potential energy of the particles above provides additional energy to overcome the energy barrier, therefore causes aggregations to happen near the meniscus.

Denote H as the height of particle stacking inside the needle, d is the diameter of the microparticles. Hence the compression force that the microparticle at the bottom feels from the weights of the particles above is

$$F_g = \frac{H}{d}\frac{4}{3}\pi r^3(\rho_p - \rho)\mathrm{g} \tag{5.27}$$

Assume the above microparticles stack densely in a column, ρ_p is the density of the particles.

Hence the additional gravitational potential energy provided by the particles above is

$$U_g = F_g h \tag{5.28}$$

where the origin of the gravitational potential energy is chosen to be when the particle at the bottom is in contact with the particle right above it. (Fig. 5.17)

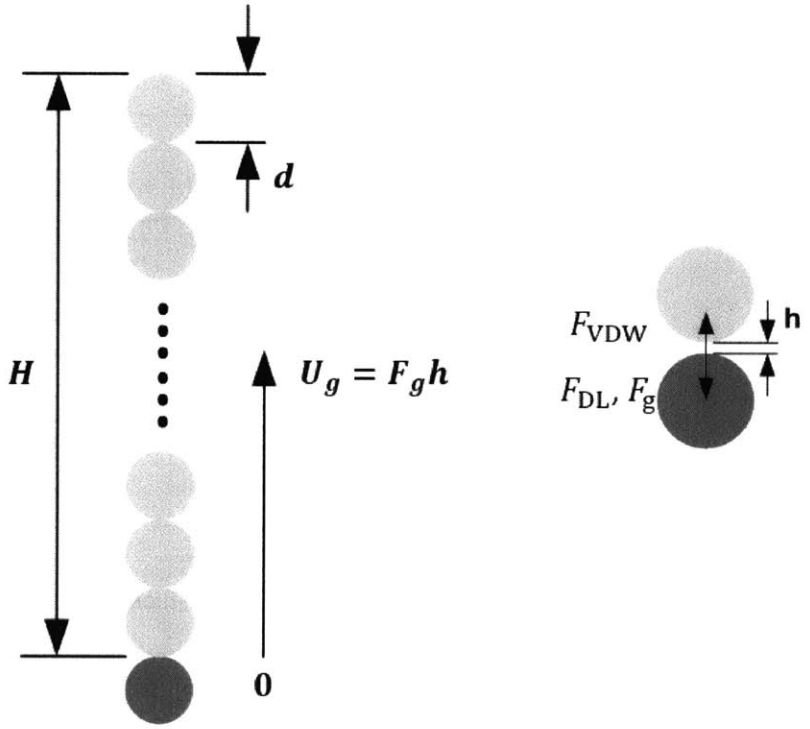

Fig. 5.17 Schematic of the particles stacking above the particle at the apex of the Taylor cone.

Hence the total interaction free energy is updated to

$$U_2 = U_{DL} + U_{VDW} - U_g = 2\pi\varepsilon\varepsilon_0 r\Psi^2 e^{-\kappa h} - \frac{Ar}{12h} - \frac{H}{d}\frac{4}{3}\pi r^3(\rho_p - \rho)gh \qquad (5.29)$$

Fig. 5.18 shows the plots of the updated total interaction free energy of the model system with different height of particle stacking above. From the figure we can clearly see that with the increase of the stacking height, the energy barrier is significantly decreased. When the particles above stack higher than 3 cm, the colloidal suspensions will coalesce rapidly to form aggregations. Actually, in our experiments, the usual stack height of the microparticles is estimated to be >2 cm (calculated from the amount of colloidal suspensions loaded), which greatly contribute to the formation of aggregations.

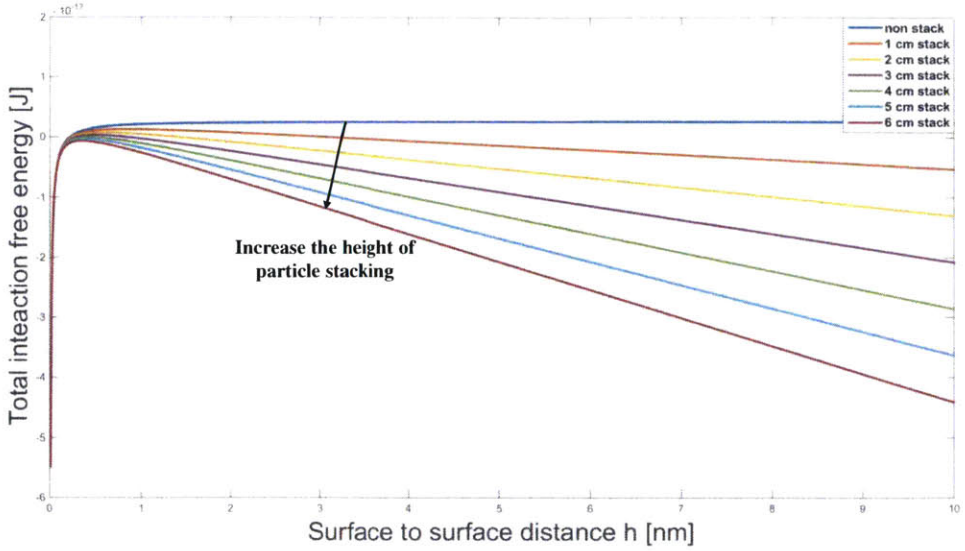

Fig. 5.18 Interaction free energy with different heights of particles stack above the microparticle at the apex of the Taylor cone.

5.5.1.4. Dependences on Particle Surface Potential and Size

We further looked into the dependence of the formation of the aggregations on the surface potential and size of the microparticles.

Fig. 5.19 shows the plots of the total interaction free energy with different surface potentials of the silica microparticles, under a 2 cm-high particle stack. With small surface potentials (e.g., -10 mV and -20 mV), particles are more likely to aggregate. When increase the surface potential, the self-repelling of between the microparticles become stronger and the energy barrier is harder to overcome, which effectively suppressed the aggregations.

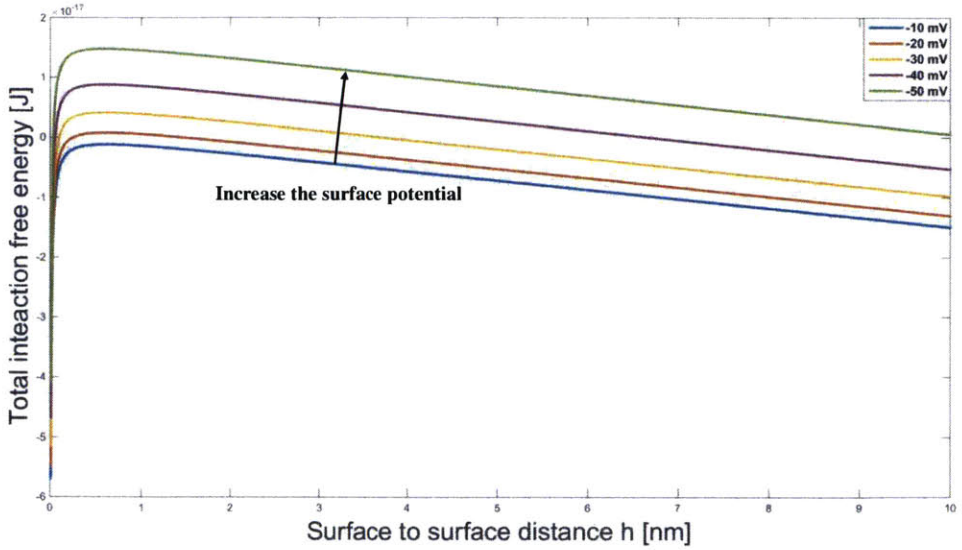

Fig. 5.19 Interaction free energy with different surface potentials of the silica microparticle.

Fig. 5.19 shows the plots of the total interaction free energy of the silica microparticles with different size, under a 2 cm-high particle stacking. Conclusion can be addressed that aggregations are more likely to form for small particles.

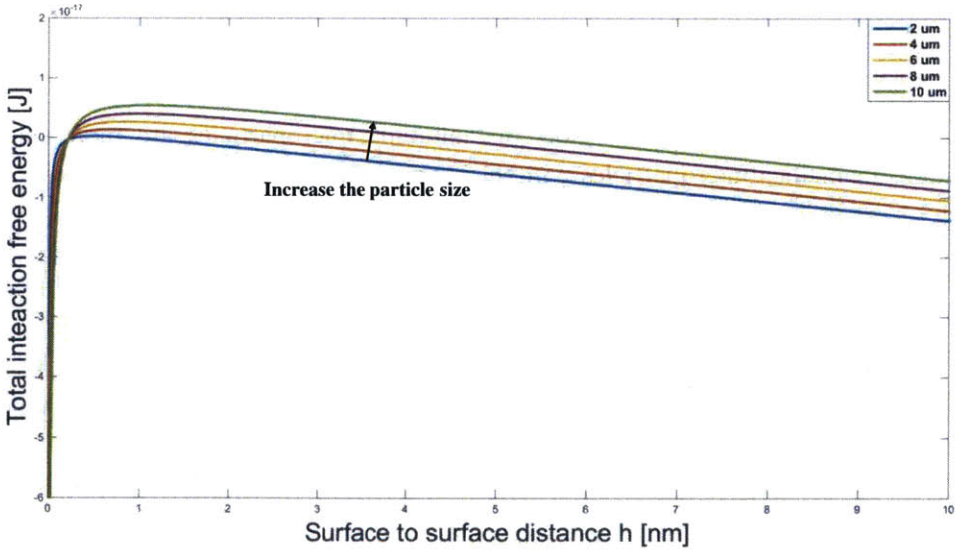

Fig. 5.20 Interaction free energy with different sizes of the silica microparticle.

5.5.1.5. Comparison between Silica and Alumina Particles

A quick comparison of the total interaction free energy of silica microparticles and alumina microparticles is shown in Fig. 5.21. The radius and the surface potential of both particles are 1.5 μm and -20 mV, respectively, and the stack of the particles above has a height of 1 mm.

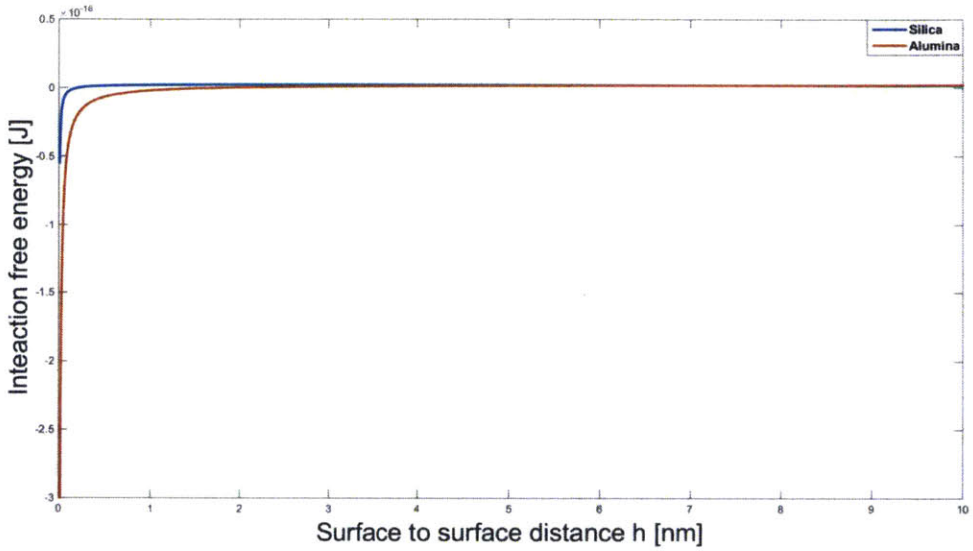

Fig. 5.21 Comparison of the interaction free energy between silica microparticles and alumina microparticles.

It is predicted from the above plots that alumina microparticles are more likely to form aggregations than silica microparticles with the same surface potential and size, due to

1. The density of alumina $\rho_{Al_2O_3} = 3.95\ \mathrm{g}/cm^3$ is larger than that of silica $\rho_{SiO_2} = 2.65\ \mathrm{g}/cm^3$, which makes the gravitational potential energy provided by the above alumina particles larger.
2. The Hamaker constant of alumina in water $A_{Al_2O_2} = 3.67 \times 10^{-20} J$ is also larger than that of silica $A_{SiO_2} = 0.46 \times 10^{-20} J$, which makes the contribution from the Van der Waals force to the interaction free energy larger to overcome the energy barrier.

The analysis above agrees with the observations from our experiments that, statically colloidal suspensions containing alumina microparticles are more likely than those containing silica microparticles to form aggregations near the meniscus, under the same experimental conditions.

5.5.2. Force Balance

Based on the analysis above, the dominant force balances during printing of microparticles might between: surface tension force F_γ, electrostatic force F_Φ and interparticle force F_p. The compression force F_g from the microparticles stacking above does not directly contribute to the force balance, but is included whiling analyzing F_p.

The characteristic pressures of the above forces exerting on the microparticle at the apex of the Taylor cone are

Pressure from surface tension

$$P_\gamma \sim \frac{\gamma}{r} \tag{5.30}$$

Pressure from electrical stress

$$P_\Phi \sim \varepsilon_0 \left(\frac{\Phi}{s}\right)^2 \tag{5.31}$$

Pressure from interparticle force:

$$P_\mathrm{p} \sim \frac{2\pi\varepsilon\varepsilon_0 r\kappa\Psi^2 e^{-\kappa h} - \frac{\mathrm{Ar}\ 1}{12h^2}}{r^2} = \frac{2\pi\varepsilon\varepsilon_0\kappa\Psi^2 e^{-\kappa h}}{r} - \frac{\mathrm{A}}{12}\frac{1}{rh^2} \sim \frac{A}{rh^2} \tag{5.32}$$

As in the regime where aggregation happens, Van der Waals forces dominates over the double layer force, i.e., $\frac{\mathrm{A}}{12}\frac{1}{rh^2} \gg \frac{2\pi\varepsilon\varepsilon_0\kappa\Psi^2 e^{-\kappa h}}{r}$, hence $\frac{2\pi\varepsilon\varepsilon_0\kappa\Psi^2 e^{-\kappa h}}{r} - \frac{\mathrm{A}}{12}\frac{1}{rh^2} \approx \frac{A}{rh^2}$.

While analytically calculating the electrostatic force is likely practically impossible due to the complexity of the distribution of the electric field and the surface charge, we will now analyze the formation of the particle streams mode and chunk of particles mode according to their dominant forces balances.

For the printing mode of particle streams, the electrostatic force exerted on the microparticle at the apex of the Taylor cone helps it to overcome the surface tension force and interparticle forces, therefore the constitutive law for the ejection of this particle is

$$\begin{array}{ccccc} F_\phi & \geq & F_\gamma & + & F_p \\ \int_s \left(\frac{1}{2}q\vec{E}\cdot\hat{z}\right)ds & \geq & 2\pi\gamma r\cos\left[\theta\left(1-h\sqrt{\frac{\pi r}{2V}}\right)\right] & + & 2\pi\varepsilon\varepsilon_0\kappa r\phi^2 e^{-\kappa h} - \frac{A}{12}\frac{r}{h^2} \\ \sim P_\phi r^2 & & \sim P_\gamma r^2 & & \sim P_p r^2 \end{array} \tag{5.33}$$

where $F_\gamma = 2\pi\gamma r\cos\left[\theta\left(1-h\sqrt{\frac{\pi r}{2V_b}}\right)\right]$ is the surface tension force between the two microparticles due to capillary bridge, V_b denotes the volume of the liquid between the particles and θ is the contact angle of the solvent on the silica surface [106].

Given the colloidal suspensions and system parameters, the characteristic bias voltage (given that the duration is long enough) is only dependent on the geometry of the Taylor cone G_T and the packing of the particles inside the meniscus, i.e., surface to surface distance between the particle and its adjacent particle h. There denote

$$V_{stream} = f(G_T, h) \tag{5.34}$$

While in the mode of chunk of particles, the large cluster of particles does not break down and is ejected in one piece. The meniscus pinches off the interface between the particle clusters, where the interparticle forces are the weakest, hence can be neglected. Therefore the electrostatic force exerted on particle cluster only needs to overcome the surface tension force, the constitutive law for the ejection of the large particle cluster is

$$\begin{array}{ccc} F_\phi & \geq & F_\gamma \\ \int_s \left(\frac{1}{2}q\vec{E}\cdot\hat{z}\right)ds & \geq & 2\pi\gamma L\cos\theta \\ \sim P_\phi r^2 & & \sim P_\gamma' L^2 \end{array} \tag{5.35}$$

L is the characteristic radius of the Taylor cone where the meniscus pinches off to eject the large cluster of particles (Fig. 5.22), $F_\gamma = 2\pi\gamma L\cos\theta$ is the surface tension force exerted on the aggregation and $P_\gamma' \sim \frac{\gamma}{L}$ is the characteristic pressure due to surface tension on the aggregation.

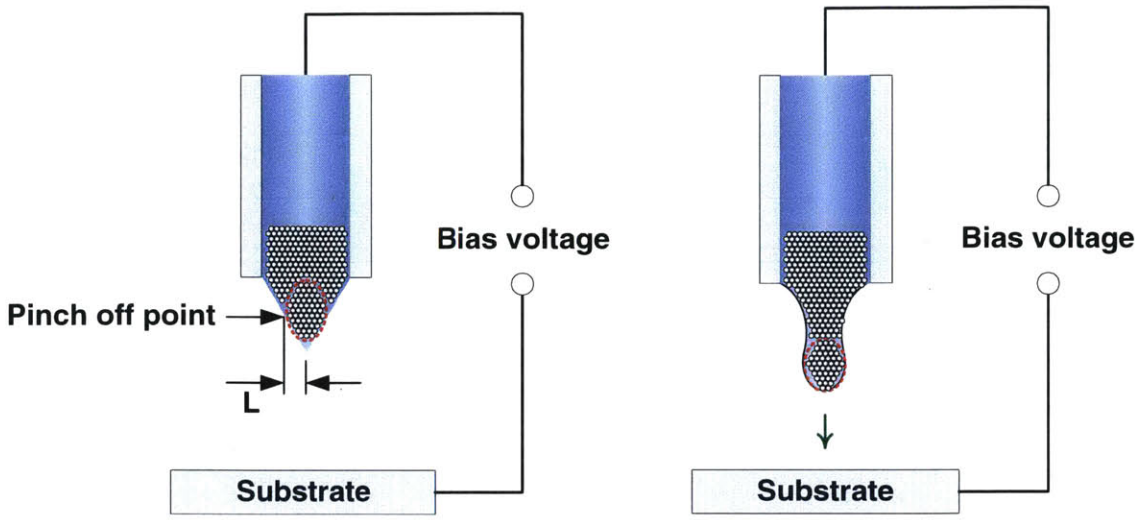

Fig. 5.22 Mechanism of the ejection mode of chunk of particles, the dashed line indicates the large particle cluster.

Given the system parameters, the characteristic bias voltage to eject the chunk of particles is only dependent on the geometry of the Taylor cone and the characteristic radius of the cluster, which can be denoted as

$$V_{chunk} = g(G_T, L) \tag{5.36}$$

Therefore, for microparticles stacking at the tip of the capillary near the meniscus, there are two different characteristic values of the bias voltage pulse which induce different ejection modes respectively:

1. V_{stream} to induce the mode of particle streams.
2. V_{chunk} to induce the mode of chunk of particles.

The actual mode of printing microparticles is determined by the relationships between the bias voltage V and the two characteristic voltages V_{stream} and V_{chunk}, which are summarized in the Table 5.5 below.

Conditions	Bias voltage	Mode
$V_{stream} < V_{chunk}$	$V < V_{stream}$	Non-ejection
	$V_{stream} \leq V < V_{chunk}$	Particle stream
	$V_{chunk} \leq V$	Both modes might happen[13]
$V_{chunk} \leq V_{stream}$	$V < V_{chunk}$	Non-ejection
	$V_{chunk} \leq V < V_{stream}$	Chunk of particles
	$V_{stream} \leq V$	Both modes might happen

Table 5.5 Printing conditions of particle streams mode versus chunk of particles mode.

5.6. EHD Printing of Particle Streams onto Porous Media

In the previous sections, we have demonstrated on-demand EHD printing of particle streams onto flat and compact substrates (e.g., glass microscope slides with or without copper tapes, silica and silicon wafers). In this chapter, new AM capabilities of printing particle streams towards fabricating multi-material composites are presented, including printing colloidal suspensions onto carbon nanotube (CNT) forests, and deposition of ceramic microparticles onto a metal powder bed and laser consolidation afterwards.

5.6.1. Printing Particle Streams onto Carbon Nanotube Forests

In this section, we demonstrate the capability of on-demand EHD printing of particle streams of depositing colloidal suspensions onto porous materials. We anticipate that the solvent in the printed matter will wick into the porous media rapidly upon contacting the substrate, which effectively eliminates the spreading of the printed pattern and thereby enhances printing resolution and positioning accuracy.

The colloidal suspensions we used in this demonstration were 3 μm diameter silica microparticles (Corpuscular Inc., Monodisperse Silica Microspheres) dispersed in water glycerin mixture with a volume fraction of 10:1. The initial volume fraction of silica microparticles before loading is 4.5%.

The nanoporous media used in this experiment is vertically aligned carbon nanotube (CNT) forests. The CNT forests were synthesized by chemical vapor deposition (CVD) on a piece of silicon wafer. An Al_2O_3/Fe (10 nm/1 nm) layer was deposited on the wafer as catalysts by electron

[13] The bias voltage is large enough to induce both modes, while we expect that which mode will finally occur depends on their relative time scale.

beam deposition before growth. The as-grown CNT forests were then coated with Al_2O_3 using atomic layer deposition (ALD) for 150 cycles, in order to prevent the forests from deformation due to capillary shrinkage. The height of the CNT forests is 40 μm. The size of the pores in the CNT forests is ~100 nm, which is much less than the diameter of the silica microparticles of 3 μm, hence the microparticles will not wick into the CNT forests. SEM images of the CNT forests (both before and after ALD coating) are shown in Fig. 5.23.[14]

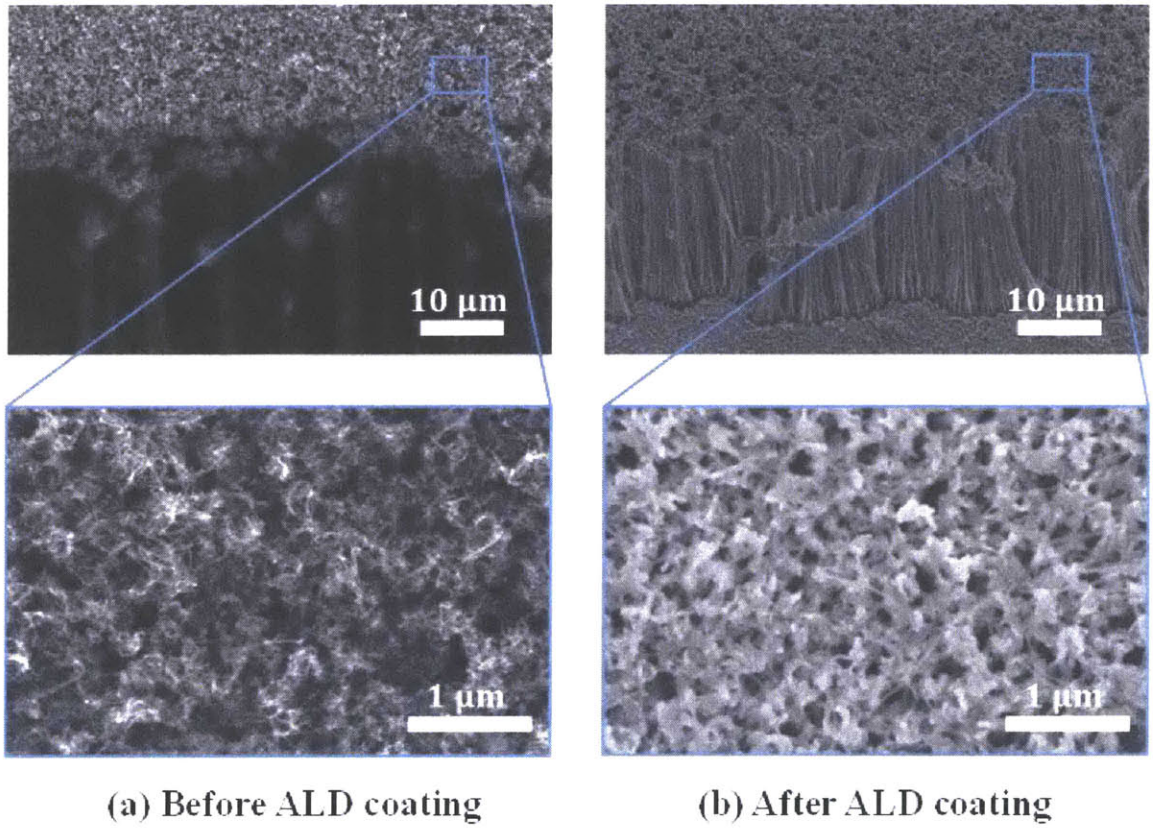

Fig. 5.23 SEM images of CNT forests: (a) Before ALD coating; (b) After ALD coating of alumina.

The CNT sample was placed on a glass microscope slide covered with a copper tape, which functions as the counter electrode. The schematic is illustrated in Fig. 5.24.

[14] Thanks to Hangbo Zhao for helping prepare the CNT samples.

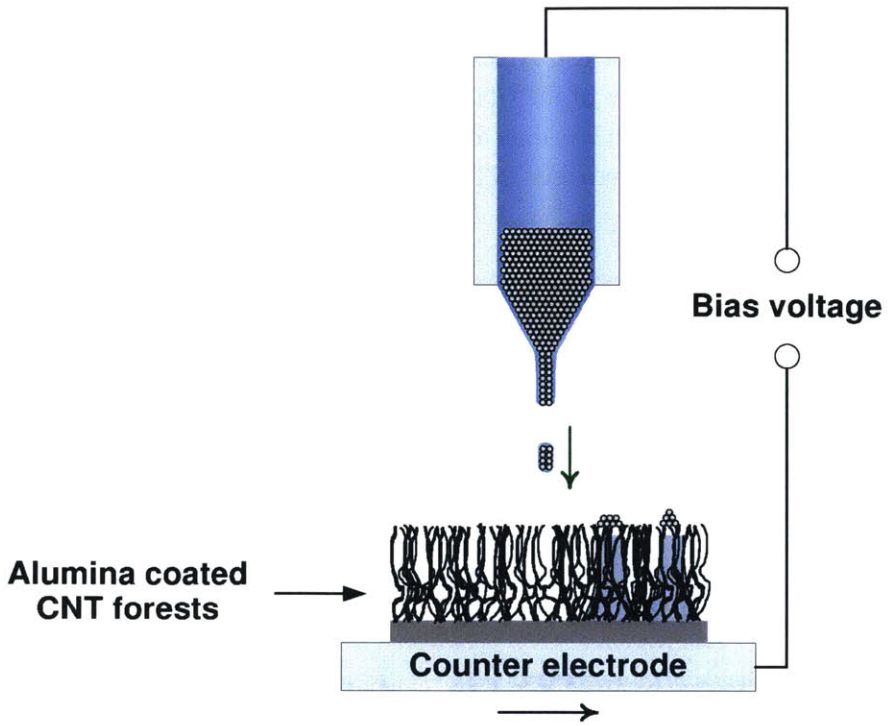

Fig. 5.24 Schematic of EHD printing of silica microparticle streams onto alumina ALD coated CNT forests.

Fig. 5.25 presents a sequence of snapshots of the printing event from the high speed video. The printing parameters are summarized as follows:

- Separation between the tip of the capillary and the top of the CNT forests: 250 μm.
- Bias voltage:
  - Baseline voltage: 1 kV.
  - Pulse amplitude: 2 kV.
  - Pulse duration: 5 ms.

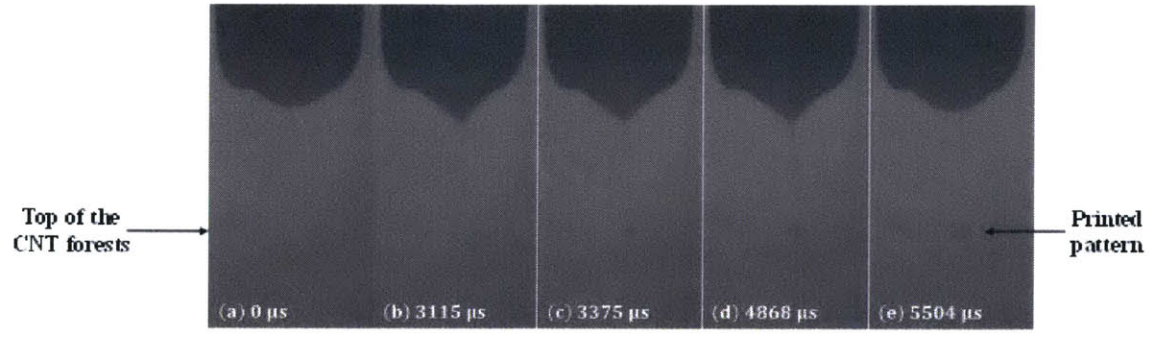

Fig. 5.25 A sequence of snapshots of on-demand EHD printing of silica microparticle streams onto alumina ALD coated CNT forests.

Fig. 5.26 shows the SEM images of the top view of the CNT forests with silica microparticles printed.

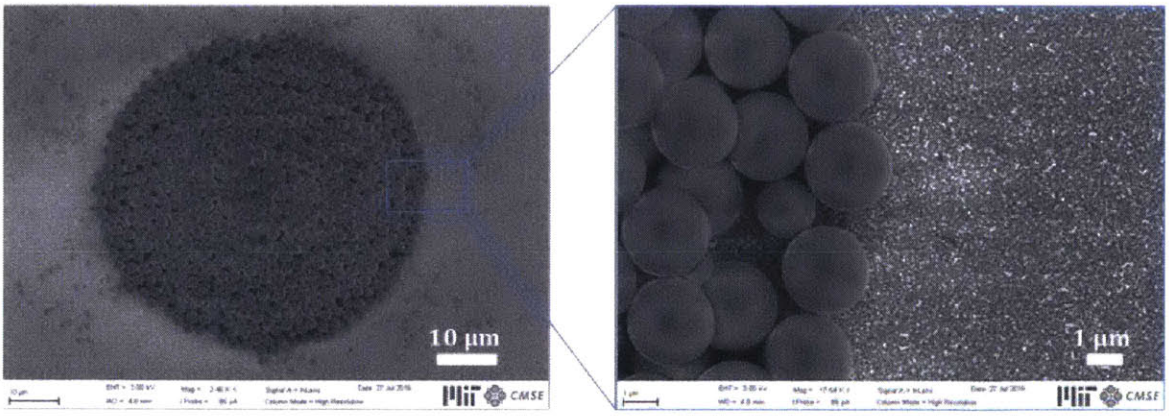

Fig. 5.26 SEM images of alumina ALD coated CNT forests with silica microparticles printed.

Actually, from the high speed recording of the printing event, we can hardly observe the wicking process of the solvent by the CNT forests. This may be because of the low concentration of the solvent in the particle streaming scheme hence the amount of the solvent ejected onto the CNT forests was too little for us to observe its wicking process.

The sample was imaged through a microscope immediately after printing and no solvent was found on the CNT forests. As glycerin had been added to the colloidal suspensions which reduces its evaporation rate, the time needed for the solvent in the similar ~50 μm diameter pattern on a glass microscope slide to dry out after printing is usually >1 h from past experiences. Hence this indicates the ability of the CNT forests to rapidly wick the solvent from the printed pattern.

Moreover, the printed pattern presents a nice round shape and there are no satellite patterns on the CNT forests. This is enhanced by the solvent wicking by the CNT forests hence the spread of the printed matter is suppressed effectively. Fig.5.27 shows some typical patterns of printing the same colloidal suspensions onto glass microscope slides, which have relatively poor sphericity and satellite particles can be observed around the main pattern.

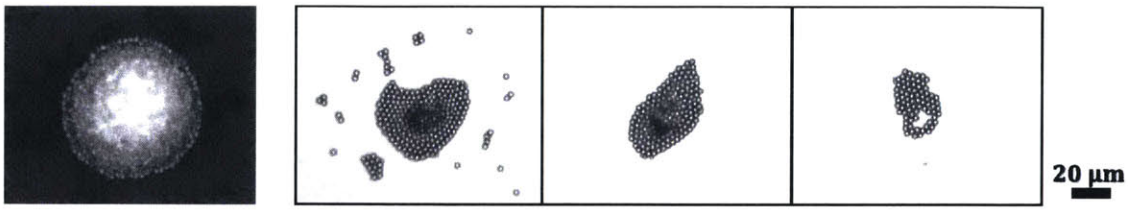

(a) Onto CNT forests **(b) Onto glass microscope slides**

Fig. 5.27 Comparison of printed patterns of silica microparticles onto CNT forests versus onto glass microscope slides: (a) Onto alumina ALD coated CNT forests; (b) Onto glass microscope slides.

5.6.2. Printing Particle Streams onto Metal Powder Beds

Metal-ceramic composites are of great interests to us due to its property of combined high stiffness, high ductility, and low density. Our approach of manufacturing the metal-ceramic composites is to print ceramic microparticles via on-demand EHD printing of particle streams onto a metal powder bed and selectively laser melt (SLM) the mixture afterwards.

We have demonstrated the first experiment of printing ceramic microparticles onto a metal powder bed and laser consolidating the mixture using the atmosphere controlled additive manufacturing (ACAM) apparatus built in our group. The preliminary results, analysis and future improvements are presented as follows.

The ceramics we used were colloidal suspensions containing 3 μm diameter alumina microparticles (Corpuscular Inc., Plain Al2O3 microspheres, 3 μm). The solvent and the initial volume fraction of the microparticles before loading are the same as above. The metal powder bed was 316L stainless steel 3D powders with diameter ranging from 15 μm to 45 μm purchased from John Galt Steel.

The schematic of the printing process is shown in Fig. 5.28. The metal powder bed functions both as the substrate and as the counter electrode in this experiment.

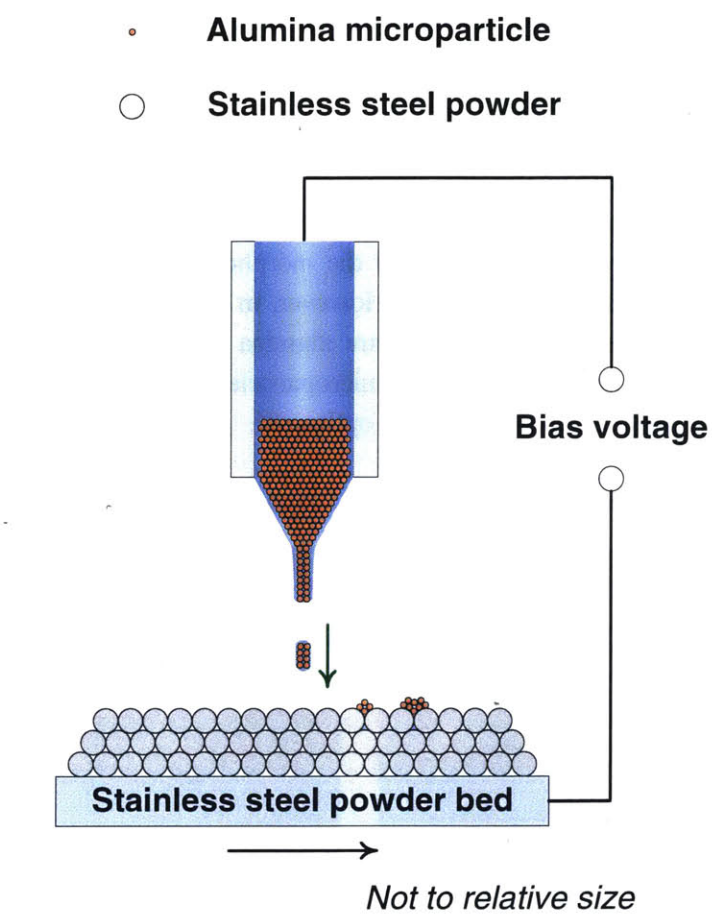

Fig. 5.28 Schematic of EHD printing of alumina microparticle streams onto a stainless steel powder bed.

The printing was done by applying a bias voltage pulse with a baseline amplitude of 1 kV as well as the pulse amplitude and duration of 1 kV and 5 ms, respectively. The separation between the tip of the capillary and the top of the powder bed is 1.5 mm. The interaction between the ejected materials and the powder bed was not captured by the high speed camera due to the large separation of the capillary and the powder bed therefore the powder bed was not brought into the field view. The capillary to substrate distance was chosen to be much larger than those of other substrates (~250 μm) because: in the current experimental setup, the stainless steel powder bed functions as the counter electrode as well. Hence when the bias voltage pulses are applied, the metal powders will feel the electrostatic attraction from the meniscus to move upwards and stick to the meniscus. This problem poses great challenge to the accurate positioning of fine ceramic patterns onto the metal powder bed and the uniformity of the deposition, as the distribution of the electric field and the motion of the droplet between the capillary and the substrate are disturbed by the motion of the metal powders.

The laser sintering was done using the ACAM apparatus, which is a customized SLM machine built in our group. Our sample was sintered in the atmospheric condition with 35 W power and a scanning speed at 25 mm/s.

Fig. 5.29 shows the optical microscope images of the mixture of stainless steel powders and alumina microparticles, before and after laser sintering, respectively.
It can be observed that laser sintering changed the morphology of the mixture as well as the distribution of the powders and microparticles. However, in this experiment strong balling effect of the metal powders is observed while there are alumina microparticles remaining unmelted. Hence, more uniform deposition of the alumina microparticles onto the stainless steel powder bed is needed and the sintering conditions need to be optimized.

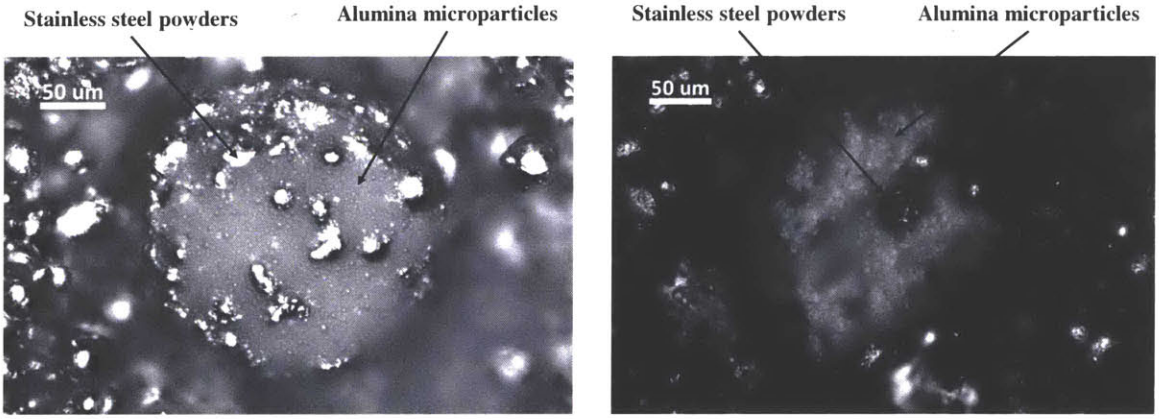

(a) Before laser sintering **(b) After laser sintering**

Fig. 5.29 Optical microscope images of the mixture of alumina microparticles and stainless steel powder bed: (a) Before laser sintering; (b): After laser sintering.

SEM images of the mixture after laser sintering are shown in Fig. 5.30. The balling phenomena of the sintering process and unmelted alumina microparticles can be observed clearly from the images. Moreover, from the profile of the surface of one of the balls in the mixture, the shape of the alumina microparticles can be found. This indicates the coalescence of alumina and stainless steel due to laser sintering.

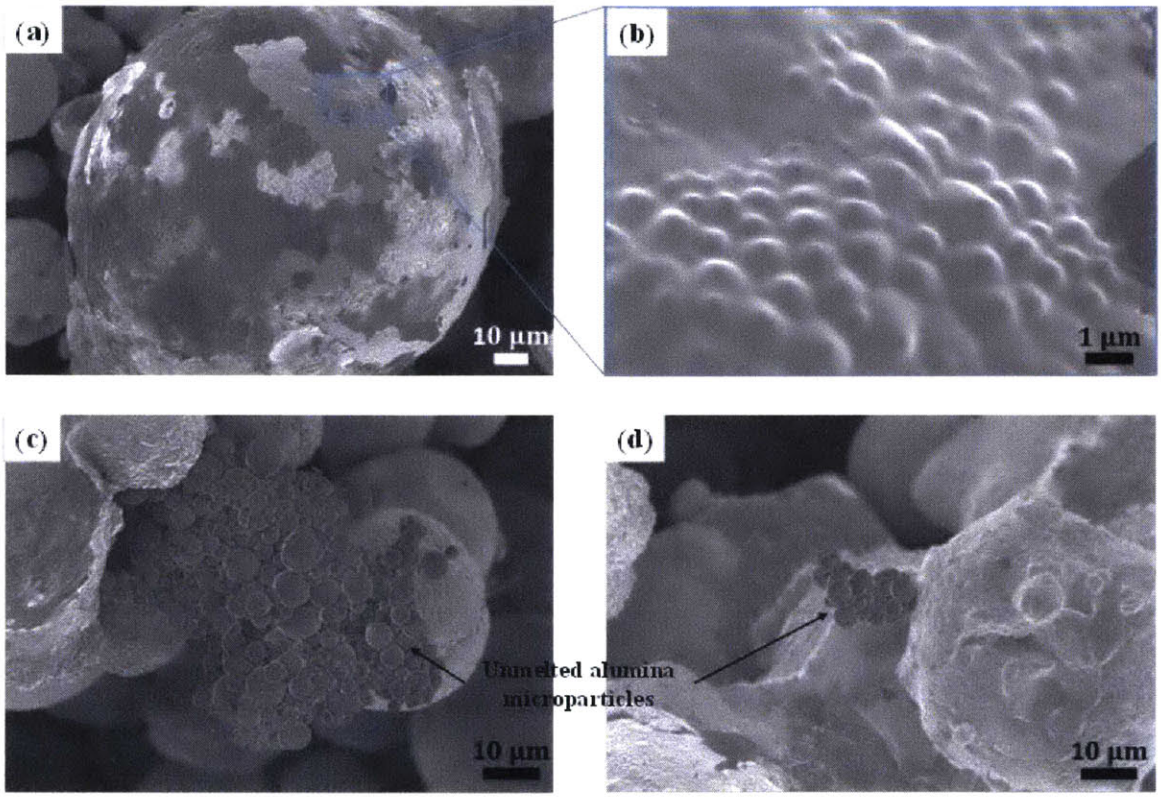

Fig. 5.30 SEM images of the mixture of alumina microparticles and stainless steel powder bed after laser sintering: (a) Balling phenomena; (b) Profile of the ball shows the shape of alumina microparticles and indicates the coalescence of the stainless steel powders and the alumina microparticles; (c) and (d): Unmelted alumina microparticles.

The pattern after laser sintering we presented here in our first experiment had defects due to balling phenomena and poor deposition uniformity, potential solutions to improve the quality of the metal-ceramic composited will be discussed in Chapter 6.

this page intentionally left blank

Chapter 6: Conclusions and Future Work

The major contributions and the future directions for the extension of this work are highlighted below.

6.1. Contributions

The main contributions of this work are:

1. A customized single-tip apparatus has been designed and constructed for the experimental study of on-demand EHD printing of particle streams, which is capable of characterizing the printing processes via synchronized high speed recording of the printing events, control of the bias voltage profiles and measurement of the printing current between the tip and substrate.
2. Dot arrays with 20 μm feature size and continuous lines are printed from colloidal suspensions containing 3 μm diameter PS microparticles and 3 μm diameter alumina microparticles, using the mode-controlled continuous EHD jetting mechanism. The radius and spacing of the dot arrays are found to increase when increasing the external flow rate and decreasing the substrate motion speed, yet do not depend on the amplitude of the bias voltage directly. A mathematical model is utilized to predict the radius and spacing of the dot arrays, which are verified to scale with the square root of the external flow rate. The scaling relationship obtained from the model shows a good agreement with the experimental results.
3. It has been shown that small numbers of microparticles can be ejected by EHD printing, which has great potential as a direct-write AM approach for microparticulate materials, in contrast with conventional EHD-driven inkjet printing techniques which are only capable of printing homogeneously dispersed functional inks, including nanoparticulate materials, molecular and polymers.
4. It has been shown that pulsed voltage signals are capable of inducing EHD printing from capillary tips with sedimented particles and resulting in ejection of liquid droplets, streams, and aggregates containing microparticles, at rates of ~10 kHz.
5. The mode of ejection under this condition depends strongly on the packing of the particles within the meniscus, their size and properties, the strength of the double layer force and Van der Waals interactions, and the profile of the bias voltage pulses. And this is rationalized by analysis of the scaling of forces exerted on the microparticle at the apex of the Taylor cone upon ejection.
6. It has been demonstrated that these conditions can be applied for on-demand deposition of microparticles with different sizes and materials, including 3 μm and 7 μm diameter silica microparticles, 3 μm diameter alumina microparticles and 10 μm diameter PS microparticles.
7. Demonstration experiments have been performed to show that the EHD process developed here can be used to deposit microparticle clusters on porous materials. Specifically, it has been shown that: 1) EHD printing of silica microparticle streams onto alumina coated CNT

forests; 2) EHD printing of alumina microparticle streams onto a stainless steel powder bed.

6.2. Future Work:

The findings above validate the capability to use EHD to deposit microparticles from liquid carriers. Potential areas of future investigation are outlined below.

1. **Experimental apparatus**
   The printing current measurement module in our experimental apparatus has been demonstrated to be capable of recognizing different EHD ejection modes and correlating with individual printing events. More efforts are needed to potentially enable: 1) automatic stabilization of the ejection mode by coordination of the liquid flow and the printing signal; 2) feedback control of the printing process via peak detection of the printing current. Further study is needed to determine if the charge transfer can be a reliable measure of the amount of liquid and solid deposited in each event.
2. **Understanding of aggregations**
   More comprehensive models need to be developed in order to understand the formation and properties of the particle aggregations inside the meniscus. This will guide the design of parametric experiments accordingly to investigate the aggregation behaviors and how they affect the performances of EHD printing of particle streams as well.
3. **Scalings of the printing quality**
   Further parametric study and scaling analysis can determine the relationships between the printing quality (for example, ejection rate, feature size, positioning accuracy, throughput and repeatability) and the printing parameters, including the properties and size of the colloidal suspensions, profile of the bias voltage, system geometries and etc.
4. **Particle delivery mechanism**
   One critical requirement for EHD printing of particle streams is to deliver particles to the tip of the capillary at which point they can be printed. Other particle delivery mechanisms could be investigated in order to: 1) transport microparticles with diameter < 1 μm where the natural sedimentation due to gravitational force is not sufficient; 2) achieve controlled delivery of particles to the meniscus during the printing process to mitigate aggregations due to particle sedimentation.
5. **More AM capabilities**
   More AM capabilities via EHD printing of particle streams will be explored, including printing metallic microparticles, fabricating multi-material and multi-dimensional composites. It would also be attractive to integrate EHD microparticle deposition with powder-based metal AM methods such as selective laser melting (following our discussion in Chapter 5). For this, the concept of deposition onto a powder bed may be employed. A secondary counter electrode design will be used in order to prevent the metal powders from being attracted to the meniscus. The schematic is shown in Fig. 6.1. In this design the metal powder bed only functions as the substrate where ejected colloidal suspensions will finally land. Therefore by adjusting the distance between the metal powder bed and the tip of the

capillary, the electrostatic attraction exerted on the metal powders can be greatly reduced to prevent the upward motion of the powders while the force needed to eject colloidal suspensions is preserved.

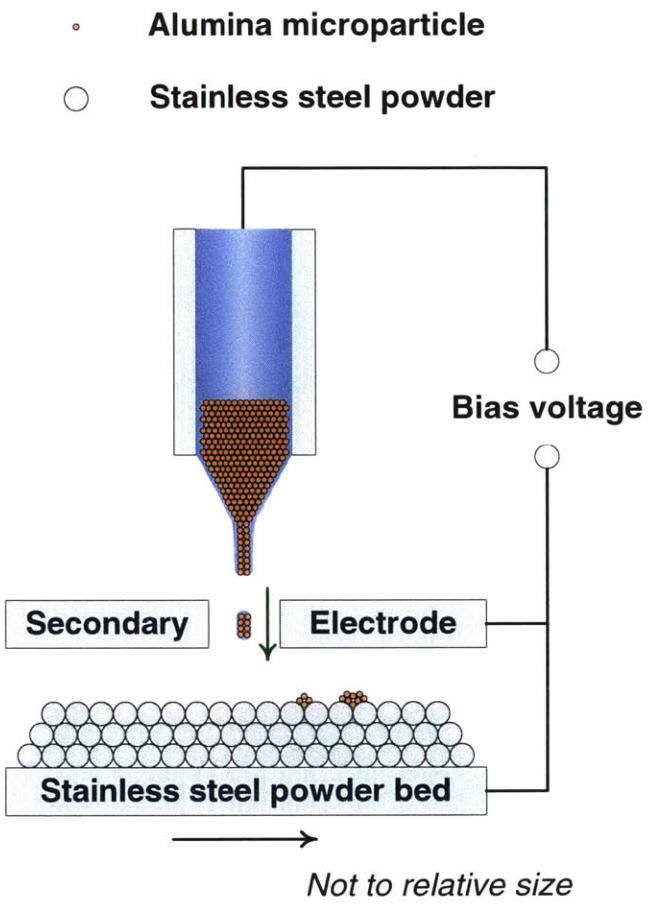

Fig. 6.1 Design of a secondary electrode for EHD printing of ceramic microparticle streams onto a metal powder bed.

this page intentionally left blank

Bibliography

[1]. Kalpakjian, Serope. Manufacturing engineering and technology. Pearson Education India, 2001.

[2]. Gibson, Ian, David W. Rosen, and Brent Stucker. Additive manufacturing technologies. Vol. 238. New York: Springer, 2010.

[3]. "ASTM F2792-12a: Standard Terminology for Additive Manufacturing Technologies." ASTM International, West Conshohocken, 2013.

[4]. "Sustainable Manufacturing." An Integrated STEM Approach for Aerospace Studies. N.p., n.d. Web. 22 Aug. 2016.

[5]. "Fused Deposition Modeling." Wikipedia. Wikimedia Foundation, n.d. Web. 18 Aug. 2016.

[6]. Hornbeck, Larry J. "Digital light processing and MEMS: an overview."Advanced Applications of Lasers in Materials Processing/Broadband Optical Networks/Smart Pixels/Optical MEMs and Their Applications. IEEE/LEOS 1996 Summer Topical Meetings:. IEEE, 1996.

[7]. "Digital Light Processing." Wikipedia. Wikimedia Foundation, n.d. Web. 18 Aug. 2016.

[8]. Feygin, Michael, and Sung Sik Pak. "Laminated object manufacturing apparatus and method." U.S. Patent No. 5,876,550. 2 Mar. 1999.

[9]. "Laminated Object Manufacturing." Wikipedia. Wikimedia Foundation, n.d. Web. 18 Aug. 2016.

[10]. Taminger, Karen, and Robert A. Hafley. "Electron beam freeform fabrication: a rapid metal deposition process." (2003).

[11]. "Electron Beam Freeform Fabrication." Wikipedia. Wikimedia Foundation, n.d. Web. 18 Aug. 2016.

[12]. Lü, Li, Jerry Ying Hsi Fuh, and Yoke-San Wong. "Selective Laser Sintering."Laser-Induced Materials and Processes for Rapid Prototyping. Springer US, 2001. 89-142.

[13]. "Selective Laser Sintering." Wikipedia. Wikimedia Foundation, n.d. Web. 18 Aug. 2016.

[14]. Gibson, Ian, David Rosen, and Brent Stucker. "Directed Energy Deposition Processes." Additive Manufacturing Technologies. Springer New York, 2015. 245-268.

[15]. Jacobs, Paul Francis. Rapid prototyping & manufacturing: fundamentals of stereolithography. Society of Manufacturing Engineers, 1992.

[16]. "Stereolithography." Wikipedia. Wikimedia Foundation, n.d. Web. 18 Aug. 2016.

[17]. Derby, Brian. "Inkjet printing of functional and structural materials: fluid property requirements, feature stability, and resolution." Annual Review of Materials Research 40 (2010): 395-414.

[18]. Onses, M. Serdar, et al. "Mechanisms, Capabilities, and Applications of High-Resolution Electrohydrodynamic Jet Printing." small 11.34 (2015): 4237-4266.

[19]. Perelaer, Jolke, et al. "Printed electronics: the challenges involved in printing devices, interconnects, and contacts based on inorganic materials." Journal of Materials Chemistry 20.39 (2010): 8446-8453.

[20]. Singh, Madhusudan, et al. "Inkjet printing—process and its applications."Advanced materials 22.6 (2010): 673-685.

[21]. Castrejon-Pita, J. Rafael, et al. "Future, opportunities and challenges of inkjet technologies." Atomization and Sprays 23.6 (2013).

[22]. Tekin, Emine, Patrick J. Smith, and Ulrich S. Schubert. "Inkjet printing as a deposition and patterning tool for polymers and inorganic particles." Soft Matter 4.4 (2008): 703-713.

[23]. Melcher, J. R., and G. I. Taylor. "Electrohydrodynamics: a review of the role of interfacial shear stresses." Annual Review of Fluid Mechanics 1.1 (1969): 111-146.

[24]. Ziabicki, Andrzej. Fundamentals of fibre formation. Wiley, 1976.

[25]. " Electrospinning." Wikipedia. Wikimedia Foundation, n.d. Web. 18 Aug. 2016.

[26]. Tanski, M., et al. "A System for Cooling Electronic Elements with an EHD Coolant Flow." Journal of Physics: Conference Series. Vol. 494. No. 1. IOP Publishing, 2014.

[27]. " Electrohydrodynamics." Wikipedia. Wikimedia Foundation, n.d. Web. 18 Aug. 2016.

[28]. Masuyama, Kento, and Steven RH Barrett. "On the performance of electrohydrodynamic propulsion." Proc. R. Soc. A. Vol. 469. No. 2154. The Royal Society, 2013.

[29]. "Ionocraft." Wikipedia. Wikimedia Foundation, n.d. Web. 18 Aug. 2016.

[30]. Gomez, Alessandro, and Keqi Tang. "Charge and fission of droplets in electrostatic sprays." Physics of Fluids (1994-present) 6.1 (1994): 404-414.

[31]. "Electrospray." Wikipedia. Wikimedia Foundation, n.d. Web. 18 Aug. 2016.

[32]. Saville, D. A. "Electrohydrodynamics: the Taylor-Melcher leaky dielectric model." Annual review of fluid mechanics 29.1 (1997): 27-64.

[33]. Grimm, Ronald L. Fundamental studies of the mechanisms and applications of field-induced droplet ionization mass spectrometry and electrospray mass spectrometry. Diss. California Institute of Technology, 2005.

[34]. Frs, L. R. "On the equilibrium of liquid conducting masses charged with electricity', Lond." Edinb. Dublin Philos. Mag. J. Sci 14 (1882): 87.

[35]. Taflin, Daniel C., Timothy L. Ward, and E. James Davis. "Electrified droplet fission and the Rayleigh limit." Langmuir 5.2 (1989): 376-384.

[36]. Zeleny, John. "The electrical discharge from liquid points, and a hydrostatic method of measuring the electric intensity at their surfaces." Physical Review3.2 (1914): 69.

[37]. Zeleny, John. "Instability of electrified liquid surfaces." Physical review 10.1 (1917): 1.

[38]. Allan, R. S., and S. G. Mason. "Particle behaviour in shear and electric fields. I. Deformation and burst of fluid drops." Proceedings of the Royal Society of London A: Mathematical, Physical and Engineering Sciences. Vol. 267. No. 1328. The Royal Society, 1962.

[39]. Taylor, Geoffrey. "Disintegration of water drops in an electric field."Proceedings of the Royal Society of London A: Mathematical, Physical and Engineering Sciences. Vol. 280. No. 1382. The Royal Society, 1964.

[40]. Suvorov, Vasily G., and Nikolay M. Zubarev. "Formation of the Taylor cone on the surface of liquid metal in the presence of an electric field." Journal of Physics D: Applied Physics 37.2 (2003): 289.

[41]. Collins, Robert T., Michael T. Harris, and Osman A. Basaran. "Breakup of electrified jets." Journal of Fluid Mechanics 588 (2007): 75-129.

[42]. Xu, Shenren. Operating regimes of self-regulated electrohydrodynamic cone-jets. 2010.

[43]. Yogi, Osamu, et al. "On-demand droplet spotter for preparing pico-to femtoliter droplets on surfaces." Analytical chemistry 73.8 (2001): 1896-1902.

[44]. Chen, C-H., D. A. Saville, and I. A. Aksay. "Electrohydrodynamic "drop-and-place" particle deployment." Applied physics letters 88.15 (2006): 154104.

[45]. Chen, C-H., D. A. Saville, and I. A. Aksay. "Scaling laws for pulsed electrohydrodynamic drop formation." Applied physics letters 89.12 (2006): 124103.

[46]. Onses, M. Serdar, et al. "Hierarchical patterns of three-dimensional block-copolymer films formed by electrohydrodynamic jet printing and self-assembly." Nature nanotechnology 8.9 (2013): 667-675.

[47]. Onses, M. Serdar, et al. "Block copolymer assembly on nanoscale patterns of polymer brushes formed by electrohydrodynamic jet printing." ACS nano 8.7 (2014): 6606-6613.

[48]. Shigeta, Kazuyo, et al. "Functional protein microarrays by electrohydrodynamic jet printing." Analytical chemistry 84.22 (2012): 10012-10018.

[49]. Shigeta, Kazuyo, et al. "Functional protein microarrays by electrohydrodynamic jet printing." Analytical chemistry 84.22 (2012): 10012-10018.

[50]. Park, Jang-Ung, et al. "High-resolution electrohydrodynamic jet printing."Nature materials 6.10 (2007): 782-789.

[51]. Park, Jang-Ung, et al. "Nanoscale patterns of oligonucleotides formed by electrohydrodynamic jet printing with applications in biosensing and nanomaterials assembly." Nano letters 8.12 (2008): 4210-4216.

[52]. Lee, Ayoung, et al. "Optimization of experimental parameters to determine the jetting regimes in electrohydrodynamic printing." Langmuir 29.44 (2013): 13630-13639.

[53]. Collins, Robert T., et al. "Universal scaling laws for the disintegration of electrified drops." Proceedings of the National Academy of Sciences 110.13 (2013): 4905-4910.

[54]. Collins, Robert T., et al. "Electrohydrodynamic tip streaming and emission of charged drops from liquid cones." Nature Physics 4.2 (2008): 149-154.

[55]. Mishra, Sandipan, et al. "High-speed and drop-on-demand printing with a pulsed electrohydrodynamic jet." Journal of Micromechanics and Microengineering 20.9 (2010): 095026.

[56]. Stachewicz, Urszula, et al. "Experiments on single event electrospraying."Applied Physics Letters 91.25 (2007): 254109.

[57]. Kim, Joonghyuk, Hyuncheol Oh, and Sang Soo Kim. "Electrohydrodynamic drop-on-demand patterning in pulsed cone-jet mode at various frequencies."Journal of Aerosol Science 39.9 (2008): 819-825.

[58]. Stachewicz, Urszula, et al. "Stability regime of pulse frequency for single event electrospraying." Applied Physics Letters 95.22 (2009): 224105.

[59]. Choi, Jaeyong, et al. "Drop-on-demand printing of conductive ink by electrostatic field induced inkjet head." Applied Physics Letters 93.19 (2008): 193508.

[60]. Chen, C-H., D. A. Saville, and I. A. Aksay. "Electrohydrodynamic "drop-and-place" particle deployment." Applied physics letters 88.15 (2006): 154104.

[61]. Lee, Sukhan, et al. "Satellite/spray suppression in electrohydrodynamic printing with a gated head." Applied Physics Letters 103.13 (2013): 133506.

[62]. Tse, Leo, and Kira Barton. "A field shaping printhead for high-resolution electrohydrodynamic jet printing onto non-conductive and uneven surfaces."Applied Physics Letters 104.14 (2014): 143510.

[63]. Wei, Chuang, et al. "High-resolution ac-pulse modulated electrohydrodynamic jet printing on highly insulating substrates." Journal of Micromechanics and Microengineering 24.4 (2014): 045010.

[64]. Wei, Chuang, et al. "Drop-on-demand E-jet printing of continuous interconnects with AC-pulse modulation on highly insulating substrates."Journal of Manufacturing Systems 37 (2015): 505-510.

[65]. Sutanto, Erick, and Andrew G. Alleyne. "Norm Optimal Iterative Learning Control for a Roll to Roll nano/micro-manufacturing system." 2013 American Control Conference. IEEE, 2013.

[66]. Choi, Kyung Hyun, Muhammad Zubair, and Hyun Woo Dang. "Characterization of flexible temperature sensor fabricated through drop-on-demand electrohydrodynamics patterning." Japanese Journal of Applied Physics 53.5S3 (2014): 05HB02.

[67]. Sutanto, E., et al. "A multimaterial electrohydrodynamic jet (E-jet) printing system." Journal of Micromechanics and Microengineering 22.4 (2012): 045008.

[68]. Barton, Kira, et al. "A desktop electrohydrodynamic jet printing system."Mechatronics 20.5 (2010): 611-616.

[69]. Grilli, Simonetta, et al. "3D lithography by rapid curing of the liquid instabilities at nanoscale." Proceedings of the National Academy of Sciences 108.37 (2011): 15106-15111.

[70]. Cai, Yanli, et al. "Collagen grafted 3D polycaprolactone scaffolds for enhanced cartilage regeneration." Journal of Materials Chemistry B 1.43 (2013): 5971-5976.

[71]. Galliker, Patrick, et al. "Direct printing of nanostructures by electrostatic autofocussing of ink nanodroplets." Nature communications 3 (2012): 890.

[72]. Han, Yiwei, Chuang Wei, and Jingyan Dong. "Super-resolution electrohydrodynamic (EHD) 3D printing of micro-structures using phase-change inks." Manufacturing Letters 2.4 (2014): 96-99.

[73]. Lee, Sangkyu, et al. "Patterned oxide semiconductor by electrohydrodynamic jet printing for transparent thin film transistors." Applied physics letters 100.10 (2012): 102108.

[74]. Jeong, Sunho, et al. "Metal salt-derived In–Ga–Zn–O semiconductors incorporating formamide as a novel co-solvent for producing solution-processed, electrohydrodynamic-jet printed, high performance oxide transistors." Journal of Materials Chemistry C 1.27 (2013): 4236-4243.

[75]. Awais, Muhammad Naeem, et al. "ZrO 2 flexible printed resistive (memristive) switch through electrohydrodynamic printing process." Thin Solid Films 536 (2013): 308-312.

[76]. Back, Sung Yul, et al. "Drop-on-demand printing of carbon black ink by electrohydrodynamic jet printing." Journal of nanoscience and nanotechnology 12.1 (2012): 446-450.

[77]. Corbin, Elise A., et al. "Micromechanical properties of hydrogels measured with MEMS resonant sensors." Biomedical microdevices 15.2 (2013): 311-319.

[78]. George, Sherine, et al. "Sensitive detection of protein and miRNA cancer biomarkers using silicon-based photonic crystals and a resonance coupling laser scanning platform." Lab on a Chip 13.20 (2013): 4053-4064.

[79]. Arrabito, Giuseppe, and Bruno Pignataro. "Solution processed micro-and nano-bioarrays for multiplexed biosensing." Analytical chemistry 84.13 (2012): 5450-5462.

[80]. Poellmann, Michael J., and Amy J. Wagoner Johnson. "Multimaterial polyacrylamide: fabrication with electrohydrodynamic jet printing, applications, and modeling." Biofabrication 6.3 (2014): 035018.

[81]. Sutanto, Erick, et al. "Electrohydrodynamic jet printing of micro-optical devices." Manufacturing Letters 2.1 (2014): 4-7.

[82]. Kim, Bong Hoon, et al. "High-resolution patterns of quantum dots formed by electrohydrodynamic jet printing for light-emitting diodes." Nano letters 15.2 (2015): 969-973.

[83]. Kim, Bong Hoon, et al. "High-resolution patterns of quantum dots formed by electrohydrodynamic jet printing for light-emitting diodes." Nano letters 15.2 (2015): 969-973.

[84]. Park, Jang-Ung, et al. "Nanoscale, electrified liquid jets for high-resolution printing of charge." Nano letters 10.2 (2010): 584-591.

[85]. Ahn, Bok Y., et al. "Omnidirectional printing of flexible, stretchable, and spanning silver microelectrodes." Science 323.5921 (2009): 1590-1593.

[86]. Juraschek, R., and F. W. Röllgen. "Pulsation phenomena during electrospray ionization." International Journal of Mass Spectrometry 177.1 (1998): 1-15.

[87]. Poon, H. F., D. A. Saville, and I. A. Aksay. "Linear colloidal crystal arrays by electrohydrodynamic printing." Applied Physics Letters 93.13 (2008): 133114.

[88]. Cristancho, Diana M., et al. "Volumetric properties of glycerol+ water mixtures at several temperatures and correlation with the Jouyban-Acree model."Revista Colombiana de Ciencias Qu ímico-Farmacéuticas 40.1 (2011): 92-115.

[89]. Cheng, Nian-Sheng. "Formula for the viscosity of a glycerol-water mixture."Industrial & engineering chemistry research 47.9 (2008): 3285-3288.

[90]. Einstein, Albert. "Eine neue bestimmung der moleküldimensionen." Annalen der Physik 324.2 (1906): 289-306.

[91]. Guth, Eugene, and R. Simha. "Untersuchungen über die viskosität von suspensionen und lösungen. 3. über die viskosität von kugelsuspensionen."Colloid & Polymer Science 74.3 (1936): 266-275.

[92]. Thomas, David G. "Transport characteristics of suspension: VIII. A note on the viscosity of Newtonian suspensions of uniform spherical particles."Journal of Colloid Science 20.3 (1965): 267-277.

[93]. Korkut, Sibel, Dudley A. Saville, and Ilhan A. Aksay. "Collodial cluster arrays by electrohydrodynamic printing." Langmuir 24.21 (2008): 12196-12201.

[94]. John W. M. Bush (May 2004). "MIT Lecture Notes on Surface Tension, lecture 5" (PDF). Massachusetts Institute of Technology. Retrieved April 1, 2007.

[95]. Langbein, Dieter. "The shape and stability of liquid menisci at solid edges."Journal of Fluid Mechanics 213 (1990): 251-265.

[96]. Chandrasekhar, S. Hydrodynamic and Hydromagnetic Stability; Clarendon Press: Oxford, 1961; Chapter 12, pp 540-543.

[97]. Deegan, Robert D., et al. "Capillary flow as the cause of ring stains from dried liquid drops." Nature 389.6653 (1997): 827-829.

[98]. Behrens, Sven H., and David G. Grier. "The charge of glass and silica surfaces." The Journal of Chemical Physics 115.14 (2001): 6716-6721.

[99]. Kim, Jin-Keun, and Desmond F. Lawler. "Characteristics of zeta potential distribution in silica particles." Bulletin of the Korean Chemical Society 26.7 (2005): 1083-1089.

[100]. Júnior, José Antonio Alves, and João Baptista Baldo. "The behavior of zeta potential of silica suspensions." New Journal of Glass and Ceramics 4.02 (2014): 29.

[101]. Bergström, Lennart. "Hamaker constants of inorganic materials." Advances in Colloid and Interface Science 70 (1997): 125-169.

[102]. Love, John D. "On the van der Waals force between two spheres or a sphere and a wall." Journal of the Chemical Society, Faraday Transactions 2: Molecular and Chemical Physics 73.5 (1977): 669-688.

[103]. Israelachvili, Jacob N. Intermolecular and surface forces: revised third edition. Academic press, 2011.

[104]. Bhattacharjee, Subir, Menachem Elimelech, and Michal Borkovec. "DLVO interaction between colloidal particles: beyond Derjaguin's approximation."Croatica Chemica Acta 71.4 (1998): 883-903.

[105]. Behrens, Sven Holger, et al. "Charging and aggregation properties of carboxyl latex particles: Experiments versus DLVO theory." Langmuir 16.6 (2000): 2566-2575.

[106]. Rabinovich, Yakov I., Madhavan S. Esayanur, and Brij M. Moudgil. "Capillary forces between two spheres with a fixed volume liquid bridge: theory and experiment." Langmuir 21.24 (2005): 10992-10997.

[107]. Li, Ruidi, et al. "Balling behavior of stainless steel and nickel powder during selective laser melting process." The International Journal of Advanced Manufacturing Technology 59.9-12 (2012): 1025-1035.

[108]. McCallum, Matthew S., et al. "Capillary instabilities in solid thin films: Lines." Journal of applied physics 79.10 (1996): 7604-7611.

[109]. Rauber, M., et al. "Thermal stability of electrodeposited platinum nanowires and morphological transformations at elevated temperatures." Nanotechnology 23.47 (2012): 475710.